OPTICALLY ACTIVE NANOMATERIALS IN FOOD AND AGRICULTURE APPLICATIONS

KAMALJIT KAUR

A thesis submitted for the partial fulfillment of

the degree of Doctor of Philosophy

Institute of Nano Science and Technology(INST), Mohali

Knowledge city, Sector 81, SAS Nagar, Manauli Pin-140306

Indian Institute of Science Education and Research (IISER), Mohali,

Knowledge city, Sector 81, SAS Nagar, Manauli Pin-140306

December, 2022

Dedicated to

my husband & beloved parents

Declaration

The work presented in this thesis has been carried out by me under the guidance of Dr. P.S. Vijaya Kumar at the Institute of Nano Science and Technology, Mohali. This work has not been submitted in part or in full for a degree, a diploma, or a fellowship to any other university or institute. Whenever contributions of others are involved, every effort is made to indicate this clearly, with due acknowledgement of collaborative research and discussions. This thesis is a bona fide record of original work done by me and all sources listed within have been detailed in the bibliography.

KAMALJIT KAUR

In my capacity as the supervisor of the candidate's thesis work, I certify that the above statements by the candidate are true to the best of my knowledge.

DR. P.S. VIJAYA KUMAR

Acknowledgements

While a completed dissertation bears the name of a student, the process that leads to its completion is always accomplished in combination with the love and help of other people. I am indebted to many people for their forever support, love and encouragement. It is a great pleasure to have the opportunity to thank them. I am afraid that these words would not be enough to express the deep gratitude and respect I feel for them.

First, to my lord, without whom nothing would have been possible but with whom everything is.

I am all overwhelmed and humbled to thank major people involved for completion of my entire PhD tenure. First and foremost, Professor, **Dr. P.S. Vijaya Kumar** who has given me a golden opportunity to work on optically active nanomaterials for its biological applications. He has been extremely helpful to me during the entire period of my research work. Without his help and encouragement this dissertation would not have been possible. He was always there to support and lift me up even during my bad times. I am extremely thankful to him for believing in me and always supporting me in all the possible ways and design new experiments to improve my research. Besides my supervisor I would like to thank the research monitoring committee **Dr. Prakash Neelakandan** and **Dr. Monika Singh.**

I am deeply grateful to CSIR for providing me the financial aid and INST for providing excellent research facilities.

My sincere thanks extend to our collaborators **Dr. Ujjal Gautam, Prof. Chen sheng Yeh, Dr Boddu.S. Naidu, Prof Eswaramoorthy Muthusamy, Prof Kesavan Subaharan, Dr. Nitin, Prof. Jeffrey P. Youngblood** and **Dr Selvaraju Kanagaranjan** who have helped me in many ways to complete my research work.

I would like to also thank my fellow lab mates**: Dr. Ashmeet Singh, Dr Sandeep Sharma, Dr Pulkit Bindra, Dr. Muthu Kumaran, Amandeep Kaur Bandana Kumari Sahu, Mahima Chandel, Kanchan Swami, Parul Sharma, Prem, Sarita, Neeraj, Ankita, Gagandeep Kaur, Navpreet Kaur, Anshika Gupta**. Their support and encouragement helped me a lot during my PhD journey.

I thank a ton to my Mom (**Mrs. Jasbir Kaur**), Dad (**S. Kuljit Singh**), Mother in law (**Mrs. Iqbal Kaur**) and father in law **(S. Narinder Singh**) and all my family members (**Mr. Daljit Singh, Mr. Sarabjit Singh, Mrs. Nirvair Kaur, Mrs. Damantej Kaur, Mrs. Manpreet**

Kaur, S. Amandeep Singh) as they have encouraged my academic interests from day one and were even there to lift me up when I almost broke down. Your consistent prayers, love and encouragement helped me sail during my career.

Finally heartfelt thanks to my husband **Mr. Amardeep Singh** for his immense support and constant love that lifted me up during the bad times. Honestly, this dissertation would not have been complete if he had not been my side. He has always helped me relax by stimulating discussions. He provided me with the tools that I needed to choose in the right direction and helped me in many ways to successfully complete my dissertation. I thank him a lot for all the love, care and affection he showered on me during these years.

Last but not the least my pet dog Sandy whose love and gratitude meant a lot to me and was a stressbuster.

I also thank all the technical and non-technical staff of Institute of Nanoscience and Technology, Mohali.

I sincerely express my love and gratitude to my Mom, Dad, and husband. I can honestly say that without your intervention this dissertation would not exist. You have helped prevent slip through cracks, so thank you for being there always.

KAMALJIT KAUR

Abstract

In traditional agriculture sun light play an important role in the key activities like production, protection, processing and sensing. First, the photosynthesis is the key process for the production, which solely depend on light; while, in protection light trap play an important role in the pest control; finally, for the processing of the yield, globally the harvesting time is scheduled in the maximum light hours season for the easy drying and storage. Hence with this inspiration here an attempt has been made to use photo active nanomaterials to do some additional job in controlled fashion for the advanced agriculture application. In this context we have explored the application of optically active nanomaterial for the protection, processing and sensing.

Mushrooms are rich in ergosterol, a precursor of ergocalciferol, which is a type of vitamin D_2. The conversion of ergosterol to ergocalciferol takes place in the presence of UV radiation by the cleavage of the "B-ring" in the ergosterol. As the UV radiation cannot penetrate deep into the tissue, only minimal increase occurs in sunlight. In this study, upconversion nanoparticles with the property to convert deep-penetrating near-infrared radiation to UV radiation have been cast into a disk to use sunlight and emit UV radiation for vitamin D conversion. An engineered upconversion nanoparticle (UCNPs) disk with maximum particles and limited clusters demonstrates ~2.5 times enhanced vitamin D_2 conversion.

The indiscriminate use of pesticides leads to irreparable damage to the ecosystem, which motivates for sustainable alternatives like pheromone-assisted pest management. The tomato pinworm *Tuta absoluta* is a major threat to tomato cultivation. Moreover, its green management technology uses a pheromone trap that has a short field life. To overcome this problem, a pheromone composite with graphene oxide (GO) and amine-modified graphene oxide (AGO) that can extend the diffusion path has been developed. The composite stimulates an effective electrophysiological response in the antenna, which results in trapping of a significantly higher number of insects as compared to the commercial septa, thus qualifying it for field evaluation. Compared to AGO, the GO composite has pheromones assembled into a multilayer, which increases the pheromone diffusion path. This in turn resulted in the extension of the pheromone life that proportionally increased the pest trapped. Further the nano-edifice has been tested for photo triggered controlled pheromone release and pest collection. This technique will be beneficial to farmers as they have longer field efficacy to keep the pest damage low in an environmentally friendly manner.

Lycopene, a natural colorants and antioxidant with a huge growing market is highly susceptible to photo/thermal degradation, which demands real-time sensors. Hence, here a transparent upconversion nanoparticles (UCNPs) strip, having Yb^{3+} 30 mol % Tm^{3+} 0.1 mol % β-$NaYF_4$ UCNPs which shows intense 475 nm emission, has been developed. This strip has been found sensitive to lycopene, down to 10 nM using a smart phone camera; which is due to static quenching confirmed by life time study. In comparison to previous paper strips, here the transparent strip has minimal scattering with maximum sensitivity in spite of not using any metal quenchers. An increase in strip hydrophobicity during the fabrication process complements the strip to selectively permeate and present an extraction-free substitute analysis to chromatography. Hydrophobicity also adds the capability to reuse the strip with ~100 % luminescence recovery.

Table of Contents

List of Figures

List of Tables

Abbreviations

ACN	Acetonitrile
AFM	Atomic force microscopy
AGO	Amine modified graphene oxide
BHT	Butylated hydroxy Toluene
CNC	Cellulose nanocrystals
CCD	Charged coupled detector
ch	Chitosan
DM	Dry mass
DMF	Dimethyl formamide
DMSO	Dimethyl Sulphoxide
EDX	Energy dispersive X ray spectroscopy
ET	Energy transfer
FTIR	Fourier transform infrared spectroscopy
GC-MS	Gas chromatography mass spectrometry
GO	Graphene Oxide
HPLC	High Performance liquid chromatography
HR-TEM	High Resolution transmission electron microscope
ICP-MS	Inductively coupled plasma -Mass spectrometry
IU	International Units
LOD	Limit of detection
LSPR	Localised surface plasmon resonance
MTBE	Methyl Tert-butyl ether
mV	milli volts

µg	microgram
NPs	Nanoparticles
NIR	Near infrared
ng	nanogram
pe	pectin
pM	pico-Molar
PL	photoluminescence
PEG	Polyethylene Glycol
PTT	Photothermal Therapy
ppb	parts per billion
ppm	parts per million
PVA	poly vinyl alcohol
PDA	Photodiode Array Detection
rcf	Relative centrifugal force
rpm	Revolutions per minute
SEM	Scanning electron microscopy
THF	Tetrahydrofuran
TEM	Transmission electron microscopy
TGA	Thermogravimetric analysis
UCNPs	Upconversion Nanoparticles
VIS	Visible
XRD	X Ray Diffraction
n	Principle quantum number
m	Magnetic quantum number
EAG	Electroantennogram

Chapter 1

Bibliographic Introduction

1. Introduction

1.1 Food and nutrition

With the ever-increasing population, food security is going to be a great challenge in front of the human progress. In food security, it is the responsibility of the research fraternity working in the food and agriculture to develop advance technology to ensure enough food as well as balanced nutrition.[1] While coming to the balanced nutrition, along with the carbohydrate and proteins, vitamins and minerals often needed to be fortified.

1.2 Importance of Vitamin D

In recent years especially after COVID-19 there has been an increased awareness of health benefits of vitamin D and the natural sources associated with it has been discussed. Vitamin D, which is also known as the sunshine vitamin is responsible for maintenance of healthy body functions like blood pressure,[2] overcome health issues like obesity,[3,4] type 1 and type 2 diabetes,[5] improved bone health,[6] reduced risk of cancer [7,8] and autoimmune disease.[9,10] Vitamin D deficiency is prevalent all over the world and affects all age groups in both men and women.[11] Further the disease severity dependents on the age of the individual, season and geographical location.[12,13] Some countries have a poor access to sunlight, like the ones in temperate condition (>30°N and > 30°S), therefore more prone to vitamin D deficiency, so these countries recommend regular fortification to their population.[14] Due to the sedentary indoor lifestyle of younger generation and elderly people, the sunlight exposure is minimised, therefore the deficiency increases. Also, dark skin coloured population with high melanin content are more prone to vitamin D deficiency, as melanin inhibits UV radiation from entering the skin and restricts the conversion process.[15] Also the overuse of the skincare sunscreen products restricts the vitamin D conversion. Community based statistics in India revealed that the prevalence of vitamin D deficiency is around 50% to 94%.[16,17]

Major function of vitamin D is the maintenance of bone health by the ability to stimulate the osteoblast cells and by inhibiting bone resorption. An adequate dose of vitamin D will be able to prevent bone fractures due to its ability of mineralise bone and maintain effective bone health.[18] The fundamental mechanism behind the anti-cancer properties of vitamin D is the ability to activate several kinases that arrests the cell cycle in G1/S phase and inhibit DNA synthesis in tumour/malignant cells.[19] Vitamin D is responsible for better cardiovascular function by maintenance of cardiovascular endothelial growth factor, which activates cell

transduction pathways for growth and proliferation.[20] In addition, vitamin D levels are also accountable for maintaining serum cholesterol levels and for the suppression of rheumatic heart disease, of which the latter is the cause for cardiac related deaths by reducing the expression of genes responsible for renin production that regulates blood pressure.[21] The deficiency of vitamin D includes rickets, insomnia, osteoporosis etc.[22]

Irradiation techniques like gamma radiation and electron beams are employed for antimicrobial action, prevention of browning, increasing the shelf life of the mushrooms thereby preserving its quality (proteins, sugars and vitamins) and key phenolics.[23] These irradiation techniques are cost effective and safe in improving the quality and aroma of vegetables and fruits.[24]

1.3 Vitamin D synthesis and its sources: The major source of vitamin D is the sunlight. There have been recent reports that prove that the agricultural farm workers are at a reduced level of vitamin D deficiency due to continuous sunlight exposure, which reduces the cancerous population. However, vitamin D_3 is the native form in human without any external supplementation but synthesized by animals by daily exposure of skin to the sunlight. Vitamin D_3 is produced in the skin by the sunlight, especially by the UV-B range in the solar spectrum, while irradiating 7-dehydrocholesterol present in the epidermal skin.[25,26] This photoreaction of 7-dehydrocholesterol with the UV light results in pre-vitamin D_3, which is further isomerised to vitamin D_3. Prolonged irradiation can result in the formation of tachysterol and lumisterol, which then isomerises to vitamin D in the dark. The mechanism of isomerisation of 7-dehydrocholesterol to vitamin D_3 is shown in Fig 1.1.

The metabolism of vitamin D in human body undergoes two step hydroxylation process that produces 25-hydroxy vitamin D (calcidiol) in liver and 1,25-dihydroxy vitamin D (calcitriol) in the kidney that is biologically most accepted form of vitamin D. The external sources of vitamin D could be classified as non-vegetarian and vegetarian based diet system. In this, the non-vegetarian sources are more abundant with respect to the vegetarian sources. The non-vegetarian sources include fish, salmon, tuna, meat, egg, chicken, turkey, liver, cured bacon, ham and red meat.[27] The diary source include milk, yoghurt and mushrooms.[28] The vegetarian dietary forms of vitamin D include vitamin D_2 and vitamin D_4 in phytoplankton and fungi. Nowadays, fortified fruits juices, milk and yogurt are available to help alleviate the deficiency. However, the amount of vitamin D varies from source to source. For example, the value ranges in 250 µg $100g^{-1}$ in cod liver oil, 8-30 µg $100g^{-1}$ in fatty fish such as salmonella, eel and 3-9 µg $100g^{-1}$ in lean fish such as sole and tuna.[29]

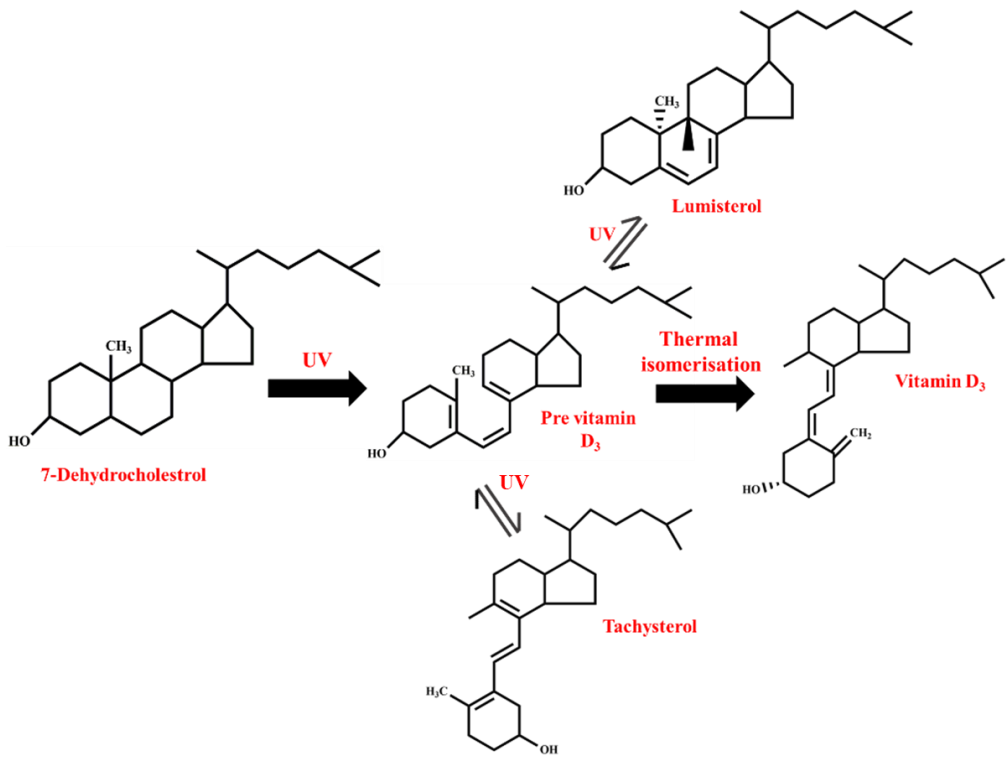

Fig 1.1 Mechanism of conversion of 7-dehydrocholesterol upon UV light irradiation in the sunlight. 7-dehydrocholestrol under the presence of UV light converts to pre vitamin D_3 (by cleavage of B ring) which further undergoes thermal isomerisation to form vitamin D_3. Continued irradiation of pre vitamin D_3 leads to reversible formation of tachysterol and lumisterol.

1.4 Vitamin D_2: Vegetarian source of vitamin D is basically obtained from a fungal sterol that support their cell wall, which is in substitution to lignin in the plant cell wall. Especially, vitamin D_2 is derived from the sterol called ergosterol, ergosterol is the major sterol comprising 80-90 % of the sterol content in fungal (mushroom) cell wall.[22,30] The ergosterol functions like cholesterol in the human body that assists in maintaining cell's structural strength and rigidity.[31] The ergosterol gets converted to vitamin D in the presence of UV radiation, (200-400 nm) by the cleavage of the B ring at C9 and C10 position.[25] Also, it has been found that vitamin D_2 is as beneficial as vitamin D_3 to maintain serum 1,25-dihydroxy vitamin D levels.[32]

1.4.1 Mushroom and vitamin D: The production of cultivated edible mushrooms is found to be maximum in China as it accounts for 87% of world output. Among 2000 edible varieties of mushrooms only 25 are accepted for human consumption. The major varieties of these includes *Lentinula* (22%), *Pleurotus* (19%), *Auricularia* (17%), *Agaricus* (15%), and *Flammulina* (11%) as shown in Fig 1.2.

Mushrooms have numerous medicinal and nutritional properties, which makes them to

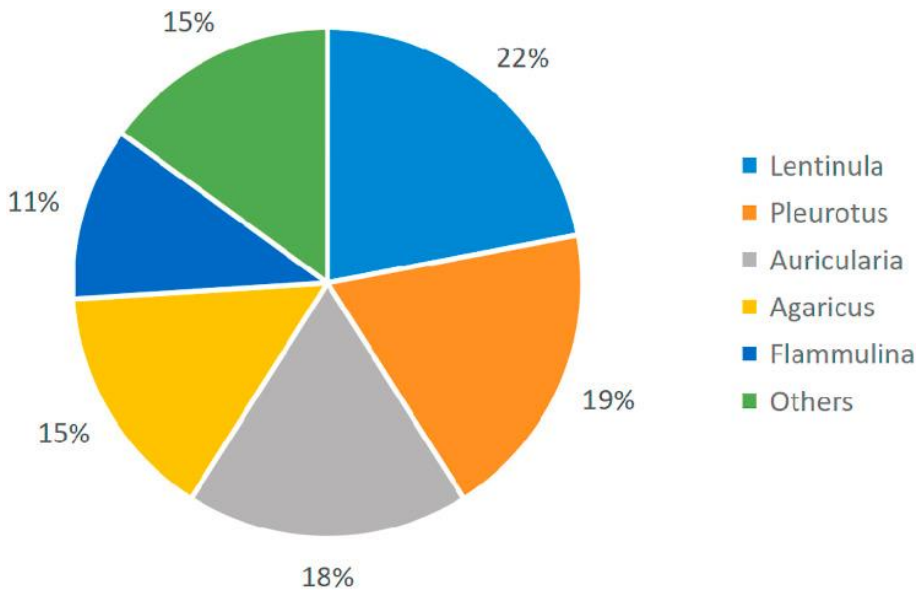

Fig 1.2 Pie chart showing the distribution of different mushroom varieties found in China.

be a source of excellent anticancer, antitumor. antibacterial, anti-tyrosinase, anti-inflammatory and hypo-glycemic properties.[33–35] The mushroom varieties like *Agaricus bisporus* are rich in various antioxidants, polyphenols, selenium and polysaccharides. The fruiting body in mushrooms is rich in ergosterol the precursor of vitamin D_2, and the content of ergosterol varies in different mushroom varieties.

1.5 Quantification and biological relevance: Vitamin D level in the body is given by quantifying 25-hydroxy vitamin D in blood serum, and the individual processing a concentration of less than 20 ng mL^{-1} is found to be deficient in vitamin D_2 levels.[36] Unlike vitamin D_3, which is not approved in all the countries globally for the fortification, in account of their sterol nature; the vitamin D_2 is certified by the FDA as fortification agent in many foods and dietary supplements. The recommended dose for vitamin D supplements varies with the age, gender, country's regulation, latitude, season and temperate conditions; for example, in kids it is 400 IU and for adults it is 800 IU.[37] The recommended dose of vitamin D in Australia and New Zealand is in the range of 200-600 IU [38]; America [38] and Canada [39] it is 600-800 IU and in UK it is 400 IU. Nowadays, various vitamin D fortified foods are available, which are mostly limited to dairy products like milk, juices, processed cheese etc.[40] Mushrooms are an excellent alternative fortified food to the population, who have lactose intolerance and low dairy product consumption.[41] The steps favouring vitamin D (most active 1,25-dihydroxy cholecalciferol) formation in skin are shown below in Fig 1.3.

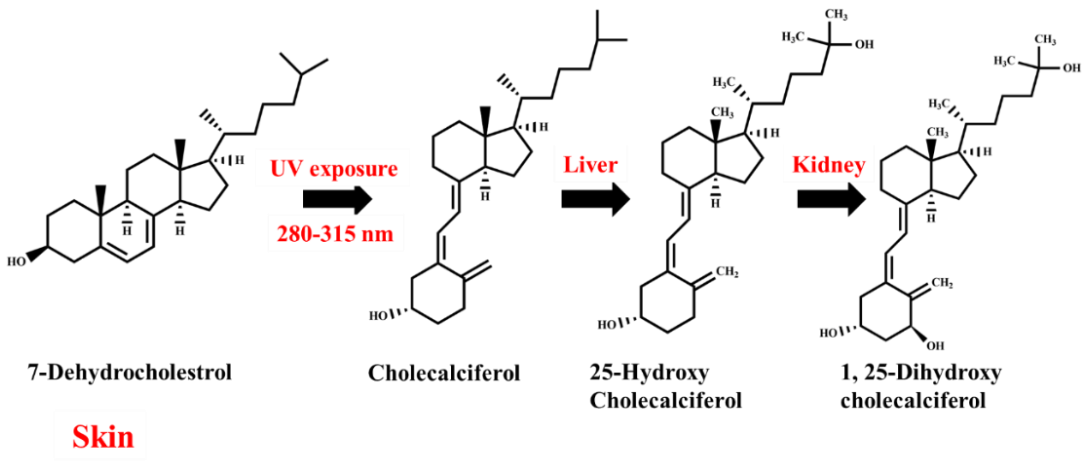

Fig 1.3 Steps of vitamin D formation in the body. Cholesterol which is already present in skin converts to 7-dehydrocholestrol by an enzyme DHCR7.7-dehydrocholestrol then undergoes B ring cleavage by UV exposure (280-315 nm) to form cholecalciferol (Pre vitamin D_3). Cholecalciferol is converted to 25-hydroxycholecalciferol in the liver and further hydroxylation step results in 1, 25-dihydroxy cholecalciferol in the kidney (which is identified as the most active form of vitamin D).

1.6 Details of the Vitamin D_2 fortification in Mushrooms through UV irradiation

UV assisted conversion and vitamin D_2 fortification in the mushroom is already in commercial practice in US, but the limitation of this method is the poor penetration depth of UV light. The UV light consists of three parts *viz*., UV-A, UV-B and UV-C (6-10 layers), among this the conversion was found to be the highest in the presence of UV-B as compared to UV-A and UV-C. Further several other factors affect the conversion of ergosterol to vitamin D, which includes intensity of UV light, time duration, moisture content in mushrooms as well as its particular orientation.[16,42] The conversion of ergosterol to vitamin D_2 in mushrooms is shown in Fig 1.4.

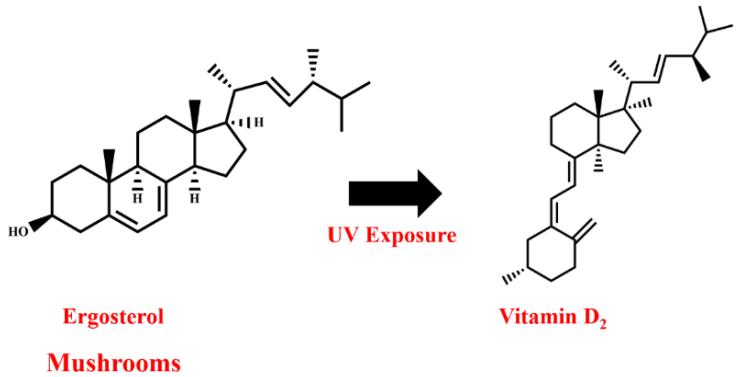

Fig 1.4 Figure illustrates the conversion of ergosterol to vitamin D_2 in mushrooms. The conversion is assisted in the presence of UV light by the cleavage of B ring in ergosterol.

Mushroom tissue depth plays an important role in ergosterol conversion to vitamin D_2. The sequence in mushroom tissue follows as;Button mushrooms > Shiitake > Oyster > Abalone > Enoki. [43] This was confirmed by Urbain *et al.* as the conversion of vitamin D_2 on the exposure of sunlight in the thick sliced mushrooms (12 mm) was significantly lower than thin mushrooms slice (9 mm thickness). Also, a similar study was performed by UV exposure to sliced mushrooms that were flipped from time to time and in case of others only one side was exposed. In this case it was observed that the sliced mushrooms flipped on both sides had a higher content of vitamin D_2 than the mushroom exposure to vitamin D_2 with just one side exposure due to increased exposure of gills.[44] Similar results were confirmed by Wu *et al*. that the content of vitamin D_2 in mushroom powder was more due to enhanced exposed surface area of the mushrooms.[45]

Agaricus is a genus of saprobic basidiomycetes that covers a broad range of 400 species distributed across the world. *Agaricus bisporus* is the most cultivated form and it accounts for one million metric tonnes annually.[46] Koyyalamudi *et al.* optimised different factors like UV radiations intensity, exposure time and distance of the radiation source for the ergosterol to vitamin D conversion in the button mushrooms (*A. Bisporus*). A time dependent increase in the vitamin D_2 levels has been observed while illuminating UV light having an intensity of 0.2-0.4 W cm-^{2}, in which the highest intensity of 0.4 W cm^{-2} showed maximum conversion. To know if the irradiation direction will play a role, Jasinghe *et al*. conducted the illumination with the gill and pileus facing the UV light, here the results show that the gills facing the radiation source for 2 hours to have the maximum conversion.[43] Simon *et al.* improved the vitamin D content in button mushrooms to 410.9 µg 100g^{-1} from 56.7 µg 100g^{-1}, which leads to 747 % increase in the presence of UV-B light at an exposure intensity of 1.06 J/cm^{2}.[47] The exposure to UV-B light is comparable to the exposure in the sunlight, which gave a conversion of 374 µg 100 g^{-1}; however, in the samples exposed to sunlight the riboflavin content was reduced, which is found to be the demerit of sunlight exposure method. Matilla *et al.* showed that vitamin D was less in the cultivable mushroom (0.21 mg 100 g^{-1} fresh weight) than wild mushrooms (2.91-29.82 mg 100 g^{-1} fresh weight) due to its culturing in dark sades.[48] The vitamin D_2 content is almost totally absent in the cultivated mushrooms *A. bisporus* white, *A. bisporus* brown, *P .ostreatus* (<0.1 µg/100g) and *Lentinus edodes* as the mushroom cultivation occurs in dark conditions, which greatly reduces the sterols conversion.

Different treatments employing UV irradiation in fresh mushrooms samples and also to freeze dried ones were carried out.[49] Here the freeze-dried ones are able to show better conversion

due to enhanced exposed surface area. Also, the mushroom fortified with vitamin D_2 through illumination, has been found stable without any degradation for a period of up to ~8 days in a cold storage (4 °C).

Matilla *et al*. was the first one to study that the distribution of vitamin D varies in different parts of mushrooms.[22] Maximum amount of vitamin D was found in the pileus in *C. tubaeformis, B. edulis* and *L. actarius* species. In contrast, in case of *C. Cibarius* the gills contained more amount of vitamin D. Agreeing to this Huang *et al.* revealed that vitamin D content is lowest in stipes as it is expected to show a greater content of polysaccharides for imparting structural strength and rigidity (also in *C cibarius*).[30] Jasinghe *et al.* reported that in shiitake mushroom the highest amount of ergosterol in gills and lowest in the stalk; further the order of decrease is as follows Gills>outer caps> stalks.[43] Among the mushrooms highest content of ergosterol was found in Button mushrooms > Shiitake > Oyster > Abalone > Enoki.[43] Pulsed UV irradiations has led to an increase of Vitamin D in *A. bisporus* to 27 µg g^{-1} DW with 12 pulses, whereas unprocessed mushrooms contained negligible amounts of vitamin D_2.[50]

The bioavailability of the vitamin D from the UV irradiated button mushrooms has been tested using the rats feeded through oral route, which showed increase in the serum vitamin D amount in proportional to the feed given.[51] Many countries in Asia [42,49],North America [52], Africa [53], Europe[28,50,54] and Australia[55] are following the vitamin D enhancement in mushrooms using UV light.

Viraj J Singhe *et al.* studied that prolonged irradiation time of more than one hour does not improve vitamin D_2 conversion by 2 x 2 factorial design. With increased temperature due to prolonged UV irradiation time leads to thermal rearrangement of ergosterol favouring the production of other isomerisation products as tachysterol and lumisterol.[16] The kinetics of ergosterol to vitamin D_2 follows a zero-order reaction reaction.

$$K=K_o \exp(-E_a/RT)$$

Where E_a=Activation energy of conversion of ergosterol to vitamin D_2, R= Gas constant, and T=Temperature.

The group also observed that the conversion in different type of mushrooms is highest during UV-B exposure in comparison to UV-A and UV-C, since mushrooms receive more than 50 % irradiation source in UV-B than in UV-C.[42] The conversion to vitamin D_2 is also dependent on the moisture content as high moisture content can dilute the ergosterol and reduce the

conversion. The moisture content governs the vitamin D_2 conversion in shiitake mushrooms and it was found that highest vitamin D_2 conversion was obtained at 80 % moisture content at 35 °C temperature, followed by 60 % moisture content at 35 °C and 80 % moisture content at 25 °C. The lowest conversion was achieved for 60 % moisture content at 25 °C.[16]

1.7 Upconversion Mechanism: Upconversion nanoparticles (UCNPs) are composed of an inorganic host lattice with lanthanide ions as dopants. The electronic configuration of lanthanide ions is $[Xe]4f^n5d^m6s^2$ (where n is principal quantum number and m is magnetic quantum number) and the lanthanide family comprises of the elements from lanthanum to lutetium including scandium and yttrium. UCNPs follow a non-linear optical process that requires simultaneous absorption of two or more photons in contrast to two photon process dyes or quantum dots.[56] These nanoparticles undergo anti-stokes emission and long lived intermediate states.[57] Extensive research is pursued for tuning the emission in the UV-Vis and NIR regions by varying the lanthanide ion concentration and the host lattice.[58–60] The excitation of these nanoparticles require an inexpensive continuous laser having power in the range of 10-10^3 W cm^{-2}, whereas the dyes or quantum dots require high pulsed laser power in the range of 10^6-10^9 W cm^{-2}.[61] In contrast to quantum dots or organic dyes where the luminescence is strongly governed by the size and resulting environmental conditions [58], the emissions from UCNPs are weakly governed by size and environment due to well shielding by 5s and 5p orbitals.[57] Further the lanthanides in the UCNPs do not follow quantum confinement unlike quantum dots.[62] Therefore the size dependent emission cannot be predicted for these nanoparticles. Another major advantage of the use of upconversion nanoparticles is resistance to photobleaching, minimal visible background autofluorescence, anti-counterfeiting, high contrast 3D imaging, photodynamic therapy, resistant to photodamage and deep tissue penetration (due to NIR excitation which comes in between biological transparent window with minimal scattering), which is of utmost importance in biological applications.[63–67] The applications of UCNPs includes photo voltaic solar energy conversion, flat panel displays [68], light emitting diodes [69], temperature sensors.[70] Further, the stability of UCNPs make them a better alternative of the organic dyes in the confocal two photon imaging applications.[71] Signature traits or characteristic feature of these nanoparticles is the sharp emission bandwidths, long lifetimes (milli second lifetime) and narrow emission bandwidths for multiplexed imaging, which arise due to electronic f-f transitions in the lanthanide ions as dopants. UCNPs are more prone to surface defects than its bulk counterparts due to its high surface area to volume ratio. The prepared UCNPs are hydrophobic due to the presence of oleic

acid chains on the surface. Broad applications of upconversion nanoparticles are shown in Fig 1.5

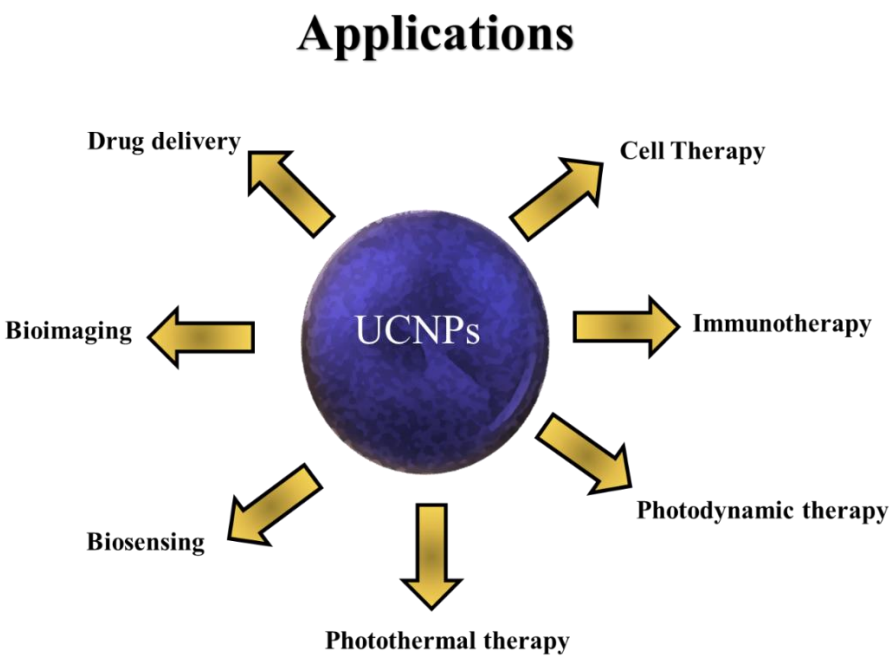

Fig 1.5 Different applications of upconversion nanoparticles.

1.8 Tailoring UC luminescence:

1.8.1 Local crystal field: According to the Laporte's rule, the intra 4f transitions are forbidden but in UCNPs, the transitions are partially allowed due to variation induced in the local crystal field by the presence of higher electronic configuration elements.[56] Chen *et al.* observed an increase in the green emission of Y_2O_3, Er^{3+} nanocrystals using 980 nm laser excitation by co-doping with Li^{3+} ions. An increase in the Li mol % to 5 mol% led to the increase in the emission by 45-75 times because Li^{3+} ions comprise smallest ionic radii that can easily co-localise in the host lattice, thereby enhancing the fluorescence upconversion.[72] Similar experimental results were followed by Chen *et al.* by co-doping of Li^{3+} ions in the oxide host lattice by approx. two orders of magnitude.[73]

1.8.2 Host lattice: There are a wide variety of host lattice that can be used for suitable upconversion emission like fluorides, oxides, and phosphates. The thumb rule for selection of a host lattice is that it should possess low phonon energies, which minimizes the non-radiative energy losses and therefore increases the upconversion emission. For example, the phonon energy of $NaYF_4$ [74](fluoride cut off phonon energy ~350 cm^{-1}), Y_20_3 [75] (cut off phonon energy ~550 cm^{-1}), and oxyfluorides and oxychlorides ex GdOCl [76] (cut off phonon energy ~ 500 cm^{-}

[1]). Therefore, in conclusion the fluorides have the lowest phonon energies that minimizes the non-radiative energy losses in the excited state or any of the intermediate states. Further among fluorides, β-phase are appreciated, since the non-radiative energy losses are minimized due to its low phonon energies and a high crystal stability.[77,78] In a demonstration, Yang *et al.* found that $Er^{3+,}$ Tm^{3+} doped $NaLuF_4$ exhibits 10 times stronger upconversion luminescence than the $NaYF_4$, Yb^{3+}, Tm^{3+} doped lattice.[79]

1.8.3 Sensitizer: After the appropriate choice of the host matrix, sensitizer plays an important role in photon absorption. Among the sensitizers ytterbium is the best choice, as it has a wide absorption cross section at NIR excitation due to its $^2F_{7/2}$ to $^2F_{5/2}$ transition that acts as an efficient ion for transfer of the pumped energy to the activator. Further, ytterbium gives efficient energy transfer for upconversion or donate the energy levels to emitter ions like Er or Tm ions. As expected if the concentration of ytterbium is increased it will absorb greater number of photons but in contrast the increased concentration results in energy losses due to several cross relaxation pathways.[61] Therefore, an ideal concentration to minimize the cross relaxation energy losses is kept closer to approx. 20 mol %. Following the sensitizer, activators like Er^{3+}, Tm^{3+}, Ho^{3+} extract energy from nearby sensitizers and promote to higher energy levels; thereby complete the energy transfer process in UCNPs.[57] Among the various activator's erbium is the best choice due to its highest upconversion efficiency and similarity in the energy levels between $^4I_{11/2}$ and $^4I_{15/2}$ and between $^4F_{7/2}$ and $^4I_{11/2}$. The concentration of the activator is kept low to less than 2 mol % to minimize the non-radiative energy losses.

1.8.4 Plasmonic enhancement: There has been enormous interest and research on the enhancement of fluorescence emission from quantum dots or dyes using metallic nanoparticles, the reason behind this has been found to be LSPR. This has been confirmed with distance dependent enhancement studies. Similar phenomenon has also been used for enhancing the upconversion emission, hence the LSPR increased the excitation rate due to local field enhancement, which result in increase in the emission. This is confirmed with study having UCNPs adjacent to Au, Ag or Al.[80–82] This LSPR dependent enhancement finds major applications in sensing[83,84] biomedical imaging,[85,86] solar cells,[87] therapeutics[88] and single molecule detection.[89] Zhang *et al*. prepared $NaYF_4$,Yb^{3+} Er^{3+} nanocrystals on sputtered gold island films and observed more than 5 fold increase in the upconversion emission. The enhancement was also confirmed using spectroscopic studies, where the enhancement was found to be 12 times at selected spectral positions.

Saboktakin *et al.* used dense Au/Ag films and Al_2O_3 spacer to enhance the emission of $NaYF_4$, Yb^{3+}, Tm^{3+} and $NaYF_4$, Yb^{3+}, Er^{3+}. The oxide layer is important as it induces polarisation of the metal NPs. The Al_2O_3 layers deposited using atomic layer deposition showed that a distance of 5 nm for Au NPs and 10 nm for Ag NPs is appropriate for enhancing the upconversion emission. Yb^{3+}, Er^{3+} doped $NaYF_4$ with Au NPs showed an enhancement factor of 5.2 and 3.5 times in the emission wavelength region of 540 nm and 650 nm respectively. In case of Ag nanoparticles the enhancement factor has been enormous *i.e.,* by 30 and 45 times in wavelength range of 540 nm and 650 nm respectively.[90]

1.9 Upconversion energy transfer Process: There are various processes involved in the energy transfer for upconversion nanoparticles.

1.9.1 Excited State Absorption: This excited state absorption (ESA) process occurs within the single ion due to the presence of ladder like energy levels in the lanthanide series. Primarily the ions in the ground state are excited by high energy pump photon to E1 and by further absorption of another pump photon it is excited to the next level E2. Also, the dopant ion concentration should be as low as 2% in order to avoid any non-radiative cross relaxation process.[61] The transitions to different energy levels is shown in Fig 1.6

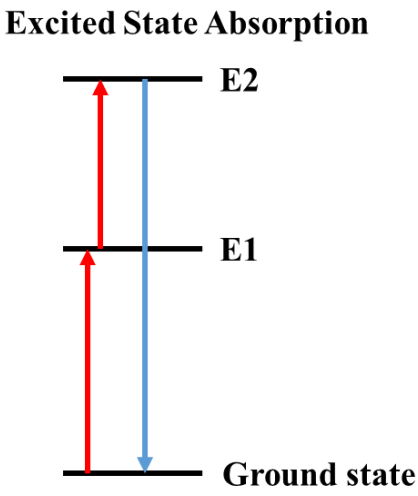

Fig 1.6: Schematic showing energy level diagram in excited state absorption. The process occurs within single ion due to ladder like energy level in lanthanides.

1.9.2 Energy Transfer Upconversion: Energy transfer upconversion (ETU) is associated with two ions. Energy transfer utilises a crystal host lattice with lanthanide ions embedded as sensitizers and activators. While excitation using 980 nm laser, the energy is non-radiatively transferred between two related ions by dipole-dipole interaction. Thus, the sensitizer transfers energy to the activators, which excites to higher energy levels and then emission occurs from the activator by the process of radiative decay. The efficiency of this process is more in comparison to excited state absorption. Dopant ion concentration should be kept low to avoid the cross -relaxation process. The most efficient ETU pairs are Yb^{3+}/Tm^{3+}, Yb^{3+}/Er^{3+}, Yb^{3+}/Ho^{3+} due to well resonating transitions in these pairs.[91] For example in case of Yb^{3+}/Er^{3+} co-doped pairs, Yb^{3+} absorbs 980 nm irradiation and gets excited from $^2F_{7/2}$ to $^2F_{5/2}$, Er^{3+} ion is initially in the ground state $^4I_{15/2}$ and reaches to $^4I_{11/2}$ by energy transfer upconversion. Due to close overlap between these two ions, energy is exchanged and Yb^{3+} ion is relaxed to its ground state and the Er^{3+} ion is excited to its higher energy level. The resulting emission will give green emission at 543 nm and red emission at 655 nm. The energy levels in energy transfer upconversion is shown in Fig 1.7

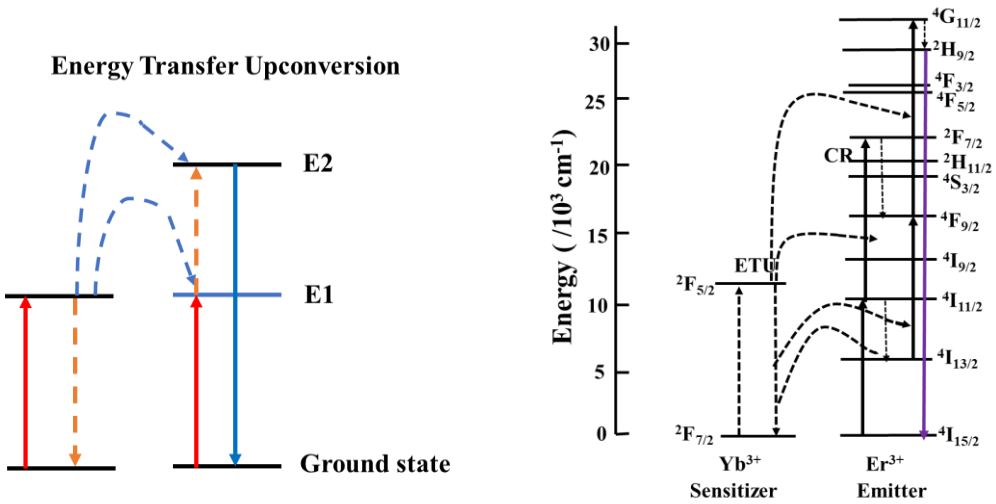

Fig 1.7 Schematic showing energy levels in energy transfer upconversion. The process occurs in the presence of two closely related ions (Dipole-Dipole interaction).

1.9.3 Cooperative Upconversion: Cooperative emission is a non-linear optical process whereby three ions are involved. In this process during laser excitation ion 1 and ion 3 are excited to a higher energy level and ion 2 is in the ground state. Due to close proximity of ion 1 and ion 3, energy transfers to ion 2 and forms a virtual excited state. Therefore, the upconversion emission occurs from ion 2. The upconversion emission efficiency is lower than

both the ESA and ETU. The Yb^{3+}/Eu^{3+}, Yb^{3+}/Pr^{3+} form cooperative upconversion pairs.[92] The schematic showing the energy transfer in cooperative upconversion is shown in Fig 1.8

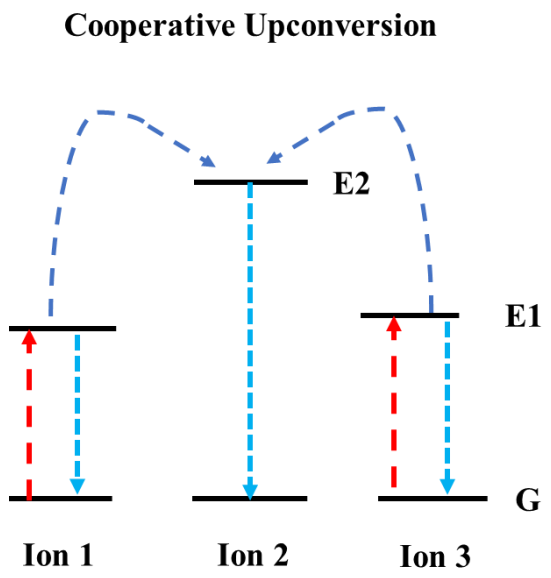

Fig 1.8 Schematic showing energy transfer in cooperative upconversion. This process involves the use of three ions i.e., lanthanide series.

Among all these processes the energy transfer upconversion is the most efficient method with minimum energy losses.

1.10 Upconversion nanoparticles colour tunability: In principle it is possible to tune the colour output of UCNPs by varying the emitter; further while keeping the emitter same and changing the sensitizer to emitter doping ratio or by giving a thin shell to cover the defects, the intensity of any particular emission or the whole emission band can be enhanced. Ytterbium is generally used as the sensitizer that can readily avail energy migration to activators like Tm^{3+}, Er^{3+} or Ho^{3+} using a single excitation wavelength at 980 nm.[56] Liu *et al.* synthesized the β-$NaYF_4$,Yb^{3+},Tm^{3+} doped upconversion nanocrystals using coprecipitation technique. The upconversion emission spectra of this was recorded under 980 nm laser excitation, which gave multiple emission peak maxima at 360 nm, 450 nm (four photon process), 475 nm, 650 nm (three photon) and 695 nm, 800 nm (two photon) due to transitions in $^1D_2$ to $^3H_6$,$^1D_2$ to $^3H_4$, $^1G_4$ to $^3H_6$, $^1G_4$ to $^3H_4$, $^3F_2$ to $^3H_6$ respectively. Therefore, the selection of different combination of lanthanide ions is a straightforward way of tuning the upconversion emission for its applications. The energy level diagram employing the use of Yb^{3+} as sensitizer and Tm^{3+} as emitter is shown in Fig 1.9.

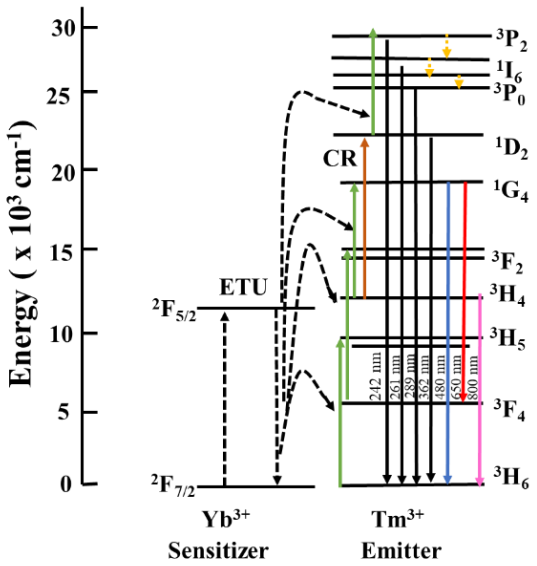

Fig 1.9 Energy transitions in $NaYF_4$, Yb^{3+}, Tm^{3+} upconversion nanoparticles. This involves Yb^{3+} as sensitizer and Tm^{3+} as emitter due to closely related energy levels.

Wang *et al.* optimised the concentration of Yb^{3+} and Tm^{3+} for tuning the emission in the visible and NIR region. As the Yb^{3+} concentration increases from 20 to 40 mol % the emission at 360,450 and 475 nm is found to gradually increase while the emission at 650 nm stayed constant. Then further fixing the doping concentration of Yb^{3+} at 20 mol % and then varying Tm^{3+} concentration from 0.2 mol% to 5 mol% there is gradual quenching in the emission at 360 nm and 450 nm, which proves that increased Tm^{3+} concentration quenches the blue emissions.[93] Therefore by varying the Tm^{3+} concentration, the fluorescence emission corresponding to the four photon process than the three photon process can be achieved. The universally accepted concentration of thulium is fixed at 0.5 mol %, because the chances of cross relaxation losses can be kept minimum. Similarly, Chen *et al.* observed that for 25 nm sized $NaYF_4$, 20% Yb^{3+}, 2% Tm^{3+} upconversion nanoparticles there is 11 times enhancement in the upconversion fluorescence intensity in comparison to 7 nm sized $NaYF_4$, 20% Yb^{3+}, 2% Tm^{3+}. Also by fixing the concentration of Tm^{3+} at 2 mol% and gradually increasing the concentration of ytterbium from 20 to 100 mol% there is an increased emission peak at 800 nm by 8.6 times as shown in Fig 1.10.[94]

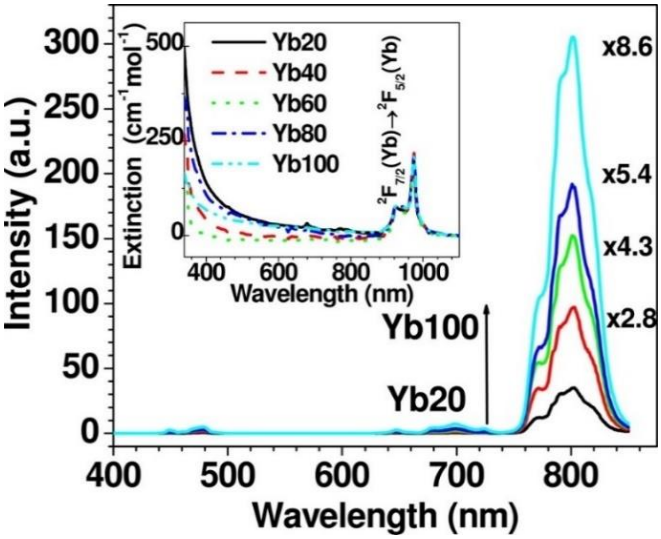

Fig 1.10 Fluorescence response of upconversion nanoparticles in response to increasing Yb^{3+} concentrations during synthesis. Reprinted from Ref 96. Copyright 2010, American Chemical Society.

A gradual decrease in the blue emission was observed for $NaYF_4$, Yb^{3+}, Tm^{3+} nanoparticles as the particle size reduces.[95] Chen *et al.* observed that the addition of cerium ions in the $NaYF_4$, 20% Yb^{3+}, 2% Ho^{3+} host lattice can change the fluorescence emission from green to red under 970 nm laser excitation, which is due to the cross-relaxation process between Ho^{3+} and Ce^{3+} ions.

1.11 Upconversion nanoparticles in sensing: Liu *et al.* synthesized $NaYF_4$, Yb^{3+} Er^{3+}, Tm^{3+} co-doped upconversion nanoparticles using co-precipitation technique. The prepared UCNPs were used to prepare curcumin-UCNPs hybrid system for selective sensing of fluoride ion. As the fluorescence emission of UCNPs overlaps with the absorbance of the Curcumin - fluoride ions complex, a detection limit of 0.10 ppm was achieved by the system due to inner filter effects phenomenon.[96]

Deng *et al.* prepared water dispersible $NaYF_4$, Yb^{3+}, Tm^{3+} co-doped upconversion nanoparticles, for assessing intracellular glutathione levels, an important anti-oxidant in mammalian and eukaryotic cells. The sensing hybrid was composed of UCNPs-MnO_2 nanosheets. Upconversion nanoparticles served as a substrate for the growth of MnO_2 nanosheets using $KMnO_4$ as the precursor in the MES buffer. An enhancement of 100-fold was achieved in the blue region (350 nm) with just 2 equivalents of glutathione. This is due to glutathione mediated reduction of MnO_2 nanosheets using a thiol disulphide exchange. This assay was found to have a detection limit of 0.9 µM.[97]

Wang *et al.* prepared $NaYF_4$, Yb^{3+}, Er^{3+} co-doped particles for sensing copper with a LOD of 1.5 nM. The sensor possesses an extraordinary signal to noise ratio of > 277. The prepared nanoparticles were conjugated with DNA-zyme and labelled with BHQ1(Black Hole quencher) as energy acceptor. As copper is added it will proportionally interact with the catalytic core and will cleave the DNA-zyme labelled strand thus restoring the quenched fluorescence emission. The sensor acts as a turn on sensor, as the copper ions restores the fluorescence intensity to 8.7 folds.[98]

Cristobal *et al.* prepared $NaYF_4$ Yb^{3+}, Er^{3+} co-doped UCNPs having an emission in the range of 550 nm and 650 nm, which has been further coated with silica to facilitate single stranded DNA attachment. Graphene oxide-UCNPs@SiO_2 formed an effective FRET pair since there is an effective overlap between upconversion nanoparticles emission and absorption of graphene oxide. So, there is a gradual decrease in the fluorescence intensity due to π- π stacking interactions between GO surface and UCNPs. The fluorescence intensity was recovered in the presence of complementary base pairing. GO concentration was optimised as 0.3 mg mL^{-1} for effective quenching and a detection limit of 5 pM.[99]

Zhang *et al.* prepared a sensor for monitoring mercury levels in green tea using $NaYF_4$, Yb^{3+}, Er^{3+} @$NaYF_4$ shell by luminescence resonance energy transfer (LRET) between the Au NPs and UCNPs. Owing to the spectral overlap between Au NPs and UCNPs fluorescence the above LRET pair has been prepared. Adding cysteine to this pair restored the luminescence, owing to cysteine triggered aggregation of Au NPs. On incubation of Au NPs with mercury and cysteine, mercury formed a more stable complex as $[Hg(Cys)_n]^{2-}$ and weakened the luminescence restoring ability of cysteine. Thus a proportional Hg^{2+} dependent change in luminescence has been observed, which was used for the sensing with a limit of detection as low as 12.5 nM.[100]

Pan *et al.* prepared $NaYF_4$, Yb^{3+}, Er^{3+} doped UCNPs and conjugated with *E.coli* monoclonal antibody to produce fluorescent probes with the limit of detection as 10 cfu mL^{-1} and detection time of less than 3 hours. The fluorescent probe was incubated with different *E. coli* concentrations and then quenching of 657 nm emission peak was used to monitor the varying *E.coli* concentrations.[101]

Liu *et al.* prepared a sensor for Hg^{2+} detection for the first-time using ruthenium complex N719 conjugated UCNPs (20 mol % of Yb^{3+}, 1.6 mol % of Er^{3+}, 0.4 mol % of Tm^{3+}), with a detection

limit of 1.95 ppb. The N719 was functionalised on the surface of UCNPs using a ligand exchange method. Thus, synthesised N719-UCNPs system shows a broad absorbance at 541 nm, which can be attributed to "ligand to metal charge transfer" of ruthenium complex N719. The addition of mercury ions shifted the absorbance maxima to 485 nm which indicates a strong interaction between N719 and Hg^{2+}. There the emission was gradually quenched due to increasing Hg^{2+} concentrations in the range of 520-540 nm and 650 nm without any change in 801 nm wavelength region.[102]

Wang *et al.* prepared nitric oxide sensor using $NaYF_4$, Yb^{3+}, Er^{3+} upconversion nanoparticles coated with mesoporous silica with a detection limit of 73 nM. The basic sensor principle was LRET between rhodamine dye and UCNPs due to overlapping spectrum. The sensors stability cum biocompatibility in the biological medium and selective permeability of NO was improved using β cyclodextrin coating. The presence of nitric oxide reduces o-phenylenediamine of the rhodamine that induces opening of the spiro ring favoured by strong absorbance in 500~600 nm emission. Therefore NO concentration can be estimated by the decrease in the emission intensity at 560 nm, which cause corresponding colorimetric changes from colourless to pink.[103]

Spectral overlap between UCNPs and gold nanoparticles were capitaliser for various specific sensors. For instance, UCNPs were functionalised with aptamers and forms a FRET pair with complementary strands conjugated on the gold nanoparticles has been developed with 60 nM LOD. Due to complementary matching of the DNA strands on the surface of UCNPs and gold nanoparticles, the fluorescence is quenched. While the analyte mercury ions are introduced, T-T mispairing occurs in the long strand and cause binding of the mercury ions leading, therefore aptamers fold onto itself and fluorescence quenching is restored.

Zhao *et al.* prepared LRET based detection of homocysteine and cysteine as these are the important indicators of disorders like Alzheimer's and cardiovascular disease. Yolk shell upconverting nanoparticles (YSUCNP) were prepared and the cavities were loaded with 8-oxo-8H-acenaphtho[1,2-b] pyrrole-9-carbonitrile, which quenches the green emission by forming a complex with cysteine. This also caused visible colorimetric response from yellow to purple.[104] The schematic representation of UCL turn on and turn off LRET is shown in Fig 1.11.

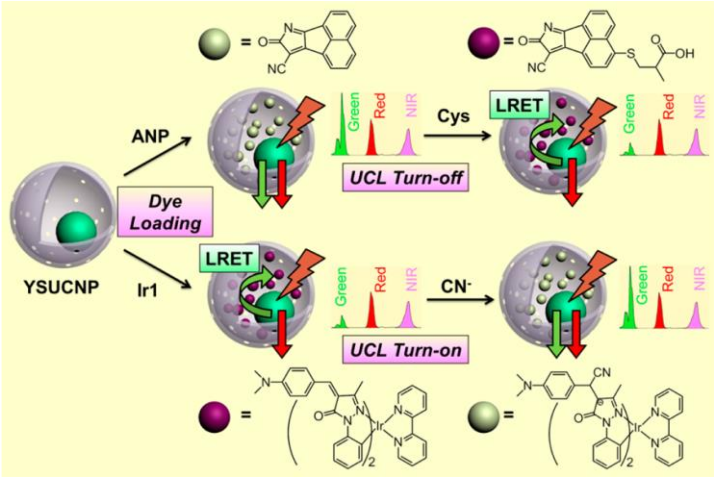

Fig 1.11 Schematic representation of yolk shell upconversion nanoparticles (YSUCNP) turn on-off (upconversion luminescence) in response to cysteine/homocysteine due to luminescence resonance energy transfer (LRET), Reprinted from ref 106, Copyright 2014, American Chemical Society

Recently Ma *et al.* prepared an upconversion sensor using $NaYF_4$, Yb^{3+}, Er^{3+}, Tm^{3+} for the detection of explosives i.e. TNT and TNP ions, which caused selective quenching of either green and violet emission respectively.[105]

Recently, Naghdi *et al.* prepared a 3D smartphone based sensing system for detection of target biomolecules using chitin nanofiber paper containing UCNPs and various colorimetric agents embedded in the 3D network.[106]

1.12 Introduction of Photo-responsive materials and its biological applications:

Photothermal property of various nanomaterials finds extensive applications biomedical field. The photothermal assisted killing of cancer cells has been explored since 18th century. Even in 17th century, the tip of the fire was used to treat breast cancer in many patients.[107]

Cancer is a deadly disease due to abnormal growth and uncontrolled proliferation of cells that pertains in lungs, stomach, liver etc. The effective treatment of the cancer is based on chemotherapy but it has huge side effects like high cost, low bioavailability and poor targeting. Therefore, with the advent of nanotechnology, advanced nanomaterials with optical property have been found to give the luxury of targeted cancerous treatment. In short photothermal particles having extinction in the NIR light that can penetrate deep tissue can sensitise the cells with the particles placed deep to deliver local heat, thereby leading to cell lysis, protein

denaturation and eventually cancerous cell death.[108] The ideal nanomaterial for effective photothermal property includes (a) Small size in the range of 30-200 nm for effective blood circulation (b) Biocompatibility and low toxicity (c) Strong absorbance in NIR region (d) Large molar extinction coefficient (e) High photothermal conversion efficiency.

Precisely photothermal responsive materials include noble metals (Au, Ag, Pd), semiconductors (WO_3, Fe_3O_4), transition metal chalcogenides (CuS, Cu_2Se), transition metal dichalcogenides (WS_2, MoS_2), carbon-based nanomaterials (carbon nanotubes, graphene) and various conjugated polymer. The NIR light consisting of wavelength from 780 nm to 2500 nm comprises of half of the sun's energy.[109]

In phototherapy, apart from photothermal therapy (PTT), another technique called photodynamic therapy is also explored.

The photodynamic therapy involves reactive oxygen species (ROS) assisted killing of the malignant cells, here the sensitizers absorb photons and while relaxation generates ROS.[110] In short during light irradiation photosensitizer absorbs radiation and excites the molecule from ground state to excited state and undergoes spin orbital coupling to triplet state. Then the triplet state excited molecule interacts with oxygen to form ROS. In case of photodynamic therapy, the wavelength of light used varies from 400-800 nm. The dye that can generate ROS with the NIR excitation is preferred since NIR can penetrate deep into the tissue. The mechanism of photodynamic therapy is shown in Fig 1.12.

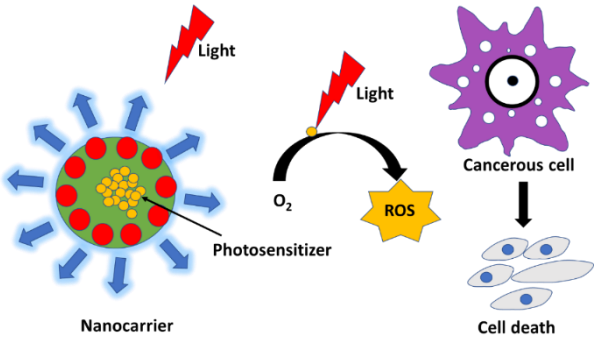

Fig 1.12 Mechanism of cell's response to photodynamic therapy. In this case the photosensitizer absorbs the radiation and generates ROS that leads to cell death.

Similar practical applications have been realised in inhibiting the growth of bacterial biofilms.[111] The photothermal property of the nanomaterials has also been realised in seawater desalination and wastewater purification thereby representing green and sustainable solutions.[112]

1.13 Mechanism of photothermal conversion:

With respect to light matter interaction the photothermal mechanism can be well explained using different principles like

1. **Localised plasmonic heating of metals**
2. **HOMO-LUMO excitations**
3. **Basis of electron-hole generation**

1.13.1 Localised plasmonic heating of metals: The main mechanism is based on LSPR. During the light irradiation the free electrons gets excited and electrons in the conduction band oscillate at a typical frequency that may resonate with wavelength based on different factors. Thus, excited electrons decays by two processes.

One is the radiative decay transition, which plays a major role in the plasmonic associated enhancement of the local electric field; whereas the non-radiative transition is associated with localised plasmonic associated heating. In the localised plasmon associated heating Au or Ag has been found to be effective; and can be tuned to the requirements by changing shape, size, composition, dielectric properties and also the interparticle distance.[113] The metal nanoparticles are used, owing to its optical field enhancement that cause strong absorption and scattering of light, which is responsible for the photothermal conversion and imaging efficiency.[114]

1.13.2 HOMO-LUMO excitation: The HOMO-LUMO excitation in the carbon-based nanomaterials like graphene and polymeric samples plays a major role in heat generation, due to its ability to convert the incoming photons to lattice vibrations. Therefore, when these materials are illuminated the loosely bound electrons in the π orbitals are excited to π* that comes in low energy spectrum.

1.13.3 Electron-Hole generation: The electron-hole generation usually occurs in semiconductors. As these nanomaterials are excited with the energy equal or greater than the bandgap, this excites the electrons in the valence band to conduction band and leaves hole vacancies in the valence band. The excited electrons can decay radiatively or non-radiatively. The non-radiative transition is closely associated with the crystal lattice vibrations and therefore generates heat. A gradient of temperature is established over the complete surface of the nanomaterial by charge carrier diffusion and recombination.[115]

The most basic criterion or requirement in the photothermal therapy is the ability of nanomaterials to possess a wide absorption cross section in the light radiation and laser for effective stimulation. The gradual increment in the local surrounding temperature is totally governed by nanomaterial properties, size, absorption coefficient and power of the radiation source. [116] Given this flexibility to tune, often attempts were made to have the material absorbance at NIR range due to its deeper penetration.

1.14 Nanomaterials for photothermal applications:

1.14.1 Gold nanoparticles: Gold has been realised as a biocompatible material and has been used for centuries for its extraordinary properties to treat various kinds of ailments.

For example, Robert Koch found out that gold cyanide is effective to kill tuberculosis causing bacteria.[117] Similar, study by Jacques Forestier in 1890, led to the discovery of anti-inflammatory properties in gold compounds and found that it is a useful drug to treat rheutemoid arthritis.[118] Also gold quality is effective for its use in surgical implants, pacemaker and stents.[119]

Gold nanoparticles has been used since 19th century for genomics, gene therapy[120] and plasmonic photothermal therapy. In plasmonic photothermal therapy targeted cancerous cells ablation,[121–123] selective bacterial destruction and treatment of viruses including HIV is made possible.[124]. The gold nanoparticles possess size dependent suitability for medical application, for instance Au NPs less than 20 nm show the ability to cross the blood brain barrier and gold nanoparticles less than 5 nm show excellent renal clearance.[125]

Advantages of photothermal effect in Au NRs:

a) Side effects associated with chemotherapy is reduced.

b) Treatment is targeted to solid tumours instead of the off-target healthy cells.

In addition to gold nanoparticles, carbon nanomaterials, polymers etc. are also explored for its photothermal applications. However, gold has been realised as most promising material for cancer treatment due to its anisotropic nature, tuneable aspect ratio for absorbance in the NIR region. Gold nanoparticles in particular the nanospheres of ~13 nm size has an absorbance in the range of 520 nm.[126] For example, the gold nanospheres of 40 nm shows a greater absorption coefficient (10^5) than any other light absorbing dye molecules.[127] The increase in the particle size also led to the proportional red shift and cause an absorbance in the NIR region. Also, the

shape of these nanomaterials can be tuned for its effective absorbance in the NIR region. Gold in the form of nanospheres, nanorods, prism, cube, shells etc. has already been explored for tailoring its absorbance in NIR region.

Currently, PEG coated silica 150 nm Au nano shells is under clinical trials developed by Nanospectra Biosci. Inc. (ClinicalTrials.gov Identifiers: NCT02680535) for Aurolase therapy, which is a type of PTT. The retention of Au nano shells is due to the phenomenon of enhanced permeability and retention effect of the cancer cells, which is due to the presence of leaky and poorly organised tumour blood channels. Halas *et al.* was the first one to demonstrate the gold nanoparticles based photothermal therapy using gold nano shells. The SPR absorbance of the prepared Au nano shells can be tuned in NIR range by changing the silica core and gold shell thickness.[122] Later on, Mustafa El Sayed prepared gold nanorods with correct aspect ratio for tuning in the absorbance to NIR range. In special case of nanorods, two types of surface plasmons are present,[128,129] that cause two UV-VIS absorbance peaks, which corresponds to longitudinal and transverse plasmon. By changing the aspect ratio of the gold nanorods the NIR absorbance peak can be tailored for its effective response in cancer photothermal therapy.[130]

The application of organic fluorophores for photothermal therapy is limited by its instability in aqueous solutions.[131] Jingyi *et al.* prepared gold nanocages having a tuneable light absorption in 500-880 nm for the photothermal destruction of cancer cells. However, the limitation of utilising these gold nanoparticles for *in vivo* drug release and photothermal property is its cytotoxicity caused by CTAB, which is used for the shape control and tuning the aspect ratio for its effective absorbance in the NIR wavelength regime.[132] The comparison of varying aspect ratio of Au nanorods and its corresponding UV-VIS spectra is shown in Fig 1.13.

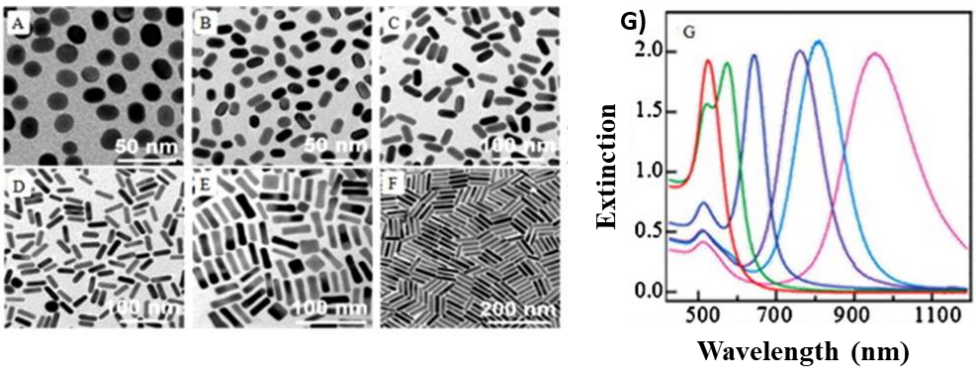

Fig 1.13 TEM images of Au NRs with varying aspect ratio (A-F) and corresponding UV-VIS spectra (G) Reprinted from Ref 139. Copyright 2013, Elsevier

It is even observed that 23% of dogs[133] die of cancer and the deaths in dogs is more in comparison to other feline patients.[134] Ali *et al.* treated mammary gland cancer in cats and dogs through photothermal therapy, by injecting Au NRs into the mammary glands through intra-tumoral route followed by NIR irradiation. This Au NRs injection and irradiation were followed for three times, and the tumour regression follows thereafter.[135] Abdoon *et al.* performed similar experiments for the treatment of mammary glands cancer.[124] London *et al.* observed partial remission of cancer by giving photothermal therapy to seven canine patients, using Au NRs injection, 72 hours prior to the exposure of NIR laser for irradiation of tumour mass.[136]

The gold nanoparticles have been widely used in the photothermal therapy owing to its biocompatible nature. However, some literature has contradictory results owing to the nature of ligands on the surface, and the power of laser used for the treatment etc. It has also been observed that the photothermal efficiency is directly related to the size of the gold nanoparticles using the Mie theory. As smaller Au NPs display higher photothermal efficiencies.[137] The comparison of photothermal efficiency in response to varying diameter of Au NPs is shown in Fig 1.14A. The gold nanorods exhibit a higher effectiveness of photothermal efficiency as it shows a higher absorption efficiency in comparison to gold nanoshells as shown in Fig 1.14B and Fig 1.14C. Similarly, Skrabalak *et al.* prepared Au nanocages for photothermal destruction of cancer cells in 2007. These particles were synthesized by the galvanic replacement of silver nanocubes with gold ions; by carefully controlling the titration volume, the SPR absorbance wavelength can be tuned anywhere between 600-1200 nm.[138] It is of prime importance to note that the content of Au is extremely important for tuning its SPR range.

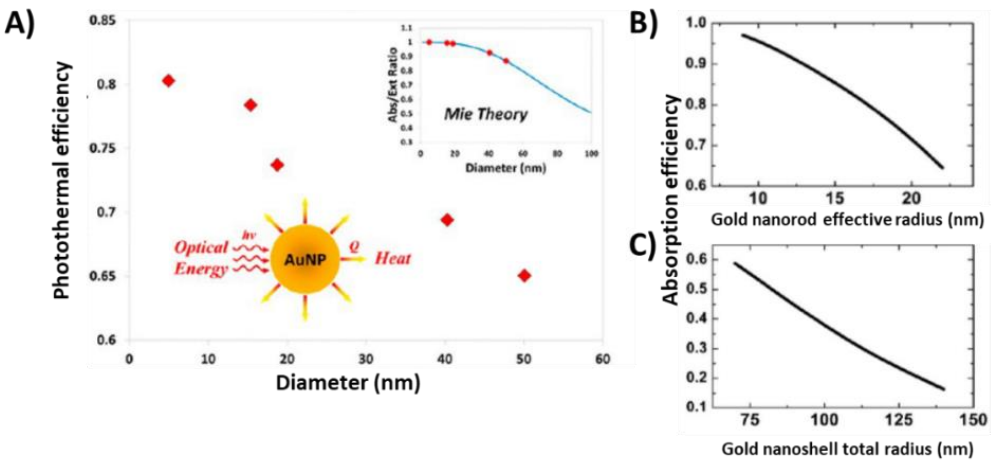

Fig 1.14 A) Effect of gold nanoparticles on the photothermal efficiency calculated using Mie theory in inset. B and C depicts the effect of gold nanorods and gold nanoshell respectively, on

the absorption efficiency which is indirectly proportional to the size of the gold nanorod or the nanoshell. Reprinted from ref 144, Copyright 2019, American Chemical Society.

Ye *et al.* prepared Au nanocrosses for efficient photothermal response owing to its large absorption cross section 7.5 x 10^{-15} m^2 in NIR wavelength range through anisotropic growth in <110> and <001> direction in contrast to the gold nanorods which growth in either of <110> or <001> direction. It is of interest to note that the absorption coefficient of these nanocrosses was higher than that of Au nanospheres even in the size range of 40-150 nm, which makes their applications useful for photothermal destruction of cells. This is accomplished due to the fact that the entire nanocross gets excited even when one of the branches is excited with incident light. The TEM images of Au nanocrosses is shown in Fig 1.15.[139] The image in Fig 1.15A is with D_{2h} symmetry. It was interesting to observe that if the doubly twinned nanocrosses were viewed along <110> zone axis, the lattice direction remains the same in the twinned boundary as shown by SAED in Fig 1.15B.

Even though there are a wide variety of Au NPs available for targeted photothermal applications, there are contrary reports on the use of these NPs. In some cases, even if the Au NPs were proved to be compatible, other components like the NIR laser used,[140] non-compatible surface ligands[141] and high treatment dosage of Au NPs raise the question. Another issue accompanied by Au NPs is that they accumulate in liver and spleen. Further in PTT treatment the efficiency varies from lab-to-lab because of the inconsistency in laser dosage. These inconsistencies are associated with different outcomes thereby causing large variations in PTT.

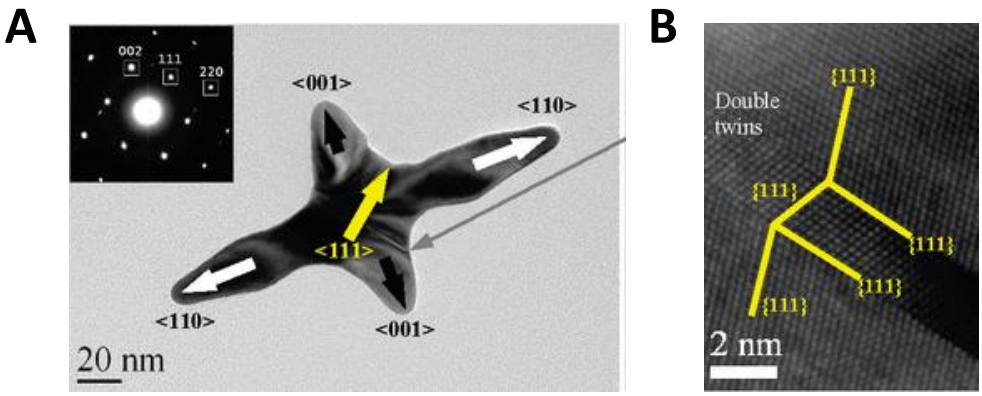

Fig 1.15 Low magnification and high magnification TEM and HRTEM images of Au nanocrosses with D_{2h} symmetry synthesized along both <110> and <001> direction. The nanocrosses were studied for its effective photothermal therapy owing to the plasmonic nature

of gold. The inset in Fig 1.15A shows one set of the SAED pattern of the nanocrosses. Reprinted from Ref 146, Copyright 2011, American Chemical Society

1.14.2 Palladium nanoparticles: The major limitation of the Au nanocrosses is that they suffer from poor photothermal stability and loss its structure upon subsequent laser exposure. Therefore, due to the reduced photostability of gold, palladium nanostructures that have high melting point were explored. Therefore, Huang *et al.* synthesized hexagonal palladium nanosheets, having intense LSPR absorbance (molar extinction coefficient 4.9 x 10^9 M^{-1} cm^{-1}) almost similar to the gold nanorods (5.5 × 10^9 M^{-1} cm^{-1}). Most importantly the nanostructured shapes of palladium are not distorted due to high energy NIR irradiation. In a similar study of palladium, nanocorolla was synthesized using etching growth strategy, which gave a temperature increase from 26 °C to 50 °C.[142]

Other photothermal nanomaterials: Apart from gold and palladium, there are other photothermal materials namely carbon based, semiconductor, metal NPs and transition metal chalcogenides. In carbon the 2D materials have a unique property of thickness dependent band gap. Similarly, in semiconducting materials the band gap of black phosphorus was simply tuned by fabricating different number of layers or thickness of black phosphorus. The transition metal dichalcogenides has a typical large bandgap (~1-2.5 eV) and can be used for absorption of short wavelength of light.

1.14.3 Carbon based nanomaterials: Carbon based nanomaterials typically comprise of 0D (fullerene), 1D carbon nanotubes and 2D graphene nanomaterials. Amongst various carbon materials such as graphene, graphene oxide/reduced graphene oxide, carbon nanotubes are used for the photothermal applications due to its wide tunability in the NIR wavelength regime and possessing an excellent light to heat conversion efficiency.[143–146]

1.14.3.1 Carbon nanotubes*:* Carbon nanotubes are similar to the graphene sheets rolled into a tube. Based on the angle of rolling, the carbon nanotubes are structurally classified as armchair or zigzag or chiral; and it may have both sp^2 and sp^3 hybridized bonds, which depends on the degree of defects. These carbon nanotubes can be classified as single walled or multi walled based on the number of layers being rolled. Single walled carbon nanotubes consist of single graphene sheet rolled having a diameter of 1-3 nm. In case of multi walled carbon nanotubes, multiple sheets are rolled up to form multiple walled carbon nanotubes. The diameter varies between 2-100 nm and length varies from 0.2 µm to several microns. The photosensitizers are coupled with carbon nanotubes for complementary action. The

bioavailability and solubility helps in efficient and targeted cancer treatment.[147] For example, PEG grafted SWCNTs is able to show photothermal effect under the laser irradiance at 808 nm wavelength resulting in significant photothermal property.[148] Similarly various kinds of modifications were carried out to improve the photothermal property of multi walled carbon nanotubes.

The advantage of using these carbon-based nanomaterials is associated with the low cost and abundance. In these nanostructures hyperconjugation in the π orbital increases the absorbance in the NIR spectral range.

1.14.3.2 Graphene Oxide*:* Graphene oxide is a 2D material having a basal planar structure with one atomic layer thickness (~0.35-1.6 nm per layer) having sp^2 hybridized carbon atoms. These carbon-carbon atoms are arranged in honeycomb crystal network.[108] The graphene oxide contain many carboxyl, hydroxyl and epoxy functionalities, which improves its dissolution in water. Graphene oxide is a low cost, biocompatible and it's synthesized from graphite and finds applications in energy [149], electronics[150] ,molecular sensing areas [151] and catalysis.[152] Various other functionalities are introduced in graphene oxide to make it hydrophilic, which includes moieties like nitrogen doping [153], hydroxyl or carboxyl groups.[154] Graphene oxide have enormous surface area, which makes it an ideal nanocarrier for various drug carrier applications. Graphene oxide can be loaded with huge number of drugs compared to other nanomaterials, because of its favourable high surface area, π-π stacking and hydrophobic interactions. Graphene oxide also shows plasmonic effect having a good absorbance in NIR region and that generates heat via the photothermal route. Graphene oxide has also been studied for improved cell adhesion properties. For example, recently GO embedded PEG based cryogels has been proven for its improved cell attachment, owing to its improved signalling pathways and therefore improving the cell viability. This demonstrates importance of graphene oxide in cryogenic system as an effective scaffold to control osteogenic commitment of stem cells.[155,156]

Liu *et al.* prepared pegylated graphene oxide for its applications in photothermal applications for in vitro drug delivery. High doses of graphene oxide were injected, which approximates to 20 mg Kg^{-1}, and then illuminated using high laser powers of ~2 W cm^{-2} for the targeted drug delivery. The high laser power is required due to its suboptimal absorption of NIR light under oxidized conditions; in comparison the carbon nanotubes use lesser power.[152,157] Robinson *et al.* for the first time prepared reduced graphene oxide conjugated with non-covalently bound

PEG, which leads to an increase in NIR absorbance by 6 folds owing to partial restoration of the aromatic and conjugated character of graphene sheets.[158] Thus, reduced GO has comparable properties in absorbance to photothermally active gold and carbon nanotube materials.

Conclusions: The thesis contain brief description about optically active nanomaterials and their application in food processing, sensing and plant protection. Firstly, light activated nanomaterial that can give UV light for the efficient vitamin D_2 processing has been developed.

Vitamin D_2 is available from dietary sources such as mushrooms, tuna, milk and other non-vegetarian options. The cheapest source is sunlight. Our body contains cholesterol which can be converted to 7-dehdrocholestrol using an enzyme present in the human body. 7-dehydrocholestrol which is present in the skin undergoes conversion to pre-vitamin D_3 in the presence of UV light present in the sunlight. The pre-vitamin D_3 then undergoes hydroxylation in two steps in kidney and becomes the active form of vitamin D_3 which can be quantified using laboratory tests. A person is considered to be deficient if the concentration of 1, 25-dihydroxy vitamin D_3 is less than 20 ng mL^{-1}. The only vegetarian source for vitamin D_2 is mushrooms. Upconversion nanoparticles owing to anti stokes emission can be used for conversion of ergosterol to vitamin D_2 in mushrooms.Upconversion nanoparticles are lanthanide ions embedded in the inorganic crystal lattice. These nanoparticles follow anti-stokes emission which contrast with other conventional fluorophores. Major advantage of the use of upconversion nanoparticles is its resistance to photobleaching, photostable nature, tuneable emissions (with different dopant ions) and most important deep tissue penetration which makes it a successful nanomaterial in photothermal/photodynamic therapy and sensors.

Finally, there is a wide variety of photothermal nanomaterials like gold, silver, palladium, carbon nanotubes and graphene oxide. However, gold has been realised as most promising material for cancer treatment due to its anisotropic nature, tuneable aspect ratio for absorbance in the NIR region. Another important photothermal material is a 2D material i.e., graphene oxide that has an enormous surface area, which makes it an ideal nanocarrier for various drug carrier applications. It can be loaded with huge number of drugs compared to other nanomaterials, because of its favourable high surface area, π-π stacking and hydrophobic interactions. Graphene oxide also shows plasmonic effect having a good absorbance in NIR region and that generates heat via the photothermal route. The nanomaterial (graphene oxide) has been used to develop the pheromone composite that can deliver the pheromone with the light stimuli and make the composite a sustainable deliver system.

Chapter 2

Food Processing

Upconversion nano-device assisted healthy molecular photo-correction

Abstract. Mushrooms are rich in ergosterol, a precursor of ergocalciferol, which is a type of vitamin D_2. The conversion of ergosterol to ergocalciferol takes place in the presence of UV radiation by the cleavage of "B-ring" in the ergosterol. As the UV radiation cannot penetrate deep into the tissue, only minimal increase occurs in sunlight. In this study upconversion nanoparticles, with the property to convert deep penetrating near-infrared radiation to UV radiation have been cast into a disk to use sunlight and emit UV radiation for vitamin D_2 conversion. Engineered UCNPs disk with maximum particles and limited clusters demonstrates ~2.5 times enhanced vitamin D_2 conversion.

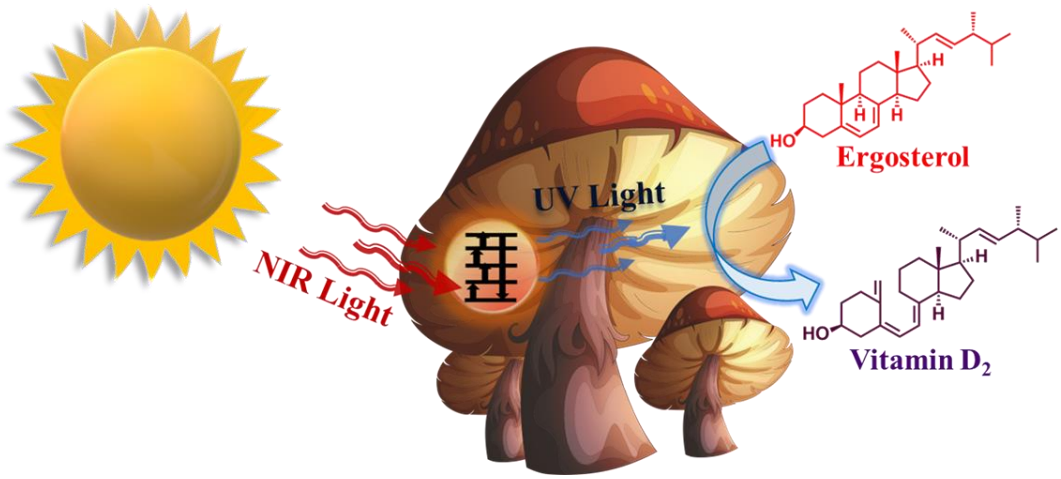

TOC: Schematic showing the conversion of ergosterol to vitamin D_2 using UCNPs coated disks in mushrooms.

2.1 Introduction

Vitamin D is an important nutrient to maintain calcium homeostasis and a healthy immune system. The vitamin D deficiency is measured by quantifying the 25-hydroxy vitamin D content in the blood serum.[32] Any count less than 20 ng mL^{-1} is considered deficient, which is further graded as mild moderate severe at 10-20, 5-10, <5 ng mL^{-1} respectively. Recently, it

has been found that vitamin D plays an important role in the control of heart disease, type I diabetes, multiple sclerosis, stroke, infectious diseases, cancer and Crohn's disease, etc.[6,10,159] The UV radiation in solar light initiates the conversion of 7-dehydrocholesterol present in the human dermal region to pre-vitamin D_3, which then converts into vitamin D_3 spontaneously; hence popularly called the sunshine vitamin.[160] Generally, the population that resides in the polar latitudes shows vitamin D deficiency, especially in the winter seasons, due to the lower UV radiation in the solar spectrum (the lowest detectable wavelength has been 300 nm). The severity gets intense due to the thick winter clothes, which limits the penetration of the radiation.[161] To be precise, the pro-vitamin D_3 to vitamin D_3 conversion after 1 hour of sunlight exposure on a cloudless day in January, between 18°N and 34°N latitude, was measured to be 10 and 3% respectively.[161,162] Hence in low sunshine locations, ~50% of young, pregnant women and the aged population were found to be affected by vitamin D deficiency.[163]

The mushrooms contain ergosterol (pro-vitamin D_2), which upon exposure to UV radiation convert into pre-vitamin D_2, followed by isomerization to vitamin D_2 (Scheme 1).[164] Vitamin D_2 has been found as effective as vitamin D_3 to maintain serum vitamin D derivative concentration.[32] The conversion of ergosterol into vitamin D_2 upon the UV-B and UV-A radiation has been realized in many edible mushrooms such as button, oyster, shiitake, and abalone. This conversion was found to accompany the synthesis of isomers *viz*., lumisterol and tachysterol.[42,165] The effect of location, *i.e*., polar to show less amount of vitamin D conversion in humans, has also been observed in mushrooms.[166] Highlighting the fact that UV radiation cannot penetrate deep tissue efficiently, the mushroom placed with lamella (bottom of the mushroom cap) facing the irradiation showed greater conversion than the thick pileus side.[54]

The UV irradiation technique to enrich vitamin D_2 in mushrooms is already in practice on a commercial scale.[40,167] However, the present process has the following limitations. 1. UV light requirement; 2. The inability of UV to penetrate deep into the tissue; 3. The short shelf life of

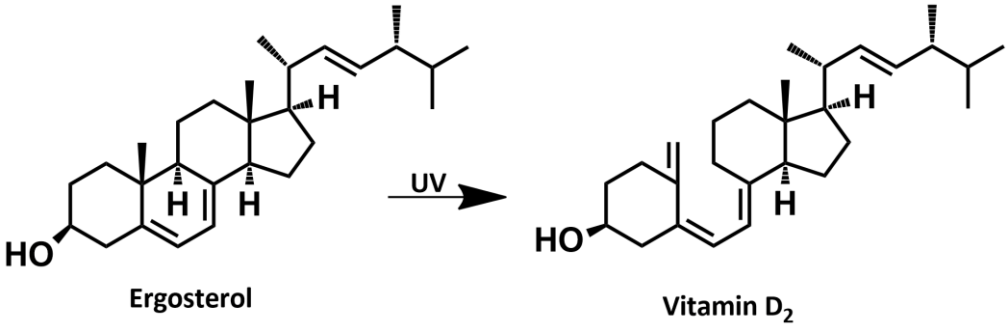

Scheme 1. Scheme demonstrates the mechanism of conversion of ergosterol to vitamin D_2 in the presence of UV light in mushrooms (200-400 nm). In the presence of UV light there is cleavage of B ring in the ergosterol which leads to the formation of Vitamin D_2.

vitamin D_2, in both cold storage or freeze/hot air dry processing.[54,166] Low energy wavelength assisted molecular correction to restructure collagen was demonstrated recently.[168] However, for vitamin D synthesis UV light irradiation is essential, hence a simple device is required that can convert deeper penetrating radiation to UV can aid in the enhancement deep inside the mushroom.

Functional materials such as optical nanomaterials are gaining significant importance across disciplines.[169–172] In biology, near infra-red (NIR) sensitive nanoparticles were found to play an important role due to its deep penetration.[173] NIR assisted 2 photon fluorescence is an interesting phenomenon, which has been documented in magnetic particles such as iron oxide nanoparticles with specific ligands. [174] The upconversion nanoparticles (UCNPs) are an important optical material with the ability to convert NIR into UV by anti-stoke emission.[175,176] In biology UCNPs has gifted the luxury of deep tissue penetration, UV activated opening of

drug gates,[177] folates target activation, [178] photodynamic therapy [179] in bone cell monitoring [180] and in-vivo cancer imaging,[181] etc.. But the UCNPs has not found application in food and nutrition studies so far to our knowledge, exceptions are the sensors.[182,183] Hence, the objective of the present study is to develop, the UCNPs disk having maximum UV emission, to plug into the mushroom for efficient ergosterol to vitamin D_2 conversion with the assistance of solar irradiation. The casting of UCNPs into a disk pose engineering challenge, hence needs careful optimization as in case of fibers.[184] Here with the simple spin coating method, we have arrived at maximum particles number and minimum cluster number for maximum vitamin D conversion efficiency at lowest UCNPs concentration. The UCNPs are not toxic by themselves even upto 1000 ppm,[178,185] further, the trace toxicity may also be ignored, as the UCNPs are cast into a disk that can be detached after the irradiation process.

2.2 Material Methods

Octadecene (Sigma Aldrich), Oleic acid (Sigma Aldrich), Yttrium acetate (Sigma Aldrich), Ytterbium acetate (Sigma Aldrich), Thulium acetate (Sigma Aldrich), Ergosterol (Alpha Aeser), vitamin D_2 (Calciferol), sodium hydroxide (Sigma Aldrich), ammonium fluoride (Sigma Aldrich), ethanol, ascorbic acid (TCI), potassium hydroxide (Sigma Aldrich), acetonitrile (HPLC grade), methanol (HPLC grade), pentane (TCI), pectin (SRL), chitosan (SRL), circular quartz coverslips 10 mm diameter (Agar scientific), and white button mushrooms (*Agaricus bisporus*).

2.2.1 Synthesis of β-$NaYF_4$:Tm^{3+} 0.5 mol %, Yb^{3+} 30 mol % nanoparticles

The upconversion nanoparticles with Tm^{3+} 0.5 mol %, Yb^{3+} 30 mol % doping in the β-$NaYF_4$ host was synthesized by following the reported method with minor modifications.[186] Briefly, a round bottom flask containing 2.8 mmol $Y(CH_3COO)_2$, 1.2 mmol Yb $(CH_3COO)_2$ and 0.02 mmol Tm $(CH_3COO)_2$ in 7:3 volume of octadecene and oleic acid was heated to 120 ºC under

vacuum for 30 minutes to form lanthanide complexes. Afterward, the reaction temperature was allowed to cool to 70 ºC and then placed under a gentle flow of nitrogen gas. Following, a further decrease in the temperature, a solution of 16 mmol ammonium fluoride and 10 mmol sodium hydroxide prepared in methanol at ~1:1 ratio was injected into the above aliquot, so that the final volume reached 1.5 times the initial volume. The resultant solution turned turbid, which was stirred for another 30 minutes at 50 ºC. Following this, the temperature of the reaction mixture was raised to 80 ºC to distill out the methanol. Furthermore, the temperature of the reaction mixture was raised to reach 300 ºC quickly and maintained at this temperature for 90 minutes under nitrogen gas flow. After 90 minutes the mixture was allowed to cool and reach room temperature. The particles were precipitated by adding acetone/ethanol and centrifuged at 7,000 rpm for 10 minutes to pellet down the particles. The resulting pellet was dispersed in a 1:3 ratio of hexane: ethanol mixture to wash and remove the unreacted components. The UCNPs were then stored in a minimal amount of hexane for further use.

2.2.2 Characterization

The powder X-ray diffraction (XRD) patterns analysis was carried using Bruker D8 advance diffractometer with Cu kα radiation source (λ=1.5406) at 40 kV and 50 mA. The transmission electron microscope (TEM) and high-resolution TEM (HR-TEM) images were performed using JEOL JEM-2100 (200KV Microscopy). A bruker multimode 8 AFM system has been used for AFM height profiling and particles measurement on the disc containing $NaYF_4$, Yb^{3+}, Tm^{3+} nanoparticles. The photoluminescence spectra were measured using the Fluoromax-4 spectrofluorometer (Horiba Scientific) equipped with a 980 nm laser excitation. An ultraviolet (UV) lamp (Power 250 Watt) was used to trigger the conversion in the mushroom. A Nanodrop spectrometer (GE healthcare Nano Vue Plus) was used to check the absorbance, spin coater spin NXG-P2 (Apexic India) was used for effective coating of upconversion nanoparticles onto

the quartz coverslip. A solar simulator (Oriel LSS-7120 solar simulator) was used to mimic solar irradiation. High-Performance Liquid Chromatography (HPLC) quantification was carried out using the Waters instrument.

2.2.3 Ergosterol conversion in aqueous solution

The as-prepared hydrophobic UCNPs disperse in non-polar solvents *i.e.*, hexane or chloroform, which differs from solvent that can be compatible to ergosterol. Hence the UCNPs were coated with amphiphilic biopolymer that can disperse the UCNPs in aqueous media. To choose the biopolymer that cause minimum quenching of emission fluorescence 2 biopolymers *viz*., pectin and chitosan coated UCNPs were prepared, and their spectra was recorded.

2.2.4 Coating of UCNPs

2.2.4.1 Pectin coating

Approximately 50 mg paste weight of UCNPs was dispersed in hexane and then added to 2 % pectin solution prepared in an acetate buffer followed by sonication. This mixture was allowed for overnight incubation under stirring at room temperature for the solvent evaporation and phase transfer of the particles to aqueous portion with pectin coating. The particles were centrifuged (7,500 rpm for 15 minutes) and washed three times with Milli Q water (UCNPs@pe).

2.2.4.2 Chitosan coating

Approximately 50 mg paste weight of UCNPs was dispersed in hexane and then added to 2 % chitosan solution prepared in acetate buffer followed by sonication. This mixture was kept for overnight incubation under stirring at room temperature for the solvent evaporation and phase

transfer of the particles to aqueous portion with pectin coating. The particles were centrifuged (7,500 rpm for 15 minutes) and washed three times with Milli Q water (UCNPs@ch).

2.2.5 Kinetics of ergosterol conversion

The effect of coating on the upconversion emission spectra was studied and it was found that the chitosan coating caused minimum quenching. Hence the UCNPs@ch was used to study the kinetics of ergosterol conversion. The UCNPs@ch and ergosterol solution was prepared in methanol at yttrium and ergosterol concentration of 37 ppb and 0.5 mM respectively; this aliquot was incubated under the selective NIR illumination from the solar simulator (only the NIR light source (900-1100 nm wavelength). The kinetics of ergosterol conversion was followed with the absorbance spectra measured at definite intervals using the nanodrop instrument.

2.2.6 Kinetics of ergosterol to vitamin D conversion in mushroom

2.2.6.1 Mushroom sampling

The vitamin D_2 content was estimated in white button mushrooms *i.e.*, *Agaricus bisporus*. These mushrooms were purchased from an identified farmer's farm, where the mother culture of *Agaricus bisporus* has been maintained. For the estimation of vitamin D_2, the mushrooms were freeze-dried using lyophilizer and crushed into powder for the vitamin D_2 analysis.

2.2.6.2 Irradiation of mushroom with UV light

In the mushrooms, the stipe (stem portion) was removed and the remaining pileus (head portion) was placed under UV lamp (Power =250 W, Hg lamp) for 2 hours under the irradiation at a distance of 10 cm, in such a way that the lamella faced the irradiation source. After 2 hours of incubation, the mushrooms were cut into pieces and lyophilized to powder for vitamin D_2

extraction and estimation. The mushrooms without any irradiation were used as the control for comparison.

2.2.7 Coating onto the quartz coverslip

UCNPs were dispersed in hexane to prepare a solution with 400 ppb yttrium concentration, the concentration was measured using Inductively Coupled Plasma Mass Spectrometry (ICP-MS) (Agilent). This solution was spin-coated on a quartz coverslip of 10 mm diameter from Agar Scientific using 150 µL volume of solution. The spin coater NXG-P2 (Apexic India) was operated at 200 rpm for 40 seconds followed by the second round at 500 rpm for one minute, (as the initial high-speed spun of 500 rpm causes the material to spill out, hence the initial low speed of 200 rpm was adopted). The coating was carried out on three similar discs with the same quantity of material.

2.2.8 Irradiation of mushroom in the solar simulator

The mushroom stipe was removed and three UCNPs discs were inserted in between the lamella of the mushroom. This set up was placed at a distance of 10 cm from the light source of the solar simulator upto 2 hours and shined using only the NIR light having 900-1100 nm radiation switched on. The intensity of the irradiation was measured and recorded as 35 mW cm^{-2}. The control mushrooms without UCNPs disk were also kept for the irradiation for upto 2 hours under NIR light with the wavelength range of 900-1100 nm using the solar simulator. After the irradiation, the mushrooms were subsequently lyophilized, and vitamin D_2 was extracted for the HPLC analysis.

2.2.9 Irradiation of mushrooms using 980 nm laser

Three UCNPs disks were inserted in the mushroom and shined using the 980 nm laser with 2W power intensity for 20 minutes on each disc. After the irradiation, the mushrooms were subsequently lyophilized, and vitamin D_2 was extracted to analyze under HPLC.

2.2.10 Extraction of vitamin D_2 from mushroom

Vitamin D_2 analysis was carried out following the reported protocol with minor modifications.[43] Briefly, 0.5 g of lyophilized mushroom powder was refluxed at 80 ºC for 1 hour in a mixture of 4 mL of 0.99 mM ascorbic acid solution in 100 mL of 1M NaOH solution, 50 mL of absolute ethanol and 10 mL of 50 % KOH for saponification. The sample mixture was allowed to cool to room temperature and decanted. To this aliquot 30 mL of a 50 % ethanol was added and transferred to separating funnel. From this solution, vitamin D_2 was extracted with three washings of n-pentane using 50 mL, 50 mL and 20 mL volume in each separation. This organic portion was removed by further three washing with 50 mL of 3 % KOH in 5 % ethanol and deionized water until it becomes neutral. Following this, the resultant was evaporated to dryness using rotavapor and then re-dispersed in acetonitrile to inject into the HPLC column. For the injection, 30 µL of the solution was used and eluted through the reverse phase C18 column fitted in HPLC instrument, with acetonitrile/methanol in gradient flow as the mobile phase at a flow rate of 1 mL min^{-1}. The eluted compounds were detected using the UV detector configured at 265 nm. Vitamin D_2 was determined with the retention time of the standards; and the concentration was quantified using the calibration curve. The standards of calciferol solution were prepared in acetonitrile and used for the preparation of the calibration curve.

2.3 Results and discussion: In this study, upconversion nanoparticles (UCNPs) were used as the UV sensitizer source in the mushroom for the efficient conversion of ergosterol into vitamin D_2 with the assistance of sunlight. UCNPs with thulium and ytterbium doped β-$NaYF_4$ host ($NaYF_4$: 0.5 mol % Tm^{3+}: 30 mol % Yb^{3+}) were synthesized in oleic acid by following the method reported by Yan *et al*. with minor modifications and dispersed in hexane.[186] Here the Yb^{3+} and Tm^{3+} doping is chosen as sensitizer and activator respectively, and Tm^{3+} is indispensable for the UCNPs to give UV emission (especially $^1I_6 \rightarrow {}^3H_6$). [187–191] The β-$NaYF_4$ is the most tested and accepted host for being with least phonon energy (~350 cm^{-1}) that minimize the non-radiative energy loss and lead to maximum luminescent quantum yield and high emission intensity. With β-$NaYF_4$ host and (Yb^{3+}/Tm^{3+}) elements fixed, different ratios of doping were tested and eventually we found that ratio of $NaYF_4$: 0.5 mol % Tm^{3+}: 30 mol % Yb^{3+} given in the reference to give the maximum UV emission, which is important for the ergosterol conversion. The quantum yield for the prepared $NaYF_4$, Yb^{3+}, Tm^{3+} is between 0.2-0.8.[192] Higher density of dopant has been known to cause enhanced energy resonant cross-relaxation and other non-radiative loss, which may be the reason for this optimum concentration to give the maximum emission. The synthesized nanoparticles were characterized using UV-VIS spectrophotometry,

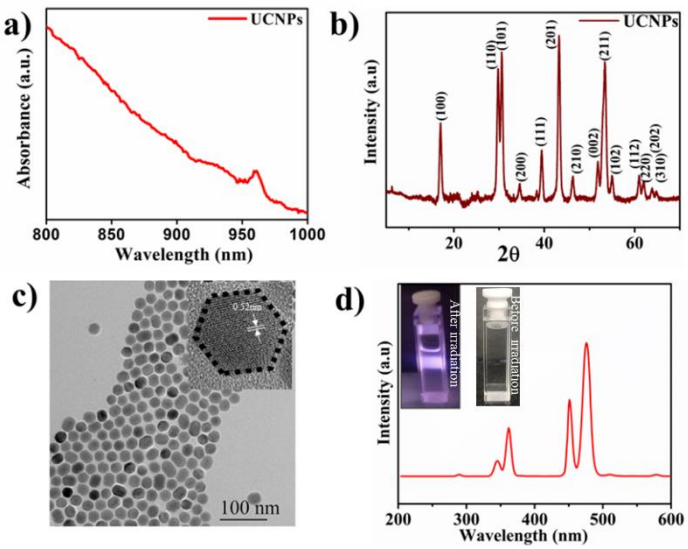

Fig 2.1 Characterization of $NaYF_4$, Yb^{3+}, Tm^{3+} UCNPs (a) UV-VIS-NIR absorbance of the as-prepared UCNPs (b) XRD pattern of $NaYF_4$, Yb^{3+}, Tm^{3+} nanoparticles matching with JCPDS standard card 00-016-0334 (c). TEM image of UCNPs, inset showing HR-TEM image ("d" spacing 0.52 nm, which corresponds to <100> hexagonal phase of the $NaYF_4$ host nanocrystals) and showing hexagonal particle shape (d) Fluorescence spectra of $NaYF_4$, Yb^{3+}, Tm^{3+} particles at the excitation wavelength of 980 nm. Inset shows the fluorescence emission of $NaYF_4$, Yb^{3+}, Tm^{3+} before and after laser irradiation. The photoluminescence spectra of UCNPs ($NaYF_4$:0.5 mol % Tm^{3+}:30 mol % Yb^{3+}) dispersed in hexane, excited using 980 nm is given in Fig 1d.

The absorbance spectra show the typical absorbance of Yb^{3+} ions at 960 nm (Fig 2.1a).[193] The XRD pattern (Fig 2.1b) shows the diffraction peaks matching the hexagonal β-$NaYF_4$ phase (JCPDS standard card 16-0334). The TEM image (Fig 2.1c) shows monodisperse nanoparticles with a size range of 24 ± 3.5 nm. The HRTEM image given in the inset of Fig 2.1c, shows the lattice "*d*" spacing to be 0.52 nm, which corresponds to the <100> hexagonal phase of the $NaYF_4$ host nanocrystals.[194] The upconversion fluorescence emission has been recorded by 980 nm laser irradiation as shown in Fig 2.1d. Inset shows the $NaYF_4$,Yb^{3+},Tm^{3+} Fluorescence spectra before and after laser irradiation. Further the EDX analysis confirms the presence of the doped sensitizer and activator elements. (Fig 2.2)

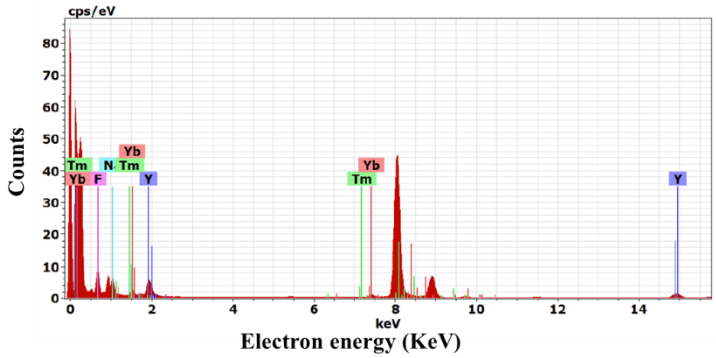

Fig 2.2 EDX analysis of $NaYF_4$, Yb^{3+}, Tm^{3+} doped upconversion nanoparticles.

The emission spectra show characteristic emission peak at 289 nm, 345 nm, 361 nm, 451 nm, 477 nm, 510 nm and 577 nm corresponding to $^1I_6 \rightarrow {}^3H_6$, $^1I_6 \rightarrow {}^3F_4$, $^1D_2 \rightarrow {}^3H_6$, $^1D_2 \rightarrow {}^3F_4$, $^1G_4 \rightarrow {}^3H_6$, $^1G_4 \rightarrow {}^3F_4$ and $^3F_3 \rightarrow {}^3H_6$, respectively as shown in Fig 2.3.

Here, the emission from $^1I_6 \rightarrow {}^3H_6$ and $^1I_6 \rightarrow {}^3F_4$ is our interest as these emission energies contribute to the ergosterol to ergocalciferol (vitamin D_2) conversion. [193,195]

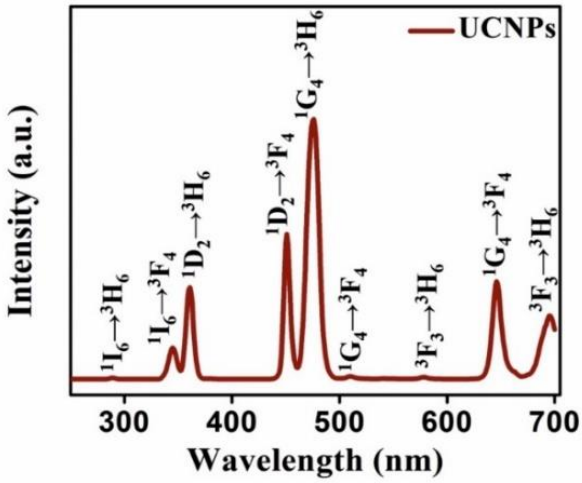

Fig 2.3 Photoluminescence spectra of $NaYF_4$, Yb^{3+}, Tm^{3+} upconversion nanoparticles using 980 nm laser excitation.

2.3.1 Ergosterol conversion

The above synthesized UCNPs were tested for the ergosterol to ergocalciferol (vitamin D_2) conversion. The UCNPs were surface modified to disperse in a solvent in which ergosterol solution can be prepared. Amphiphilic biopolymers such as chitosan and pectin having amine and carboxyl groups respectively were tested for surface modification, to select the modified UCNPs having the least fluorescence quenching for this experiment. The solvent evaporation technique was adopted for the surface modification, where the biopolymers in water wrap and transfer the UCNPs from the hexane to hydrophilic solvents *i.e.*, water during overnight evaporation.[196] The resultant particles showed good aqueous dispersion, which confirms the surface modification of the particles with the polymer. The surface charge measurement

supported this confirmation *i.e.*, the chitosan and pectin coating resulted in +7.63 ± 0.38 mV and -2.57 ±0.128 mv charge indicating the presence of amine and carboxylic groups on the surface of UCNPs respectively (Fig 2.4a). In the photoluminescence measurement, the chitosan-coated UCNPs (UCNPs@ch) showed minimum quenching compared to pectin coated UCNPs (UCNPs@pe) with reference to the emission fluorescence maximum *i.e.*, 475 nm, (Fig 2.4b). In case of chitosan, the coating may be an adsorption phenomenon that wraps the UCNPs with the native oleate capping on the synthesized particles, which will not allow the –OH quenchers from the water to interact.[197,198] Whereas in the pectin coating it may have replaced the oleate. Supporting this the DLS data shows that the chitosan coated UCNPs (UCNPs@ch : ~645 nm), which is >100 nm bigger than the pectin coated UCNPs (UCNPs@pe : ~508 nm). Hence the UCNPs@ch NPs were adopted for the ergosterol conversion. Furthermore, the chitosan modification has been confirmed using the FTIR spectrum analysis (Fig 2.4c). The peaks at 2923 and 2854 cm^{-1} represent C-H stretching from the oleic acid in the as-prepared UCNPs. This C-H stretching disappears in the chitosan-coated samples *i.e.*, UCNPs@ch and a new broad peak around 3300 cm^{-1} appear, which confirms the N-H stretching from chitosan.[178]

The UCNPs@ch and ergosterol were dispersed in ethanol and irradiated using selective NIR illumination from the solar simulator (only the NIR LEDs, λ= 900-1100 nm, were switched on in the solar simulator, all of the other visible radiations were kept off) to test the NIR-assisted ergosterol conversion. This kinetics of ergosterol to ergocalciferol conversion was followed using the absorbance spectrophotometer (Fig 2.4d). Initial ergosterol precursor shows the characteristics of 259.5, 271, 281.5 and 292 nm peaks extending up to 298 nm.[25] Over an increase in the exposure time, the 259.5 nm absorbance peak disappears and the absorbance of pre-vitamin D_2 appears as a hump extending to the absorbance wavelength of 266 nm.

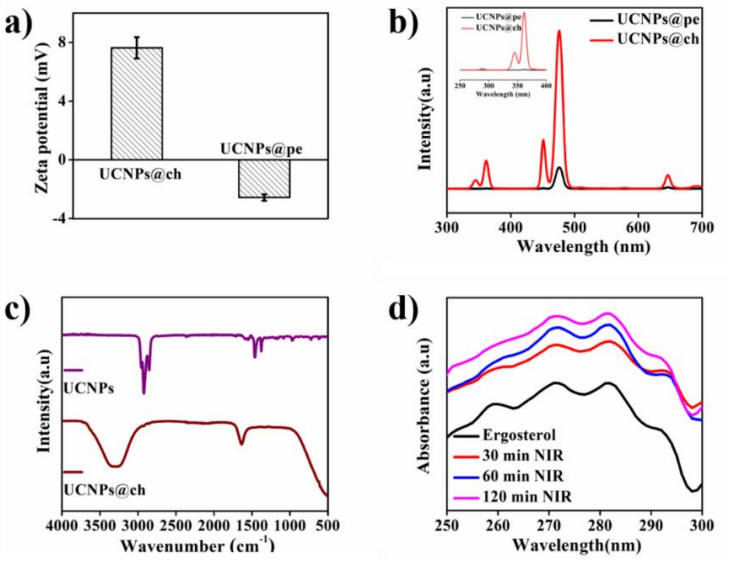

Fig 2.4 Characterization of chitosan and Pectin coated UCNPs (a) Zeta potential showing the surface charge on UCNPs@ch and UCNPs@pe (b) Comparison of fluorescence quenching observed in UCNPs@pe and UCNPs@ch(Inset showing comparison of the fluorescence quenching from 250-400 nm) (c) FTIR spectra of as-prepared UCNPs and UCNPs@ch (d) Kinetics of conversion of ergosterol in presence of UCNPs@ch under solar simulator irradiation followed by UV-VIS absorbance. The absorbance peak of the vitamin D standard and the ergosterol irradiated with the UV light is given in Fig 2.5.

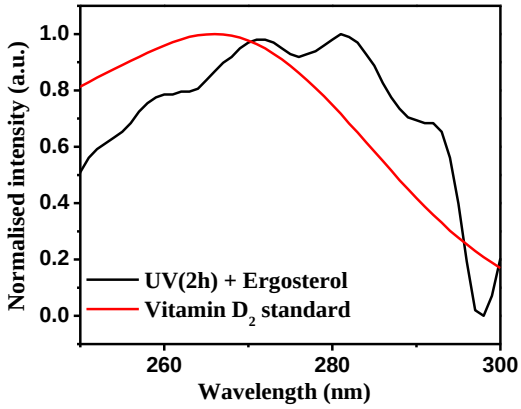

Fig 2.5 UV-vis spectra of vitamin D_2 and conversion of ergosterol in response to UV light irradiation at 200-400 nm wavelength.

The standard shows smooth peak with the absorbance maxima at 265 nm. However, such smooth peak cannot be observed in the UCNPs assisted ergosterol conversion since other sterols are formed. In this context we have also furnished the ergosterol exposed to UV light for comparison. Because the ergosterol to vitamin D_2 shift is too narrow (260 to 265 nm) to quantify; the standard analytical technique for the vitamin D_2 *i.e.*, HPLC was performed, which matches the vitamin D_2 retention time peak (Fig 2.6). This confirms the occurrence of ergosterol to vitamin D_2.

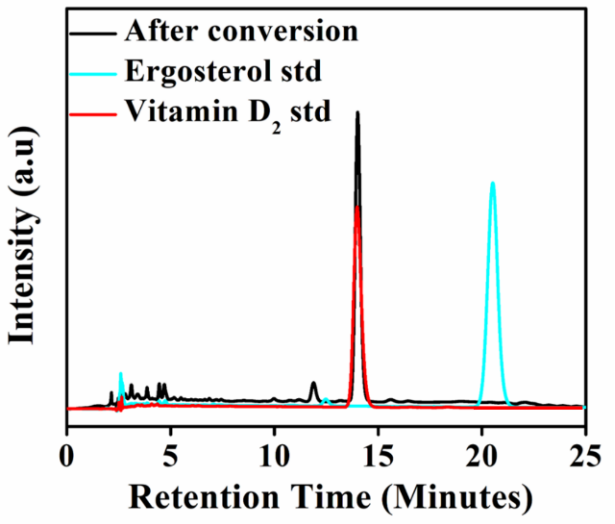

Fig 2.6 HPLC chromatogram of ergosterol, vitamin D_2 and ergosterol (irradiated with UV light for 2 hours).

2.3.2 Vitamin D_2 enrichment in mushroom:

To irradiate UV rays inside the mushroom tissue, the as-prepared UCNPs solution made up to 400 ppb (reason for 400 ppb concentration is the conversion efficiency vivid infra) with respect to yttrium ions was spin-coated onto the quartz coverslip substrate to develop a simple optical device.

Fig 2.7 Digital Picture of ivory colored upconversion quartz coverslips. The coverslips were inserted at equal distance in button mushrooms for its exposure in solar simulator and laser irradiation

The coating was performed on a quartz coverslip with a 10 mm diameter, which turned ivory color after coating. (Fig 2.7). The coated quartz cover slip was further analyzed with AFM, which shows typical spin coated surface morphology with coexistence of particles and few clusters. (Fig 2.8a left). The relation of coating morphology and conversion efficiency is explained vivid infra. The quartz coverslip of 10 mm diameter was found to be convenient to place in the inter-lamellar space of the most popular commercial mushroom species *i.e.*, *Agaricus bisporus* (Button mushroom) (Fig 2.8a right).

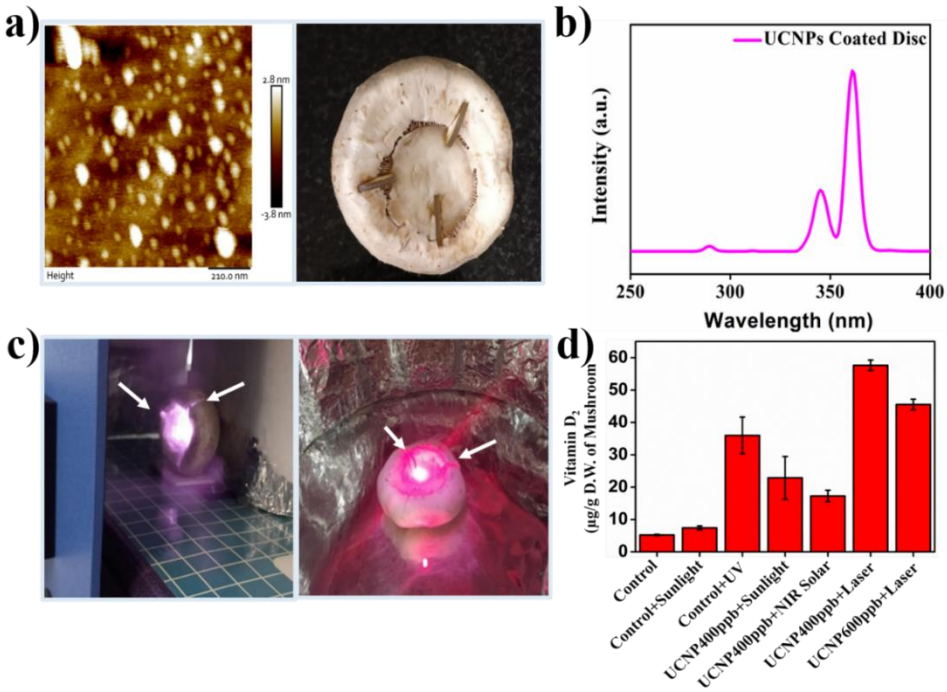

Fig 2.8 Vitamin D_2 conversion in mushroom (a) Left image shows AFM image of UCNPs $NaYF_4$ Yb^{3+}, Tm^{3+} coated quartz coverslip, Right image shows mushroom inserted with the UCNPs coated coverslips (b) Fluorescence spectra of disk coated UCNPs at 980 nm excitation wavelength (c) Left image shows mushroom irradiated using 980 nm excitation wavelength for 60 minutes, Right shows the mushroom inserted with UCNPs coated coverslips and illuminated using a solar simulator with NIR wavelength (900-1100nm) for 2 hours, Arrows indicate the position of UCNPs coated coverslip inserted into mushroom (d) Comparison of vitamin D_2 content (µg g^{-1} Dry weight of mushrooms) in different treatments (control, control + solar (sunlight), UV (without UCNPs), UCNPs coated coverslip(400 ppb) inserted into the mushroom and irradiated using the solar simulator for 2 hours using only NIR range from (900-1100 nm) and UCNPs coated coverslips inserted into the mushroom and irradiated using laser for 60 minutes at 400 ppb and 600 ppb concentration with respect to yttrium ions.

Subsequently, to quantify the UCNPs-assisted ergosterol to vitamin D_2 conversion in mushroom, three UCNPs devices were inserted into the mushroom at an equal angular distance (Fig 2.8a right panel). This setup of mushroom with the device was exposed to different radiation sources *viz.*, 980 nm laser (2 W), selective NIR illumination from the solar simulator and sun irradiation. Fig 2.8c left and right shows the photograph of the UCNPs device inserted into the mushroom illuminated using the 980 nm laser power (2 W) and selective NIR illumination from the solar simulator respectively. The photos show the difference in the degree of violet radiation emitted from different excitation sources having a different power. For the UCNPs disk-assisted vitamin D_2 enhancement in mushroom using 980 nm laser (2 W power) and selective NIR illumination from the solar simulator, the incubation time was optimized. The mushrooms irradiated under the laser for more than 20 minutes caused the sample to dehydrate, which may be due to the evaporation caused by the overlap of the absorbance of water with 980 nm. In the treatment using selective NIR illumination from the solar simulator, the duration was extended to 2 hours, because this has been the maximum duration of UV light incubation reported before (details in Table 1). The UV emission spectra from the UCNPs

device was quantified using the 980 nm excitation, which shows the emission pattern similar to the emission pattern recorded in the solvent (Fig 2.8b).

Furthermore, our experiments also show that the samples collected from the treatments irradiated using selective NIR from solar simulator for a lesser period of 30 and 60 minutes have a poor conversion. Thus 20 minutes for each disk (*i.e.*, one hour for mushroom exposure) and 2 hours incubation time was found optimum for the incubation under 980 nm laser and selective NIR illumination from the solar simulator respectively. For comparison, three different controls were maintained, 1. Control Mushroom without any exposure, 2. Mushroom exposed to sun radiation (having ~62,000 lux) for 2 hours, 3. Mushrooms exposed to UV radiation with 250 W mercury lamp at 10 cm distance for 2 hours.

The vitamin D_2 content in all of the treated samples was measured using HPLC and plotted in Fig 2.8d. Control mushrooms without any irradiation show ~5 µg vitamin D_2 g^{-1} dry weight and the mushrooms treated under sun radiation without UCNPs show ~7 µg vitamin D_2 g^{-1} dry weight. In the case of mushrooms exposed to UV irradiation, the vitamin D_2 content raised to ~35 µg g^{-1} dry weight. Interestingly the laser-assisted "mushroom + device (400 ppb)" treatment shows 58 µg vitamin D_2 g^{-1} dry weight of mushroom, to our knowledge this is the highest compared to the reports before (few of the reports tabled in Table 1). The use of disks having UCNPs coating with more than 400 ppb concentration *i.e.*, 600 ppb show no more increase in the ergosterol to vitamin D conversion, hence saturation has been reached at 400 ppb coating solution. To understand the relation of the UCNPs concentration with the conversion efficiency, the disks coated with different concentration of UCNPs, were observed with the AFM. With the increase in the concentration there was increase in the presence of independent particles up to 400 ppb concentration (Fig 2.10 and Table 2). In the disk coated with 400 ppb concentrated solution, ~446 individual particles 4 μm^{-2} was counted.

During treatment with the UCNPs device under selective NIR illumination from the solar simulator, the vitamin D_2 content raised to ~17 µg g^{-1} dry weight of mushroom, which is ~2.4 times more than the sun irradiation without UCNPs disk (kindly note that in our solar simulator UV radiation was kept off, whereas in the control mushroom illuminated with sun radiation includes UV). The treatment of mushrooms with the UCNPs disk under sun irradiation is found to have ~23 µg g^{-1} dry weight of mushroom. However, the vitamin D content in the mushroom irradiated with regular UV irradiation, needs external energy support. To quantify the contamination of the UCNPs, the concentration of yttrium in the treated samples were quantified with ICP-MS and found to be 36 ng g^{-1} dry weight of mushroom, which is very less to cause toxicity (vivid infra). The sunlight assisted conversion will be further enhanced in other species like *Pleurotus ostreatus* where the conversion is continuously proved to be more than *Agaricus bisporus*.[45] This could be a vital solution to overcome vitamin D deficiency in remote locations. Thus, the developed disk after coating was characterized using the XRD for the specific peaks (Fig 2.9).

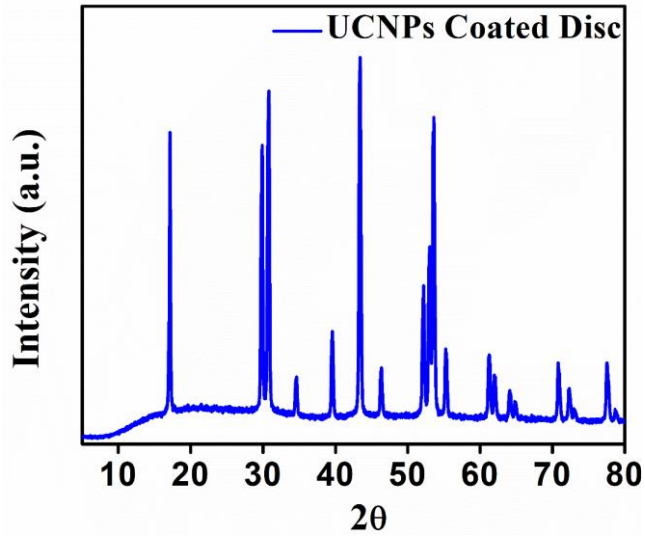

Fig 2.9 XRD spectrum recorded for the quartz coated $NaYF_4$ Yb^{3+}, Tm^{3+} cover slips.

Table 1 Description of Mushroom exposure to varying time in UV light conditions.

S. No.	Amount ($\mu g\ g^{-1}$ DW)	Exposure Source	Time (min)	Reference
1	7	UV-B	25	[27]
2	<15	UV-B	40	[16]
3	7	UV-C	120	[199]
4	15	UV-C	3.2	[166]
5	20	Commercial UV treated mushroom in US retail	-	[40]

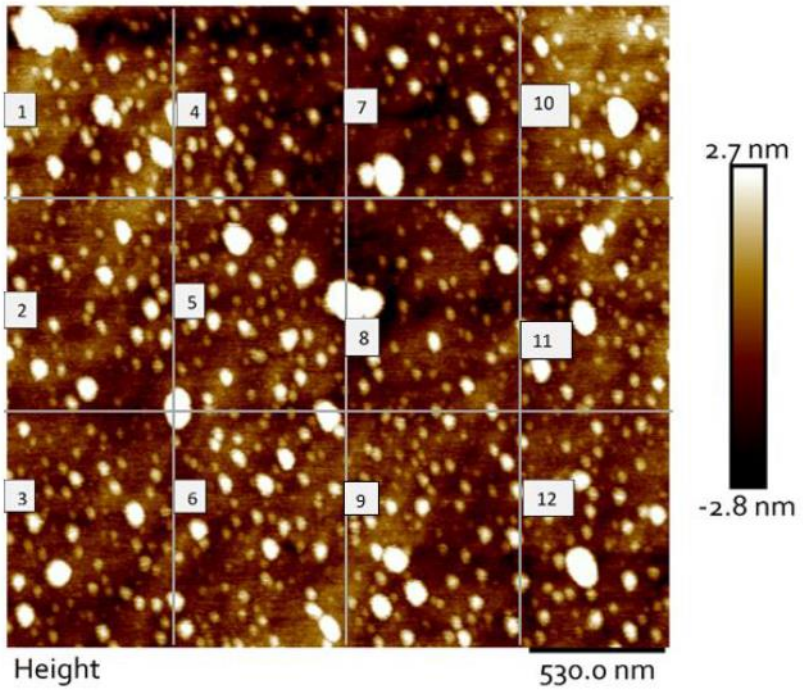

Fig 2.10 AFM image for the UCNPs coated disc at 400 ppb concentration with respect to Yttrium ions.

Table 2 Table showing summary of $NaYF_4$, Yb^{3+}, Tm^{3+} coated coverslips at 400 ppb concentration.

Square No.	No. of independent particles	No. of clusters	Standard deviation
1	37	8	2
2	35	14	3
3	40	8	2.5
4	55	11	1.6
Average	42	10	2.275

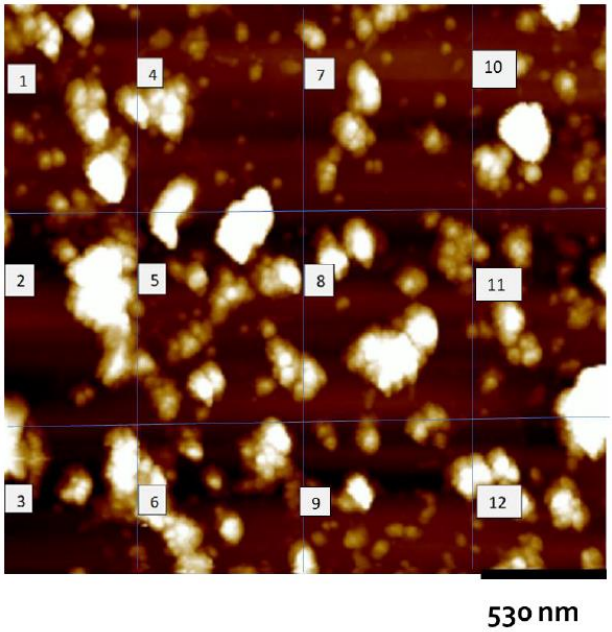

Fig 2.11 AFM image for the UCNPs coated disc at 600 ppb concentration with respect to Yttrium ions.

Beyond this concentration, the number of independent particles started to reduce in the disks due to overcrowding (Fig 2.11, Table 3). Thus, for all further treatments with irradiation experiment, disks coated with UCNPs solution made up to 400 ppb concentration with respect to yttrium ions was used.

Table 3 Table showing summary of $NaYF_4$, Yb^{3+}, Tm^{3+} coated coverslips at 600 ppb concentration.

Square No.	No. of independent particles	No. of clusters	Standard deviation
1	6	13	2.1
2	2	5	3.0
3	-	5	1.4
4	6	7	1.0
Average	3.5	8.5	1.87

2.3.3 Calculation of conversion efficiency: Thus, the conversion efficiencies of ergosterol to vitamin D_2 in the presence of UCNPs disk was examined by using 2 light sources, *viz*. 1. 980 nm laser and 2. Solar simulator having only the NIR (900-1100 nm) LEDs operated (switched on). The yields in these conditions were 58 µg g^{-1} (in 1hour exposure) and 17 µg g^{-1} (2 hours exposure) respectively.

In reference to the UCNPs-assisted sterol to vitamin D_2 conversion, we calculated the apparent quantum efficiency (AQE) using equation (1)

$$AQE = n\,(No.\,of\ electron\ or\ hole) \times \frac{Number\ of\ product\ molecule\ produced}{Number\ of\ incident\ photons} \times 100\ (\%) \quad \ldots\ldots\ldots\ (1)$$

The details of AQE calculation are detailed in supporting information. The AQE for the 980 nm laser as well as the laser assembly was estimated to be 0.00042 % and 0.00126 % respectively. The AQE under direct sunlight (full spectrum ranging from 300 to 2300 nm) is 0.000065 %. Thus, the AQE of ergosterol to vitamin D_2 was highest in the UCNPs + selective NIR from the solar simulator assisted conversion.

2.4 Conclusion

The UCNPs disk prepared by spin coating with optimum particles proved our hypothesis that with the UCNPs disk ergosterol in the mushroom can be converted to vitamin D_2 by solar irradiation. The application of UCNPs for vitamin D_2 enrichment in domestic as well as in the industry follows below;

2.4.1 Domestic application: Considering 25 g of mushroom/serving,[165] and ~15 µg vitamin D_2 g^{-1} of mushroom dry weight from the above method (UCNPs device facilitated solar irradiation assisted mushroom treatment), ~1/3 serving can fulfil the requirement of the day. Since, the widely accepted vitamin D_2 nutrition recommendation is 800-1000 international units, [200] which is equivalent to 20-25 µg and the dry matter of the *Agaricus bisporus* mushroom biomass contributes to ~7-10 %.[28,40] The possible UCNPs contamination through this method in a serving will be 70-80 ng (~70-80 ng 2.5 g^{-1} of dry mushroom weight). This is too less to cause any toxicity as UCNPs tested for oral administration at 10 mg dose/Kunming mice has shown no toxicity and the biodistribution study also shows the particle clearance through fecal and renal route within couple of days.[55]

2.4.2 Industry application: The UCNPs device facilitated laser-assisted mushroom treatment shows unprecedented conversion efficiency, in comparison to the conventional UV light irradiation method. This highlights the UCNPs aided deep lamella penetration to play an important role. The ergosterol content in the mushrooms ranges from 7 to 10 mg g^{-1} dry weight,[166] therefore more efficient UCNPs could benefit industrial-scale vitamin D_2 processing. Because vitamin D_2 is the most acceptable form of vitamin D fortification.

Chapter 3

Food sensing

Phone camera nano-biosensor using mighty transparent sensitive reusable upconversion paper

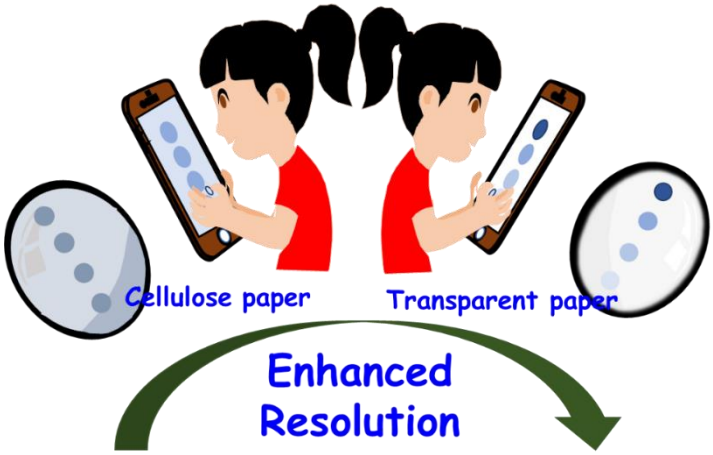

TOC. Schematic representation of lycopene detection using smartphone camera with enhanced detection in paper.

Abstract

Lycopene, a natural colorants and antioxidant with a huge growing market is highly susceptible to photo/thermal degradation, which demands real-time sensors. Hence, here a transparent UCNPs strip, having Yb^{3+} 30 mol % Tm^{3+}, 0.1 mol % β-$NaYF_4$ UCNPs which shows intense 475 nm emission, has been developed. This strip has been found sensitive to lycopene, down to 10 nM using a smartphone camera, which is due to static quenching confirmed by lifetime study. In comparison to previous paper strips, here the transparent strip has minimal scattering with maximum sensitivity in spite of not using any metal quenchers. An increase in strip hydrophobicity during the fabrication process complements the strip to selectively permeate and present an extraction-free substitute analysis to chromatography. Hydrophobicity also adds the capability to reuse the strip with ~100 % luminescence recovery.

KEYWORDS: UCNPs, sensing, lycopene, tomato, CNC film

3.1 Introduction

Lycopene the natural colorant and antioxidant is becoming an important constituent in the food and beverage, nutraceutical, pharmaceutical and cosmetics industries. Its market was 66 million $ in 2010, which raised to 107 million $ in 2020 and is expected to reach 200 million $ in 2030. [201,202] It's an expensive natural compound extracted predominantly from tomatoes, and the cost can go above 6000 $ kg^{-1}. Lycopene has been found to reduce the risk of cardiac diseases, cancers, organ disorder, metabolic syndrome and infertility, [203,204] which emphasises its role as a nutraceutical in human health. [7,205–207] Importantly, the poorest consumer group has been found to be the population most in need of lycopene supplement [208] and supplement in different forms like juice, soup and sauce has shown the plasma lycopene content to increase by ~ 60 % (up to 1.15 µM L^{-1})[209] Latest regulation on the food industries emphasis the labelling of the ingredient to differentiate the natural from the artificial ingredients. [210] The concentration of lycopene in turn controls the flavour as it is the precursor for the high odour unit value compound 6-Methyl-5-hepten-2-one. [211] Lycopene is susceptible to light, temperature and microbial degradation, which warrants as high throughput sensing at various stages like raw material purchase to processing to supply chain, etc., Lycopene is acyclic with 5, 9, 13, and 15 position isomers having 3 absorbance maxima between 400 to 510 nm, which draw special attention for having the highest reactive oxygen removal rate among all carotenoids (K_q : 31 x 10^9 M^{-1} S^{-1}). [212,213]

The cutting edge technology to control the optical properties in nanoparticles, let to the development of optical sensors for metal ions and organic molecules quantification. [214,215,216] Such detection is based on fluorescence and absorbance energy transfer, static/dynamic quenching mechanism and FRET/inner filter effect. [217] Other mechanisms like the electron teleportation electron/hole, aggregation induced quenching/emission and chroma response has been explored for the fluorescence change and calorimetric detection. [19-22] Recent development

in florescence assisted detection uses machine learning to analyse the curve pattern and identify the nucleotide. [23] The ubiquitous access to smartphones gives the convenience of sensors integration like the piezo etc., for on-the-spot analysis. [24] Similarly using the smartphone camera sensors has been developed for as the quantification of metal, glucose, antibiotic, covid virus, etc.,[25-30] On the other hand in the search for more versatile, low cost and reusability of sensors paper-based platform are encouraged. [31] Similarly the fabric-based calorimetric signals are evolving as the user-friendly technique. [32] Very recently excellent sensor paper for thiram detection down to 60 nM concentration in the fruits and vegetable has been conceived, using fluorescent carbon quantum-dots having intense blue emission. [33]

Among fluorescent nanoparticles, the near infrared (NIR) sensitive materials have gained the most attention as they are free from background interference. [34,35] In the plant metabolite quantification, the samples rich in chromophores often show background fluorescence in visible light excitation. [36,37] Hence the intense fluorescent upconversion nano-biosensor paper with NIR excitation could be a possible solution with smartphone camera assisted documentation as it's comparatively limited to few demonstrations like drug counterfeiting, quantification of pesticide in fruits and other samples. [38,39,40]

In this study, we developed an upconversion sensor paper of high transparency to detect lycopene levels with high precision by using the overlap of lycopene absorbance with the UCNPs emission coupled with a smartphone camera assisted quantification. To our knowledge, for the first time, here an upconversion sensor paper of high transparency through low scattering has been developed in contrast to regular scattering cellulose papers. The transparent paper has been optimised by us before for other packing applications. [41] Also, the increase in the hydrophobicity during cellulose nanocrystal (CNC) modification and UCNPs addition paves the way for efficient lycopene mobility and quenching. Further this also gives accessibility to the solvent to wash all the lycopene pockets after use to restore ~100 %

emission, which is again not demonstrated before. As agricultural products are highly perishable and the level of antioxidants are fluctuating at the fruit maturation stage; hence these kinds of real-time sample analysis are needed to speed up the detection and reduce the dependence on lengthy and costly chromatographic analysis in food quality control processes.

3.2 Material and Methods:

The chemicals and materials used in this study were:- Octadecene, Oleic acid (Sigma Aldrich), Yttrium acetate (Sigma Aldrich), Ytterbium acetate (Sigma Aldrich), Thulium acetate (Sigma Aldrich), Acetone, Methanol (HPLC grade), Water (HPLC grade), Hexane (Merck), 2,6- Di Tert-butyl 4 methyl phenol(Sigma Aldrich), Methyl tert-butyl ether (Sigma HPLC grade), Lycopene (Sigma Aldrich), Poly vinyl alcohol (MW-89,000-98,000), Cellulose nanocrystals (provided by Forest Products Lab Batch 2018-FPL-CNC-130, 10.0 wt% in water, 1.06 wt% sulfur on dry CNC, sodium form), C30 column (YMC), Ascorbic acid (Sigma Aldrich), Glucose (Hi-media).

3.2.1 Characterization: Powder XRD analysis was carried out in a Bruker advance D8 diffractometer that has Cu kα radiation source (λ=1.5406) at 40 KV and 50 mA. The transmission and HR-TEM were performed using JEOL-JEM 2100 that has lanthanum hexaboride filament at an accelerating voltage of 200 KV. The photoluminescence spectra were measured using Fluoromax-4 spectrofluorometer (Horiba) equipped with 980 nm laser excitation. Contact angle was measured using Kruss advance drop shape analyser. HPLC was performed in Waters instrument having MTBE and 95 % methanol as the mobile phase and stationary phase as C30 (YMC 250 X 4.6 mm I.D) column in a gradient flow. Ellipsometer studies were performed on Angstrom Sun Technologies Inc. TF Probe for film thickness and wavelength at 633 nm.

3.2.2 Synthesis of β-$NaYF_4$, Yb^{3+} 30 mol %, Tm^{3+} 0.1 mol % upconversion nanoparticles

The synthesis has been followed with the aim to get the maximum emission intensity at the wavelength, where lycopene absorbance is maximum. For this the precursor ratio of the activator and emitter were changed while following the rest of the steps as reported before.[186] Briefly in a 50 mL three-neck flask $Y(CH_3COO)_2$, $Yb(CH_3COO_2)$, $Tm(CH_3COO_2)$ were added so that 2.8 mM, 1.2 mM and 0.02 mM precursor concentrations, respectively, had been prepared in 7:3 ratio of octadecene and oleic acid. The temperature of this mixture was raised to 120 °C in a vacuum and kept in continuous stirring for 30 min. The reaction temperature was reduced to ~50 °C, followed by the addition of 16 mM NH_4F and 10 mM NaOH solution prepared in methanol. Once the solution turned turbid it was allowed to stir for 30 min. The methanol was then removed from the reaction using vacuum at 90 °C. Finally, the temperature was further raised to 300 °C with constant stirring for 1.5 hours. After cooling, the UCNPs were precipitated by the addition of 40 mL acetone to the resultant solution followed by centrifugation at 7000 rpm for 10 min. The resultant pellet has been washed using hexane/ethanol mixture for a minimum of three times and the resultant pellet is then redispersed in hexane and stored for further use.

3.2.3 Upconversion luminescence quenching in solution with lycopene addition

Using fixed concentrations of upconversion nanoparticles (0.5 mg mL^{-1}) the quenching efficiency of the luminescence was measured with increasing lycopene concentrations ranging from 2 µM-80 pM. Here the maximum titration volume was 10 µL, which does not have luminescence attenuation. A 980 nm laser was used as the excitation source.

3.2.4 Interference study: Fruits commonly contain ethanol, ascorbic acid, glucose, naringenin, magnesium, sodium, calcium, potassium, quinolone yellow and chlorogenic acid; hence these molecules were considered as the model compounds for an interference study of UCNPs quenching. These molecules were added into the UCNPs solution, in a similar volume in order to arrive at a final molar concentration equal to the lycopene, and the emission spectra were measured using 980 nm excitation.

3.2.5 Fluorescence quenching in real sample analysis: In the case of real sample analysis, different concentrations of tomato juice were added into optimum concentration UCNPs (0.5 mg mL^{-1}) and centrifuged at 9000 rpm for 10 min. Supernatant was discarded and the remaining pellet was resuspended in same volume of hexane and the emission spectra were measured at 980 nm excitation wavelength.

3.2.6 Time resolved decay measurements: Lifetime decay measurements of UCNPs were measured both in the presence and absence of lycopene using laser excitation of 980 nm and emission at 475 nm. The curves were fitted to single exponentials and the average lifetime was calculated.

3.2.7 Sensor paper strip fabrication: The CNC/PVA paper strip was fabricated using our previous protocol optimised to maximum transparency. [42] Briefly 11.9 g PVA powder was added to 88 mL of water and stirred at 85 °C. This PVA solution was mixed with CNC at 0.3: 0.7 ratio. This mixture was sonicated and stirred for another 2 h, following which it was casted onto glass slides. Approximately 1.5 mL of the above CNC: PVA aliquot was shear-casted at an angle of 45° using a single edge razor blade. The shear-casting was repeated for approximately 3-4 times on the glass slide and the slide was incubated in a desiccator for 4-6

days. After this time, the paper strips were peeled off from the glass slide and stored in a controlled atmosphere at room temperature for further use. A similar protocol was followed for UCNPs casted paper strip fabrication by adding 2 mg mL^{-1} of UCNPs in CNC: PVA suspension.

3.2.8 Lycopene content validation in real sample using HPLC: Lycopene was extracted and analysed using the HPLC. Briefly, tomato juice was dehydrated using 65 mL of methanol and followed by filtration through a glass Buchner funnel. [44] The filtrate was mixed with a mixture of carbon tetrachloride and methanol in a separating funnel to extract the lycopene to the organic phase and repeated for three times. Then, a few drops of hot methanol and benzene were added to the resultant before solvent evaporation and redispersed into hexane for further analysis.

HPLC analysis was carried out using MTBE: 95% methanol as the mobile phase and C30 as stationary column using a PDA detector having 400-530 nm as detection wavelength. Lycopene standards were injected for the calibration plot.

3.2.9 Contact angle measurement: Contact angle was measured on the dried paper strip using a drop shape analyser (Kruss advance drop shape) equipped with high-resolution CCD camera. A small rectangular sensor paper strip was placed on the sample holder and drop was placed onto the surface of the sensor paper strip and contact angle was measured.

3.2.10 Image analysis: A simple in-house system was fabricated to house the laser and sensor paper strip at different compatible positions for smartphone camera assisted imaging. The fabricated sensor paper strips were peeled off from the substrate after drying and cut into

0.5 cm x 0.5 cm pieces. The laser was shined at an angle of 45 ° with respect to the paper strip position, and NIR filter was placed in front of the camera which was vertically above the sensor paper strip. Different dilutions of lycopene were added on the fabricated sensor paper strip and images were captured using One plus 8T smartphone camera. Further images were analysed using image J software and the respective blue intensity was measured at the desired area.

3.2.11 Real sample analysis using sensor paper strip: Real sample analysis was performed on sensor paper strips by diluting tomato fruit juice 10 times and adding 10 µL of diluted juice onto the sensor paper strip. Following this, the strips were air-dried and imaged using the smartphone camera for image analysis.

3.3 Result and discussion

This study aimed to develop an upconversion sensor paper to quantify the lycopene present in fruits and vegetables. The lycopene has absorbance maxima at 475 nm (Fig 3.1A), hence, to detect this, matching UCNPs with the emission maxima in the same range has been synthesized and characterized with minor modification. From the literature, it was clear that this emission arises from a band corresponding to $^{1}G_{4} \rightarrow {}^{3}H_{6}$ transition form Tm^{3+} activator in the $NaYF_4$ host having Yb^{3+} as the sensitizer. Further, the ratio of Yb^{3+} and Tm^{3+} has to be optimum to avoid cross relaxation and non-radiative loss which may compromise the desired maximum of 475 nm emission. [45-47] Therefore, UCNPs with different Yb^{3+} and Tm^{3+} ratios were synthesized with Yb^{3+} at 30 % and varying Tm^{3+} ion concentrations by thermal decomposition method reported by us before for the vitamin D fortification in mushroom. [48]

The synthesized UCNPs were characterized using XRD and emission spectrophotometry at 980 nm excitation.The XRD pattern confirms the presence of hexagonal β-$NaYF_4$ phase material by matching to JCPDS standard card 16-0334 (Fig 3.1B). In case of

emission spectra, the UCNPs with 0.1 % of the Tm^{3+} expressed 475 nm emission maxima 9 times more than the 650 nm emission (Fig 3.1C); The photograph of the UCNPs illuminated by the 980 nm NIR laser at 2 W is given in Fig 3.1C inset contrary to our previous study that shows 475 nm emission ~2 times the 650 nm emission while having 30 % Yb^{3+} with 0.5 % Tm^{3+} ratio. Thus, this material with the maximum emission at 475 nm qualifies for the high sensitivity by maximum quenching at minimum lycopene concentration. The TEM image of the sample with the selected emission spectra shows the average particle size to be 25 nm (Fig 3.1D). The HRTEM image of the particles shows the "*d*" spacing between the lattice to be 0.52 nm (Fig 3.1D inset), which corresponds to the <100> hexagonal phase of $NaYF_4$ host nanocrystals.

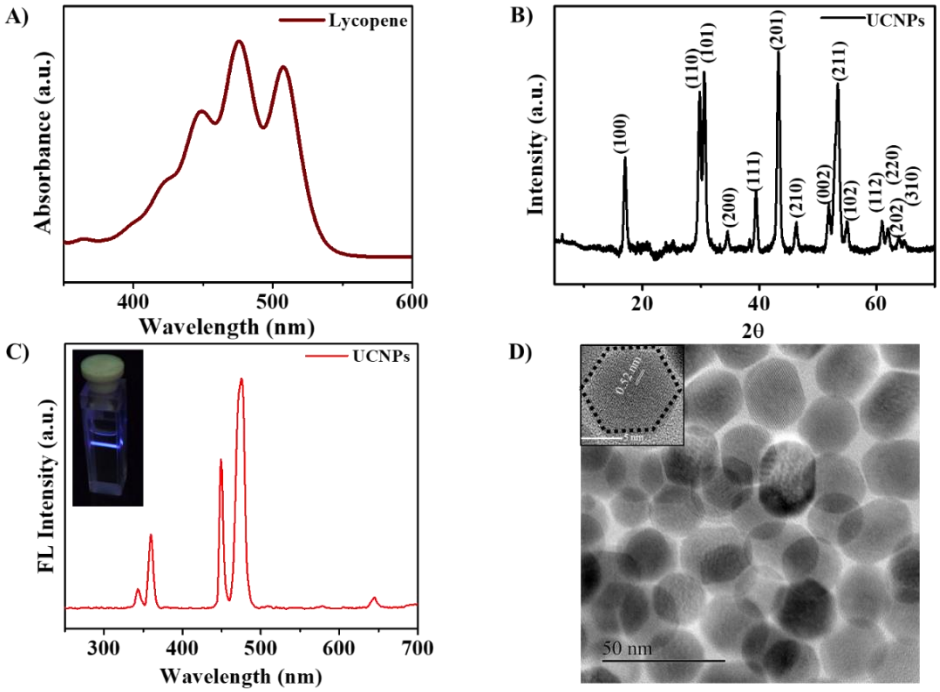

Fig 3.1 Characterization of lycopene and UCNPs A) UV-VIS absorbance spectra of lycopene B) XRD pattern of as prepared $NaYF_4$, Yb^{3+}, Tm^{3+} UCNPs matching with JCPDS 16-0334 C) Photoluminescence spectra of as prepared UCNPs and inset showing photograph of as prepared UCNPs when irradiated using 980 nm excitation laser. D) TEM and HRTEM of UCNPs showing lattice d spacing of 0.52 nm.

3.3.1 Spectroscopic analysis

Before the sensor paper fabrication, the suitability of the nanoparticles to show luminescence quenching through energy transfer (ET) by the overlap of the UCNPs emission with the lycopene absorbance has been examined. Different UCNPs concentrations were titrated with 10 µM of lycopene and found 0.5 mg mL^{-1} of the UNCPs were suitable to show measurable quenching efficiency. Following this for the fluorescence stability and maximum quenching signal of the UCNPs in response to lycopene concentrations were performed in different solvents like hexane, THF, toluene, benzene, diethyl ether and chloroform. Here the benzene, ether and chloroform showed aggregation, hence the fluorescence signals were poor, whereas in THF and toluene the quenching is not proportional (Fig 3.2, Fig 3.3).

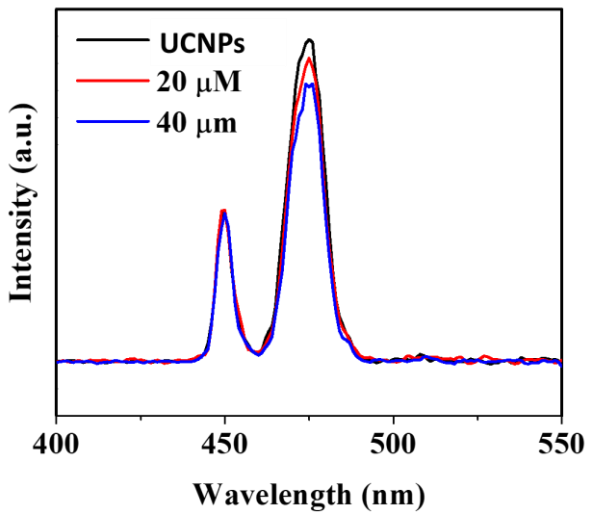

Fig 3.2 Fluorescence emission spectra of UCNPs in THF in response to increasing lycopene concentrations (20 µM and 40 µM) in hexane measured at 980 nm excitation.

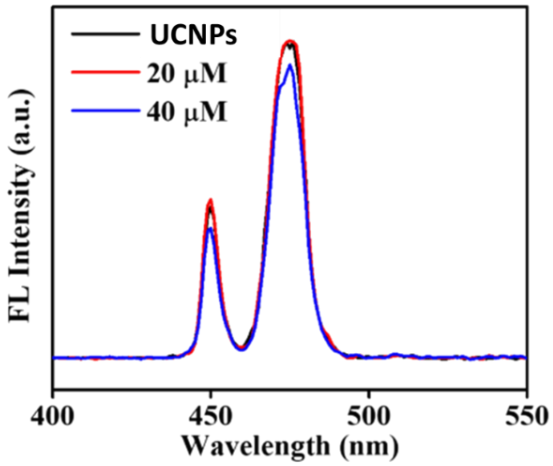

Fig 3.3 Fluorescence emission spectra of UCNPs dispersed in toluene in response to increasing lycopene concentrations (20 µM and 40 µM in hexane measured using 980 nm excitation laser.

In hexane, lycopene concentration dependent quenching of 450 and 475 nm UCNPs emission peak with a detection limit of 80 pM lycopene to 120 nM using 0.5 mg mL^{-1} UCNPs was observed (Fig 3.4). This optimisation of UCNPs concentration allowed to reach detection limit of 80 pM.

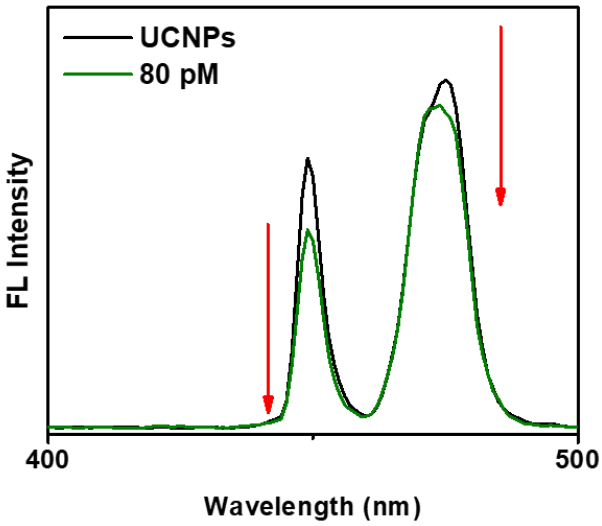

Fig 3.4 Fluorescence emission spectra of UCNPs in hexane at 80 pM lycopene concentrations upon excitation using a 980 nm laser.

The same amount of blank solvent was titrated in 0.5 mg mL^{-1} of UCNPs to ensure the absence of quenching by the solvent. (Fig 3.5)

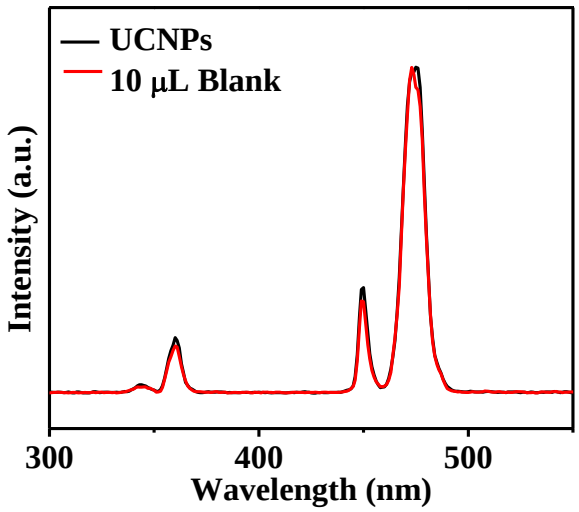

Fig 3.5 Effect of blank solvent (i.e., hexane) on the fluorescence emission spectra of UCNPs is illustrated with an excitation wavelength of 980 nm.

Here, the UCNPs did not show any measurable quenching with the addition of control solvent without lycopene, which confirms that the quenching is due to the analyte addition.

Quenching efficiency was calculated with respect to each analyte according to the equation

$Q.E\ (\%) = (I_0 - I)/I_0$

Where I_0 is the fluorescence intensity before and I is the fluorescence intensity after the addition of the analyte.

Ultimately, the aim of the study is to use this sensor design for real sample analyses, specifically for fruit quality determination, which have the major constituents like ethanol, ascorbic acid, glucose, naringenin, magnesium, sodium, calcium, potassium, and chlorogenic acid. So, to ensure the selectivity of 450 and 475 nm peak quenching to lycopene, the effect of the above compounds that belong to sugar, alcohol, vitamin, polyphenols and ions along with artificial food colourant quinolone yellow was investigated at μM concentration and found to have no interference (Fig 3.6-3.10).

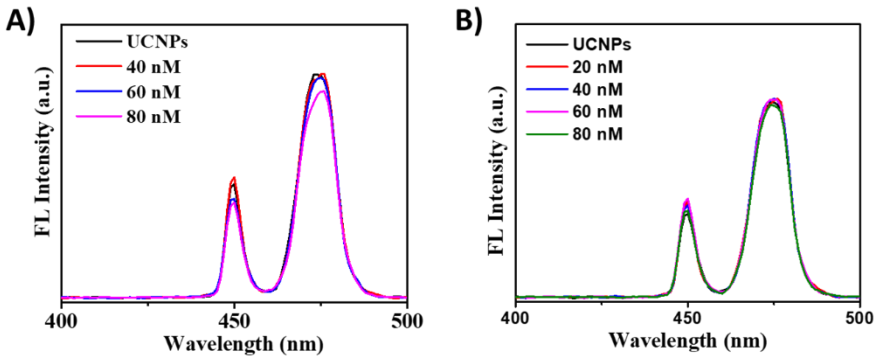

Fig 3.6 Fluorescence spectra of UCNPs in response to 40 nM to 80 nM glucose (A) and ascorbic acid concentrations (B) concentrations measured using 980 nm excitation wavelength.

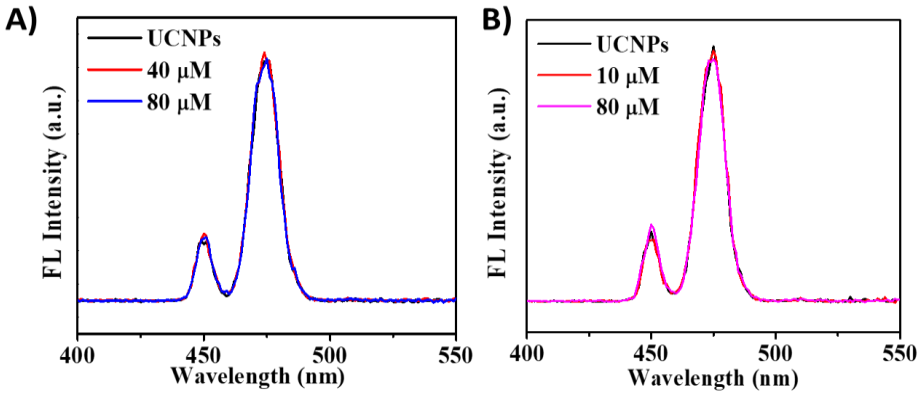

Fig 3.7 Fluorescence spectra of UCNPs in response to magnesium and potassium concentrations. The fluorescence spectra were measured using micromolar concentrations of magnesium and potassium to understand their role in interference.

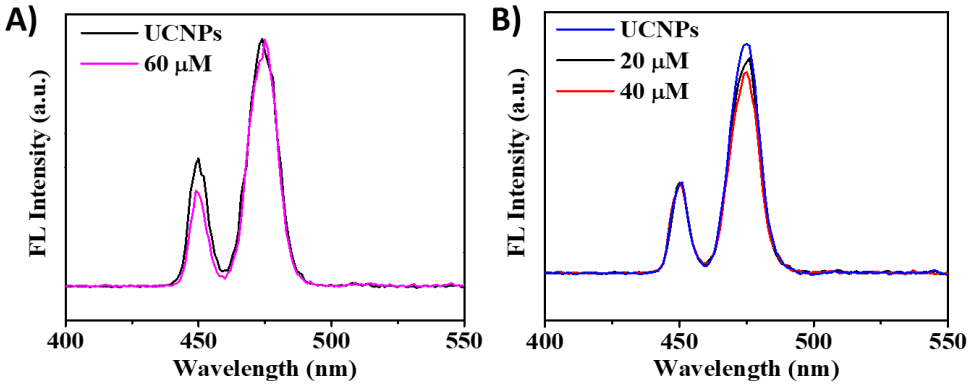

Fig 3.8 Fluorescence spectra of UCNPs in response to micromolar concentrations of sodium and calcium. The samples were excited using 980 nm wavelength.

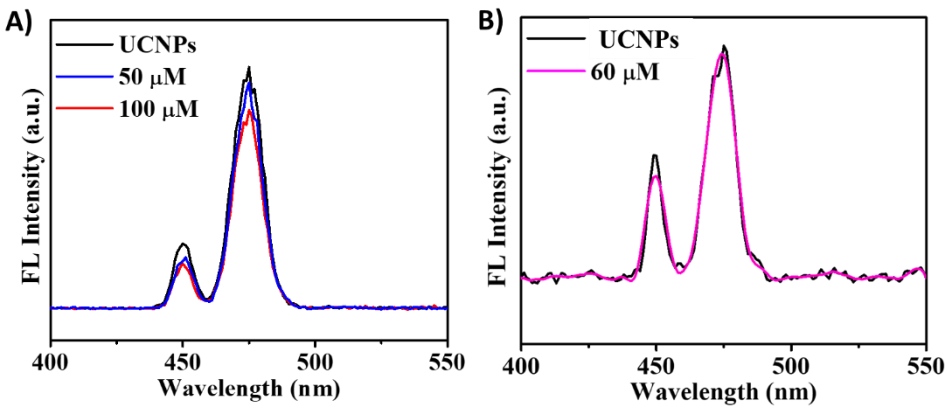

Fig 3.9 Fluorescence spectra of UCNPs in response to quinoline yellow (A) and naringenin (B) measured at micromolar concentrations. The samples were excited using 980 nm wavelength.

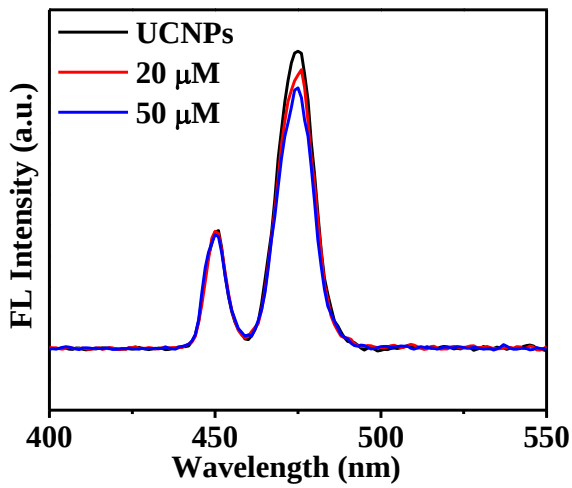

Fig 3.10 Fluorescence spectra of UCNPs in response to increasing chlorogenic acid concentration. The spectra were recorded using 20-50 μM concentrations of chlorogenic acid.

After this confirmation, real sample analysis was pursued using tomato juice, which is rich in lycopene. Fig 3.11D shows that with the increase in the real sample concentration there is a proportional decrease in the 450 and 475 nm emission intensity of UCNPs, which has not been observed in the control addition. The proportional reduction in the 350 nm peak may be due to the minor absorbance in the lycopene.

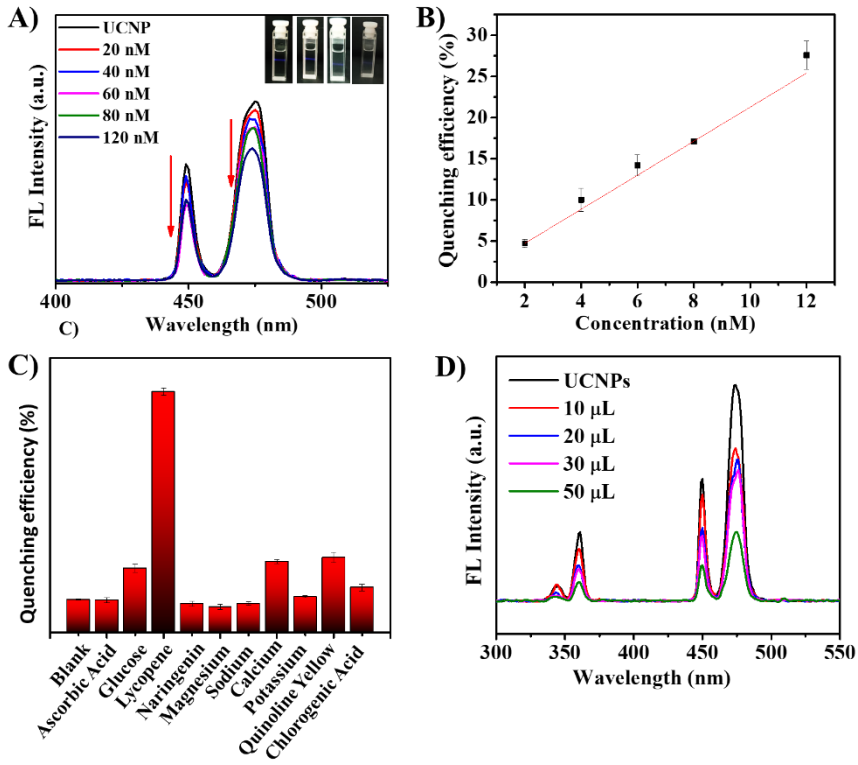

Fig 3.11 A) Fluorescence quenching of UCNPs with increasing lycopene concentrations (nM) inset shows the corresponding fluorescence photo. B) Linear calibration plot showing fluorescence quenching efficiency (%) at different lycopene concentrations (nM). C) Quenching efficiency with other possible interfering molecules in fruit juice shows the selectivity of the material to lycopene. D) Real sample analysis showing the increase in gradual fluorescence quenching in proportion to the increase in the fruit juice concentration.

3.3.2 Transparent UCNPs sensor paper strip preparation and characterization.

With the above encouraging results that shows the UCNPs to be sensitive and selective to ~pM concentration of lycopene, a transparent UNCP sensor paper strip was optimised with the aim of highest sensitivity. To fabricate such a sensor, a 98% transparent paper optimised by us using cellulose nanocrystals (CNC) and PVA (due to the matching refractive index) [218] was tested with different amount of UCNPs. The luminescence image of the fabricated UCNPs paper was captured using a smartphone placed in such a way that the camera fits the window of an inhouse custom designed accessory (Fig 3.12A). This accessory holds a 980 nm portable

laser at an angle of 45° with respect to the sensor paper with convenient distance along with the band pass filter placed in front of the smartphone camera. The CNC + PVA composite with 2 mg mL^{-1} amount of the UCNPs was found suitable for maximum transparency and optimum luminescence at 450 mW of laser power (Fig 3.12B). To ensure that the composite is having the same elasticity as that of our previous CNC + PVA mixture,[42] the loss and storage modulus has been measured. This shows almost same elasticity with an insignificant improvement, which may be due role of UCNPs as reinforcement agent. Since higher concentration of UCNPs cause intense emission that become insensitive to low analyte concentration, whereas lower concentration does not cause detectable emission. Therefore, the UCNPs concentration was optimised to 2 mg mL^{-1}, so that it has readability down to 10 µM lycopene quenching in the smartphone camera.

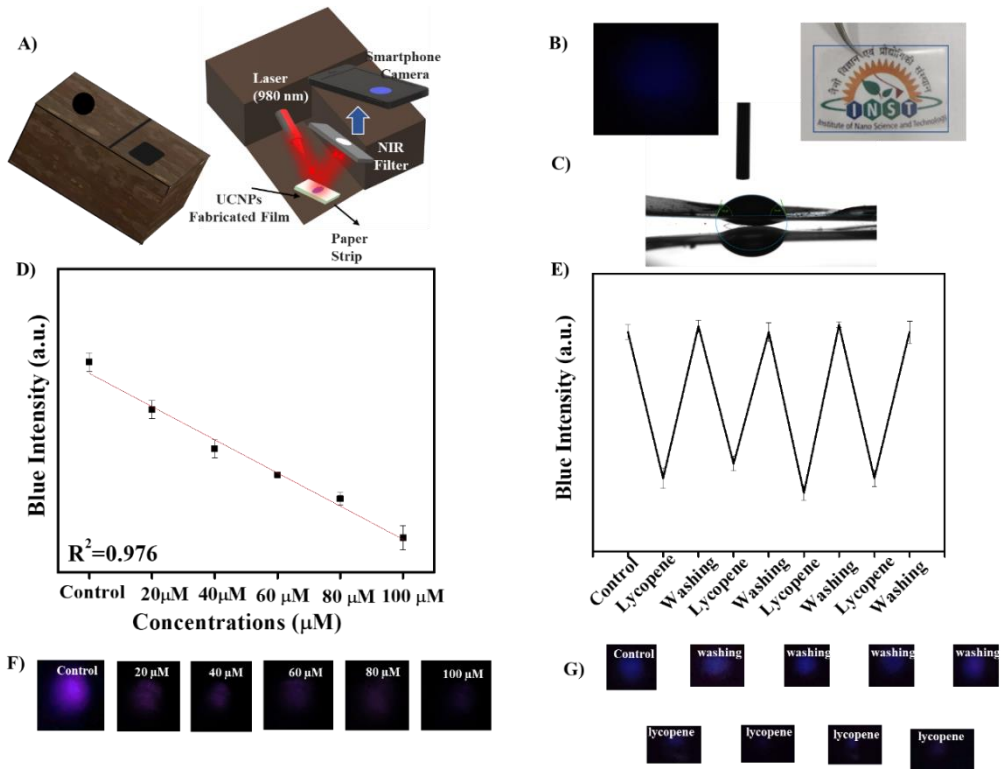

Fig 3.12 Image of in house custom designed accessory with characterization of transparent paper A) Image of in-house custom designed accessory with the cross-sectionals view for

smartphone/laser housing. B) Luminescence image of as-prepared UCNPs sensor paper strip under 980 nm laser excitation captured using smartphone camera. (Left) Photograph of the as-prepared UCNPs embedded transparent sensor paper strip showing the transparency of the strip on the institute emblem (right). C) Contact angle measurement of the UCNPs embedded sensor paper strip. D) Luminescence image of UCNPs sensor paper strip with the addition of increasing lycopene concentrations (Red line depicts the linear fit of the sensor paper strip to the increasing lycopene concentration). E) Reusability of the UCNPs sensor paper strip shown with the luminescence image restoration with each washing (corresponding normalised blue intensity is plotted). Digital images of UCNPs sensor strip F) with increasing lycopene concentrations (20µM-100µM) G) Reusability of the UCNPs sensor strip after successive washing steps.

The prepared sensor strip is desired to have a hydrophobic surface to have high lycopene mobility, therefore the water contact angle of the strip was measured. The contact angle measurement shows the sensor paper had the contact angle raised to 80° (Fig 3.12 C) from 40° in the UCNPs free transparent paper (40° can be referred from our previous publication, which is also a significant raise compared to regular cellulose paper). This raise may be due to complementary effect from the oleic acid coating on the as prepared UNCP, which is desired to enhance the interaction with lycopene as it is highly hydrophobic.

3.3.3 Quantification of the sensitivity.

The UCNPs sensor paper strip in Fig 3.12D shows the luminescence quenching sensitive to a proportional increase in the lycopene concentration while a shining 980 nm portable laser at 450 mW. The numerical count of the blue channel was measured using ImageJ software. Following this, to check the suitability of the UCNPs sensor strip to reuse multiple times, the sensor strip quenched with maximum amount of lycopene *i.e.*, 100 µM was washed with

hexane and tested if the blue channel count was restored at every washing. In this experiment for five repetitions the sensor strip was shown to restore the luminescent to the original value each time (Fig 3.12E). The transparent paper was found compatible, since it is comparatively hydrophobic, thus allows the hexane to reach all the micropores to wash away the hydrophobic lycopene. To check the stability of the strip, the thickness of the strip has been measured using ellipsometer, which shows the thickness to be stable ~1700 nm (Fig 3.13).

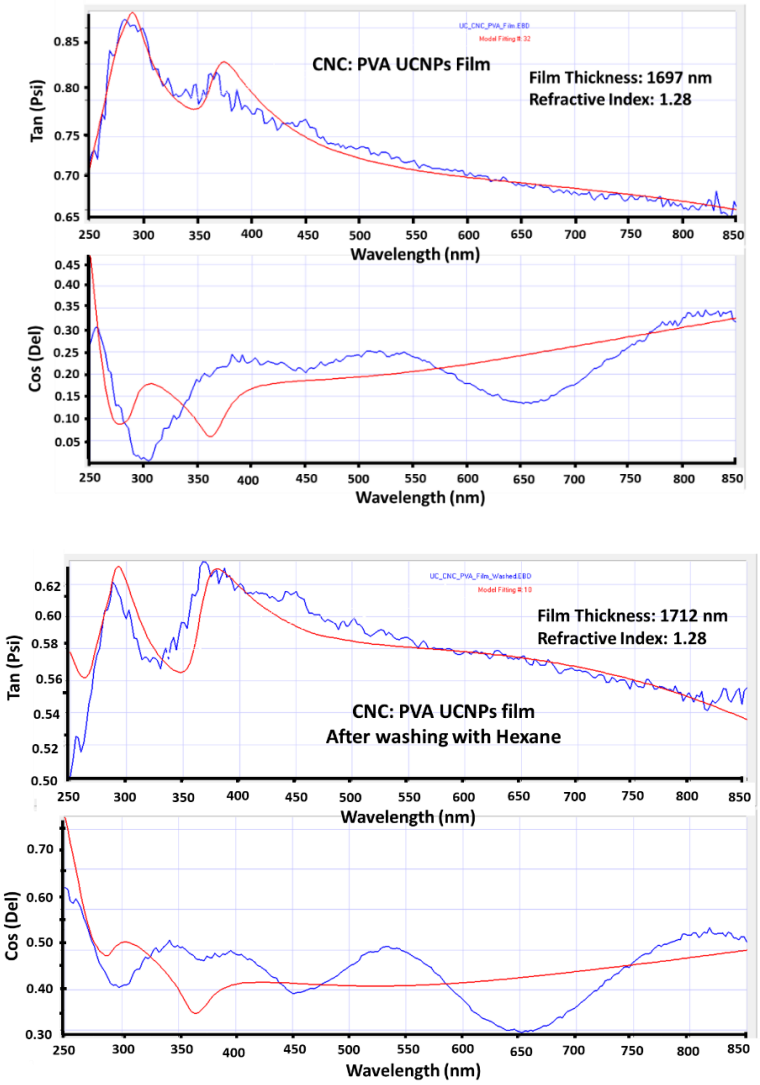

Fig 3.13 Comparison of CNC: PVA film thickness and refractive index before and after washing with hexane measured using ellipsometer

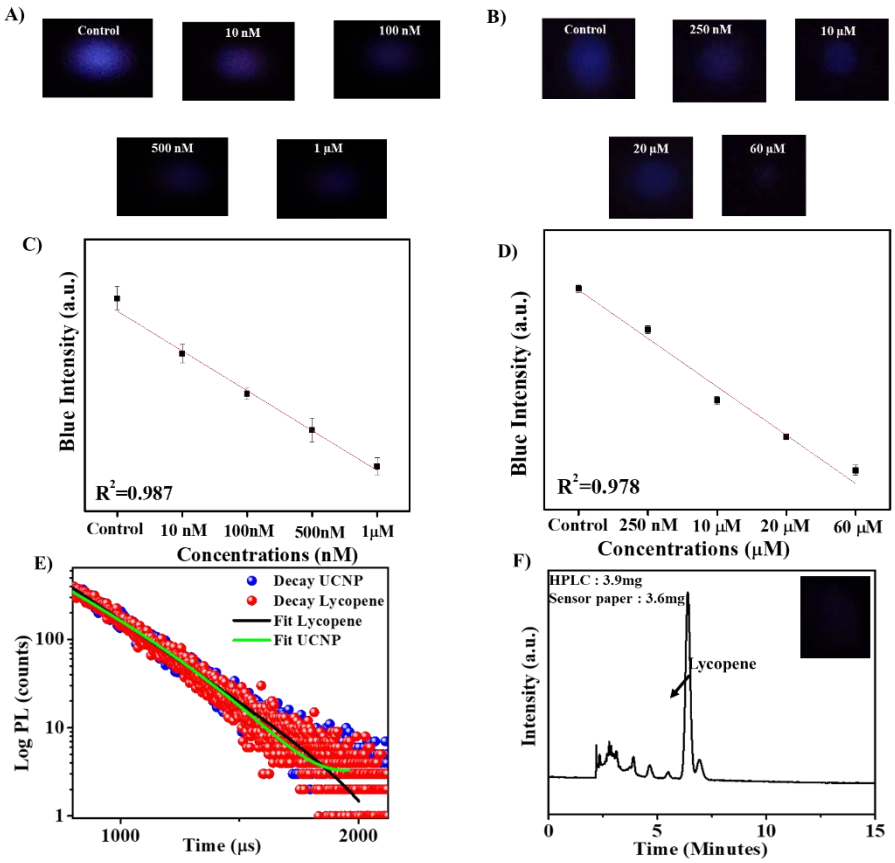

Fig 3.14 Digital pictures of the A) transparent paper strip B) cellulose paper strips demonstrating the change in the luminescence at varying lycopene concentrations. C) Limit of detection optimisation of transparent UCNPs sensor paper strip showing linear plot of quenching efficiency down to 10 nM lycopene. D) Limit of detection optimisation of UCNPs sensor paper strip prepared in regular cellulose paper. E) Lifetime analysis of UCNPs fluorescence decay in the presence and absence of lycopene with its corresponding fit. F) Representative HPLC chromatogram of extracted lycopene in C30 column and inset showing real sample analysis on transparent strip

Further, to compare the limit of detection of the transparent strip with that of the regular cellulose filter paper, which is commonly used before, an equal amount of optimum concentration of UCNPs were dropped on both materials and tested against lycopene. The strips were titrated with a reducing nM concentration of lycopene, showed the limit of detection of the transparent sensor strip to be 10 nM, (Fig 3.14C) whereas the regular cellulose filter paper with the UCNPs casting shows the detection limit to be 250 nM (Fig 3.14D). This

improvement in detection may be due to lower scattering in the transparent paper that allows the maximum blue channel count to reach the camera, whereas in the regular paper the quenching limit of the trace is undetected due to scattering. Thus, in the regular paper to improve the limit of detection, metal or strong organic dye with high absorbance index is needed.

3.3.4 Sensing mechanism behind the limit of detection

To understand the mechanism behind quenching the UCNPs fluorescence lifetime was measured. In fluorescence lifetime measurement, *τavg1* is the UCNPs lifetime *i.e.*, ~0.23 ms and the *τavg2* in the UCNPs lifetime after lycopene addition *i.e.*, ~0.238 ms (Fig 3.14E). There is no significant change in the lifetime, and hence the *τavg1/ τavg2* is nearly 1, which confirms that the ET is static rather than dynamic. [49,50] This means there is spectral overlap between the UCNPs emission and lycopene absorbance range and fluorescence quenching is due to an inner filter effect. This is a vital phenomenon of spectrofluorometer as it does not require any particular orientation of fluorophores and quenchers. Therefore, ET occurs by completion of fluorescence emission and reabsorption. The dynamic ET occurs only if there is nonradiative transfer of energy from the donor to the acceptor, which happens with the close proximity of the donor and acceptor, which is recommended for the photodynamic applications.

In this condition, the regular cellulose paper that causes scattering of the emission may not give enough emission for metal free molecules, which suffer from poor quenching coefficients to cause significant quantifiable quenching at low concentrations. Further, the hydrophobicity of the fabricated sensor paper strip may also have allowed the analyte to reach closer to effective quenching at low concentrations. Although donor/acceptor distance is a minor factor in the static quenching, it cannot be ignored with the significant increase in the contact angle.

3.3.5 Real sample analysis and luminescence quenching mechanism

The evidence observed above shows that the sensor strip method developed may not require sample extraction, as the emission peak and the hydrophobicity are selective to the lycopene. Hence for the real sample analyses, tomato juice diluted to ten-fold have been taken, since the sensitivity of the sensor strip is high to 10 nM range. This may be due to the ability of the NIR excitation to overcome the background auto-fluorescence. Thus, diluted samples show concentration-dependent quenching, which has been crosschecked using the HPLC (Fig 3.14F). The reading was very close, with a difference of ~7 %. The performance comparison with recent literature is given in Table 4.

Table 4: Performance comparison with previous publication of upconversion paper using quenching and recovery principles

Analyte	Reference	Minimum Concentration
Thiram (Thiram copper complex as quencher)	[41]	100 µM
Sulphite	[39]	60 nM
Cocaine with gold nanoparticles as quenchers	[52]	5 nM
Fluoride ion (Complex formation using curcumin)	[53]	5 uM
No metal quenchers	Present work	10 nM

3.4 Conclusion

Lycopene is an important carotenoid with the highest antioxidant potential and its quantification is gaining more importance in the food and agriculture industry. A portable smartphone camera-based cost effective UCNPs sensor strip with detection limit to 10 nM free of metal quenchers has been developed which has better resolution compared to other recently published excellent work in Table 1. Due to the use of a smartphone and nanopaper-based sensor, the method can be used with little to no skill. The sensitivity of detection is significantly higher than a regular cellulose paper, probably due to the minimum scattering in the transparent paper. The strip also shows ~100 % luminescence recovery with simple washing, allowing for reusability; that gives the strips convenience for internet of things assisted data pooling from different locations, which is emphasised for future agriculture.[51]

Chapter 4

Plant Protection

Nano-maze lure: Pheromone sandwich in graphene oxide interlayers for sustainable targeted pest control

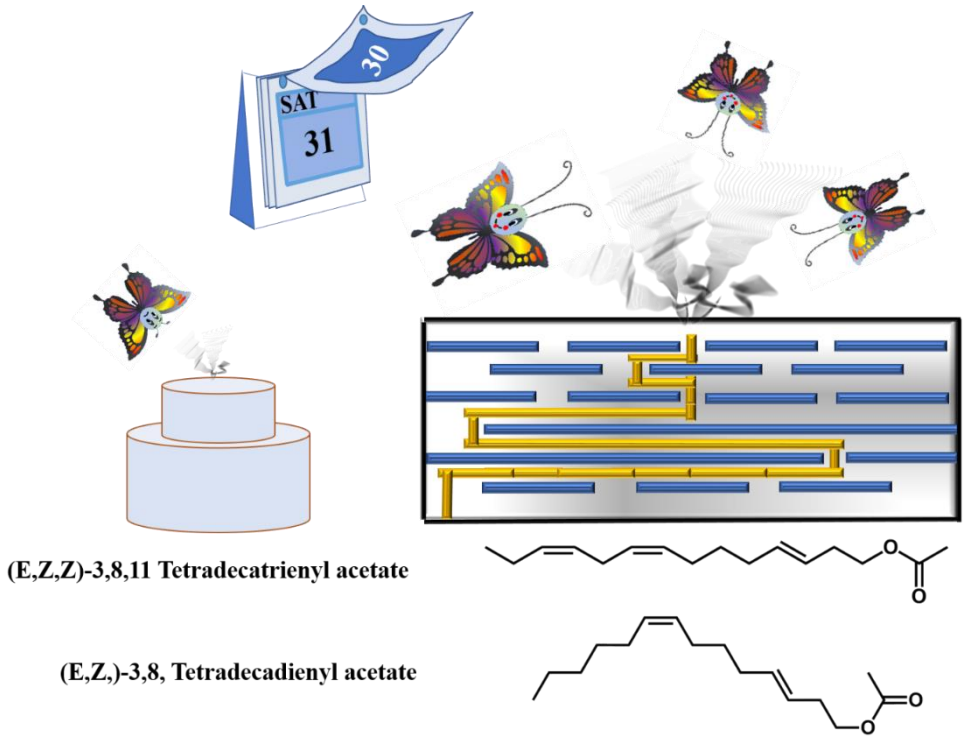

TOC. Schematic representation of pheromone release from graphene oxide nanocomposite

Abstract

Eco-friendly pest management strategies motivate the search for a platform having the ability to deliver pheromone in a controlled manner. Tomato pinworm *Tuta absoluta* is a major threat to tomato cultivation and its green management technology uses a rubber septa pheromone trap that has a short field life. Hence to overcome this problem a pheromone-composite with graphene oxide (GO) and amine-modified graphene oxide (AGO) that can extend the diffusion path has been developed. The composite stimulates an effective electrophysiological response in the antenna that qualifies it for the field test, where significantly more pests were trapped than commercial septa. Compared to AGO, the GO composite with the pheromone assembled into multilayer that increased the pheromone diffusion path, which resulted in the extension of the pheromone life that proportionally increased the pest trapped. This technique will provide

benefit to the farmers as they have longer field efficacy to keep the pest damage at low in an environmentally friendly manner.

Keywords: Graphene oxide, pheromone, volatile release, tomato, nano-agri, targeted pest control, eco-friendly, photothermal, tomato pinworm, *Tuta absoluta*

4.1 Introduction

Agrochemical viz., pesticide application ensures food security at the cost of huge damage to the environment.[219] Continuous effort by us and our counterparts led to improve pesticide efficacy with excellent multi/smart functional nanoparticles.[220–223] Slow release of the elemental sulphur and other organic pesticide from the nanoparticles and zeolite network has been realised to improve the pest control.[224,225]

Exploiting the behaviour of insect with semio-chemicals for the pest control, is an eco-friendly alternative.[226,227] Unlike the classical pesticides, which require broadcasting for pest control, this next-generation strategy requires placing the semio-chemical lure in one place in the field for mass trapping of insect pests without affecting environment. [228] Further pheromones are species-specific, hence their use do not cause damage to other non-targeted species in the ecosystem. Whereas, the pesticide cause decline in the population of beneficial insect-like pollinators, parasitoids and predators of insect pest that are noted as “friends of farmers”, which lead to imbalance in tritrophic relation.[229]

The challenge in the use of pheromone technology is the burst release thereby reducing the field efficacy of pheromone lure in a short span. This requires a matrix that can extend its release half-life along with the assurance of not altering the composition ratio. The classical method to control the release of volatile is to disperse in viscous liquid or in 3-D networks like zeolite[230] or MOF[231] or gel.[232]

On the other hand, carbon has the capacity to adsorb volatile organic compounds with the highest saturation capacity [233]. This adsorption depends on the activation and the surface morphology like the meso and microporous structure.[234,235] Following the adsorption, the volatile release kinetics has been controlled by factors, like morphology, temperature and chemical composition of the guest molecules.[236] The desirable characters of carbon as sustainable matrix, has been proved when adsorption and desorption capacity of the volatile like hexadecane on the graphitic carbon matrix was tested for multiple cycles with excellent reusability.[237] Additionally, the packing matrix can also serve as the protective shell to the agrochemicals which are susceptible to photolysis.

The carbon matrix has been shown to act as biocide by assembling as a physical barrier that limit the exchange of nutrient.[238,239] Similarly in gas the multilayer graphene oxide (GO) assembly, limits free diffusion by extending the release path and serve as the slow release platform.[240,241] The graphitic carbon like the carbon nanohorns was reported to store tetrafluoromethane in the interstitial space.[242] Tuning the interlayer space with a surfactant like dodecylbenzene sulfonate permitted the gas separation. [243] Similarly, the interlayer space tuning with the amino acid functionalization i.e. AGO led to the change in the dispersibility, absorptivity and hydrophilicity, which let to alters the permeability.[244]

Functional material with interlayer packing and wise methods to assemble 3D scaffold for bio-application by the facile solvent casting of the surface-modified platform;[245,246] motivated us to envisage surface-modified GO to assemble into 3D matrix for pheromone release kinetics. Hence, pheromone composite of GO and GO derivative i.e., AGO, have been prepared and tested for controlled release of tomato pinworm-*T. absoluta*-pheromone for eco-friendly management. This oligophagous insect possesses high reproductive ability, which could complete 10 to 12 generations per year can cause 100 percent damage to tomato under favourable conditions.[247] Farmers rely on chemical insecticides to manage the pest but

indiscriminate use has led to a decline in natural enemies, pollinators and build-up of pesticide residues in tomatoes.[248] The pheromone specific to *T. absoluta* loaded on GO/AGO has been studied for neuronal response by electroantennography and pest trapping ability at the field level. In continuation of GO's bio-avthar with the ability to cater electrical, gas bubble and thermal impulse,[196,249–251] here the diffusion maze in GO assembly has been explored for pest control.

4.2 Experimental section

4.2.1 Material used

Graphite powder and ethylene diamine were purchased from sigma. Sulphuric acid, hydrogen peroxide, orthophosphoric acid, sulphuric acid, potassium permanganate, methanol, acetone, dichloromethane (HPLC grade) and BHT (Butylated hydroxy toluene) were purchased from Merck. Dialysis bags were purchased from Thermo-scientific having a molecular weight cut off 7000. The (E,Z,Z)-3,8,11-Tetradecatrienyl acetate and (E,Z)-3,8-Tetradecadienyl acetate were provided by ATGC, Biotech Pvt. Ltd, Hyderabad.

4.2.2 Characterization

Powder X-ray diffraction was measured using Bruker D8 advance diffractometer with Cu Kα radiation source (λ=1.54) at 40 KV and 50 mA. UV-Visible absorbance spectra were measured using Cary series (Agilent technologies). TEM and HRTEM images were measured using JEOL JEM2100 measured at 200 KV. FT-IR spectroscopy was measured using vertex 70 Bruker. Raman spectra were measured using a confocal Raman system (WITEC) using a 532 nm wavelength laser. Thermogravimetric analysis (TGA) was performed under nitrogen conditions using Perkin Elmer STA 8000. GC-MS was performed for quantification of pheromone release through photothermal effect using Shimadzu GC coupled with GCMS QP 2010 plus mass detector (GC-MS) and a single quadrupole mass spectrometer Quantum

(Shimadzu) with 100 % dimethyl polysiloxane (Restek Rxi-1ms;30 m x 0.25 mm ID,0.25 µm film thickness) column. GC-MS operating conditions: Initial oven temperature is 80 °C for 5 minutes and then ramped at the rate of 20 °C per minute and then held for 15 minutes. A Bruker multimode 8 atomic force microscopy (AFM) system was used in tapping mode. Zeta potential and DLS was measured using Malvern instrument. Contact angle of graphene oxide and amine modified graphene oxide were measured using KRUSS (ADVANCE Drop shape). Electroantennogram studies were measured using Syntech instrument

4.2.3 Synthesis of Graphene oxide (GO)

GO was synthesized using modified Hummer's method. [252] Briefly, 0.5 g of graphite powder was taken with sulphuric acid and orthophosphoric acid in the ratio of 9:1. After stirring for 15 minutes, 3g $KMnO_4$ was added slowly followed by heating under constant stirring for 12-16 hours at 50 °C. The reaction mixture was then cooled to room temperature followed by the addition of 67 mL of cold water. After cooling the reaction is terminated using 0.5 mL of 30 % H_2O_2 solution. The resulting mixtures are centrifuged and the supernatant is decanted followed by washing with acid, ethanol and water. Finally, the GO was neutralized by dialyzing with distilled water and the material is dried in the oven for its further use.

4.2.4 Synthesis of amine-modified GO (AGO)

About 25 mg of GO was dispersed in 10 mL of 95 % ethanol followed by the addition of 500 µl of ethylenediamine. The mixture was probe sonicated for 1 hour and kept for stirring at room temperature for 24 hours. Finally, the mixture was centrifuged at 6428 rcf for 20 minutes and washed two times individually using methanol, ethanol and acetone. Both GO and AGO were characterized with the absorbance spectra, Raman and TEM before loading the pheromone.

4.2.5 Preparation of pheromone nanocomposite

T.absoluta pheromone (E, Z, Z) 3,8,11-Tetradecatrienyl acetate and (E,Z)-3,8-Tetradecadienyl acetate 9:1 ratio) was diluted in DCM at 1:2 ratio, following which GO and *T.absoluta* were added in the ratio of 1:1 (w:v). This was allowed to air dry. Similarly, this was followed for AGO and pheromone. The samples were characterized with FTIR, zeta and DLS size analyzer and Thermogravimetric analyser before and after loading the pheromone.

4.2.6 Rearing of tomato pinworm, *Tuta absoluta*

The tomato pinworm *T.absoluta* was collected from tomato fields Malur in Karnataka, Southern India in 2019. The culture was initiated with 100 field larvae released on potted tomato plants var *Sivam* that was placed in a wooden cage (60 x 40 x 40 cm) with nylon mesh having a cloth sleeve on one side of the cage for collecting the insects. The cages were maintained in the glasshouse with temperatures ranging from 25-28°C (± 0.5). *T.absoluta* adult males (3 days old) collected from the colony were used for assessing the antennal response in electroantennography.

4.2.7 Electroantennography (EAG)

The response of *T.absoluta* adult male antennae (3 days old) to pheromone was recorded using an electroantennographic system (Syntech). The dual-electrode probe was used for mounting the antennae. The antennae were carefully excised from the head of adult *T.absoluta* and mounted between the electrodes by placing the basal portion containing the scape to the ground electrode and the proximal tip of the antennae to the recording electrode using a conductive gel (Spectra 360 Parker, Orange, New Jersey) (Scheme 1). The clean air (activated charcoal filtered) was continuously flushed over the antennae from the delivery tube placed 15 mm away from the antennae.

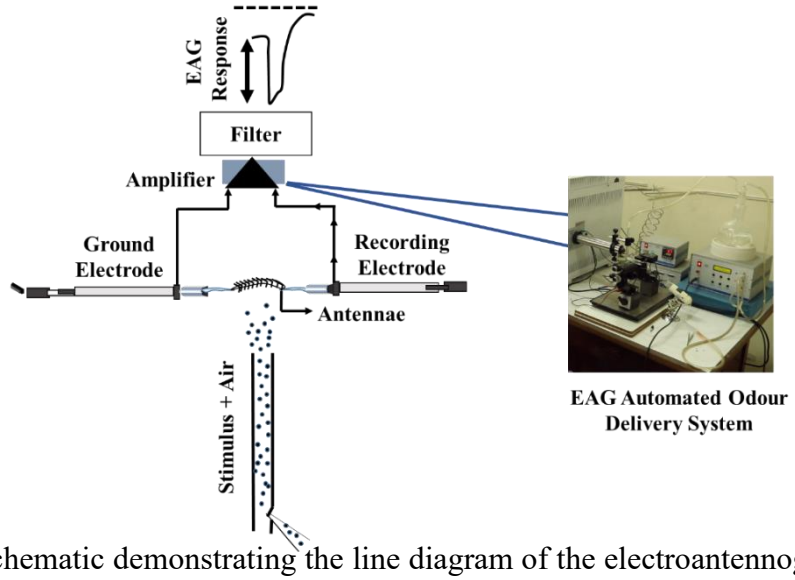

Scheme 1. Schematic demonstrating the line diagram of the electroantennogram (EAG) setup arranged with antennae. The insect antennae were fixed in between the ground electrode and recording electrode and various kinds of stimulus and EAG response was measured.

The pheromone of *T.absoluta* [(E,Z,Z)-3,8,11-Tetradecatrienyl acetate and (E,Z)-3,8-Tetradecadienyl acetate in 9: 1 ratio] was diluted in HPLC grade dicholoromethane to achieve a concentration of 160 µg μL^{-1}. One µL of the aliquot amounting to 160 µg of the pheromone was placed on Whatman filter paper strips (Advantec 5C (110 mm) Japan of 2 cm length and 4 mm diameter). The filter paper was dried for 5 minutes in the fume hood and then it was inserted into the Pasteur pipettes. This was connected to a Tygon silicone tube to the stimulus controller (CS 05 Syntech). The first puff was blown off after 30 seconds of placing the filter paper in Pasteur pipette. After sixty seconds, the antennae mounted in the electrodes were exposed to the vapor phase of the stimulus through the delivery tube placed 15 mm upstream from the antennae that had continuous air stream (pulse time 0.5 seconds, continuous flow 25mL s^{-1}, pulse flow 21 mL s^{-1}) as suggested before.[226] This was done to ascertain the physiological response of the antennae to the pheromone of *T.absoluta.*

To ascertain the antennal response to pheromone loaded in GO and AGO, the matrix (0.5 mg) loaded with *T.absoluta* pheromone (amounting to 160 µg) was placed in the Pasteur pipettes. The stimulus was applied by allowing the airstream to flow over the pheromone-loaded matrix

and reach the antennal surface. A time delay of 20 seconds was maintained between the stimuli. The summated response of the neurons in antennae was recorded through a high impedance probe that was connected to an amplifier (IDAC-4, Syntech). The recorded signals were analyzed with EAG software (Syntech). The solvent control stimulus (Filter paper with dichloromethane (DCM alone) was exposed to the antennae at the beginning, middle and end of each session. The EAG responses of pheromone (alone and when loaded in dispensers) were recorded after correcting for solvent and other background effects as described previously.[253,254] Four replicates with 10 antennae from adult males of *T.absoluta* (pooled population) were used for the study.

4.2.8 Assessing the field efficacy of pheromone loaded in GO and AGO

To assess the performance of *T.absoluta* pheromone-loaded GO and AGO composite, a field trial was conducted in the tomato field (Variety Sivam) in Malur in Karnataka, India. The composite was prepared by mixing 3 mg of GO /AGO, 1 mg of pheromone 0.5 mg of PVP and 0.25 mg of butylated hydroxytoluene (BHT) in 10 µl of DCM in a 1.5 mL Eppendorf tube. The mixture was vortexed for 5 minutes and the solvent was allowed to evaporate before closing the lid of the tube. The Eppendorf tube with the composition was hung in the centre of the plastic sticky sheet (A3 size) to trap the pest. The commercial lure in silicone septa containing 3 mg pheromone of *T. absoluta* was also attached to plastic stick traps and was hung similarly. The sticky traps alone and traps with GO /AGO blanks were maintained as control. These lures were randomly placed 25 feet apart. The number of insects trapped was counted at weekly intervals four times during the experimental period. Four replications were maintained per treatment and the traps were interchanged after each observation to prevent location bias.

4.2.9 Statistical Analysis

ANOVA and Tukey's analysis has been adopted to calculate the difference in significance of the data at P>0.05.

4.3 Result and discussion

For the judicious use of the pheromone of *T. absoluta* that volatilize quickly, here a graphene oxide (GO) based matrix has been used.

4.3.1 GO/AGO characterization Since the functional groups on the GO decide the interlayer distance, which in turn decides the diffusion of the volatiles, here we employed two kinds of GO. One, as prepared GO obtained from the improved Hummer method,[252] and the other amine-functionalized (AGO) has been synthesized as mentioned in our previous work by the simple addition of nucleophilic ethyl diamine on the electrophilic epoxy in the as-prepared GO.[255]

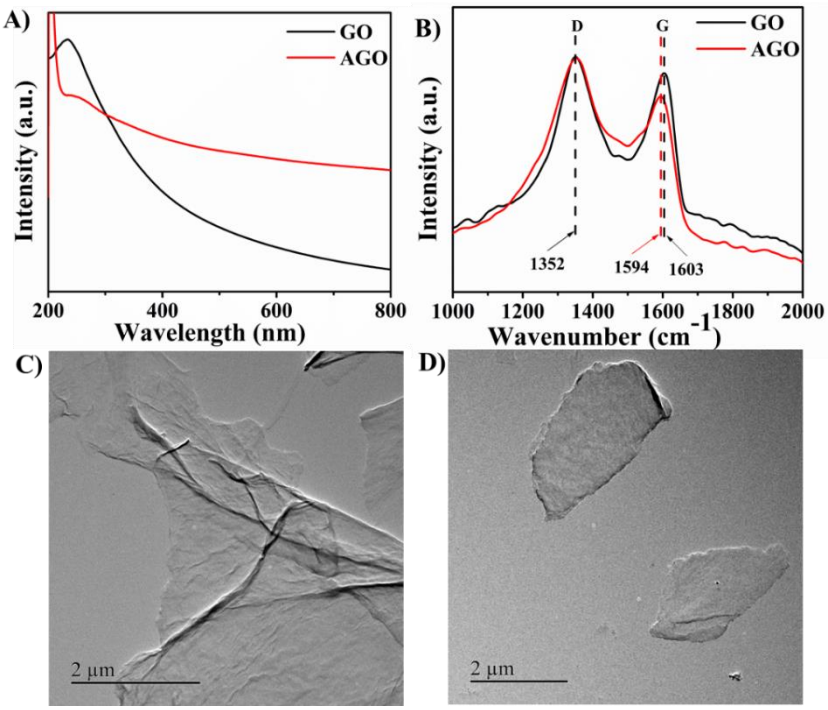

Fig 4.1 Characterization of GO and AGO (A) UV-vis absorbance spectra of GO and AGO. (B) Raman spectra of GO and AGO. (C) TEM images of GO and, (D) AGO nanosheets.

Both the GO and AGO were characterized for the optical property with the absorbance and Raman spectra (Fig 4.1 A, B). The GO shows a maximum at 233 nm, which after the amine conjugation shows redshift to 244 nm, this may be due to the reconstruction of the sp^2 bond. The Raman spectra (Fig 4.1B) shows both the D and G peak at 1350 cm^{-1} and 1600 cm^{-1} respectively, which confirms the graphitic nature of the material.[256–258] The G peak in the AGO sample was slightly shifted to the lower wavenumber, which may be due to the electron-donating nature of ethylenediamine in AGO or due to the reduction in the staking of number of sheets.[259] Following this, the structure of the material was observed with the TEM imaging (Fig 4.1C and Fig 4.1D), which shows the typical 2D structure spread as the translucent mat. The EDX analysis of the corresponding samples is shown in the Fig 4.2.

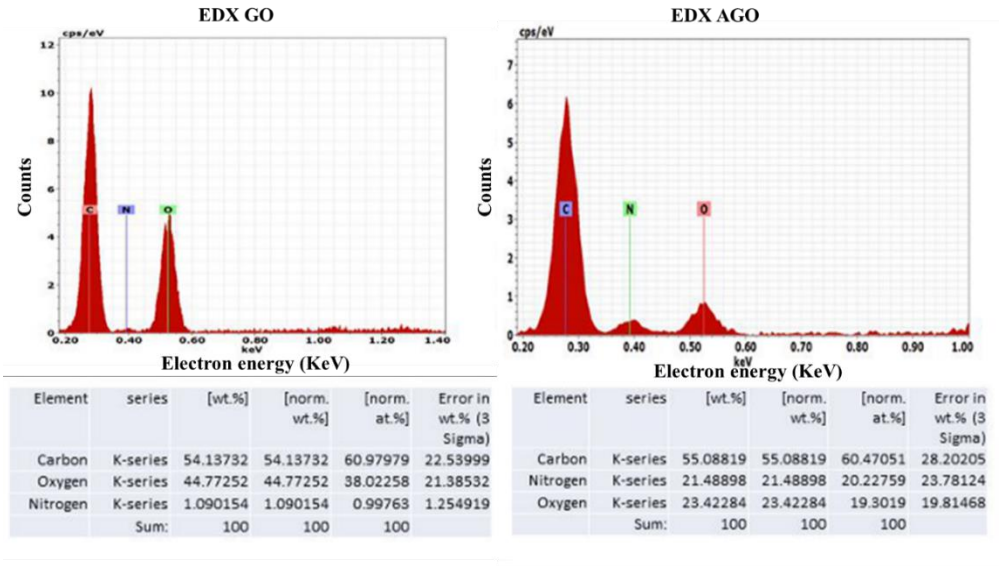

Element	series	[wt.%]	[norm. wt.%]	[norm. at.%]	Error in wt.% (3 Sigma)
Carbon	K-series	54.13732	54.13732	60.97979	22.53999
Oxygen	K-series	44.77252	44.77252	38.02258	21.38532
Nitrogen	K-series	1.090154	1.090154	0.99763	1.254919
	Sum:	100	100	100	

Element	series	[wt.%]	[norm. wt.%]	[norm. at.%]	Error in wt.% (3 Sigma)
Carbon	K-series	55.08819	55.08819	60.47051	28.20205
Nitrogen	K-series	21.48898	21.48898	20.22759	23.78124
Oxygen	K-series	23.42284	23.42284	19.3019	19.81468
	Sum:	100	100	100	

Fig 4.2 EDX analysis showed the elemental analysis for GO and AGO samples.

The appearance of the nitrogen in the AGO samples confirms that amine is tethered to the GO. Further to know the effect of functional groups on the hydrophilicity contact angle has been measured. Both the GO and AGO showed hydrophilicity (~75˚), this corroborates to the previous observation of GO.[260] In case of AGO raise in the contact angle is expected due to

the partial restoration of sp^2 graphitic structure, but in our experiment there was no significant raise in the angle.

4.3.2 Preparation and characterization of *T. absoluta* pheromone and GO composite

T.absoluta pheromone contains 2 alkyl acetate viz., (E,Z,Z)-3,8,11-Tetradecatrienyl acetate and (E,Z)-3,8-Tetradecadienyl acetate in 9: 1 ratio. The composite was prepared by mixing 3 µL of the pheromone in 5 µL DCM into 3 mg of the matrix, followed by gentle drying.

To confirm the loading interaction of pheromone in the GO and AGO, the composites before and after the loading i.e., GO@*T.absoluta and* AG0@*T.absoluta* were measured for the hydrodynamic size and zeta (Fig 4.3 A). The hydrodynamic size has been found to reduce interestingly. This reduction may be due to the separation of the GO layer that may have aligned laterally together before the addition of the *T.absoluta* pheromone. In the surface zeta measurement, the GO that expressed a strong negative charge shifted to show a weak negative charge after the pheromone loading i.e., GO@*T.absoluta*. The initial negative charge may be due to the –COO and enolic/phenolic groups on the edge whose distribution increase with oxidation and reduction in size.[261–263] In the case of the AGO, the loading of the *T.absoluta* pheromone caused the surface charge to become strongly positive. One common reason for the shift from negative to neutral or positive charge in both the GO and AGO platform could be due to the masking of the negatively charged carboxyl groups on them. Thus, this masking may cause the GO to show weak negative strength, and AGO to express the amine better for the strong positive surface charge expression. Overall observation proves that before assembling by evaporation the composite in the free medium to express noncovalent interaction.

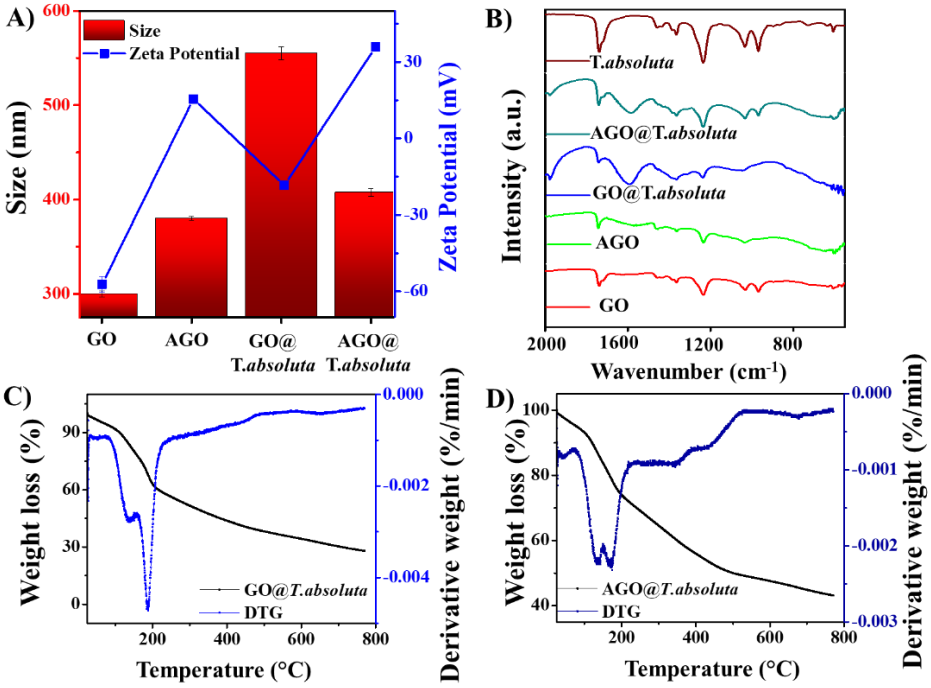

Fig 4.3 Characterization of nanocomposite with *T.absoluta* (A) Zeta potential and hydrodynamic size distribution, (B) FTIR spectrum measured for GO, AGO, nanocomposites and *T.absoluta* pheromone measured in the range of 400 cm^{-1} to 2000 cm^{-1}, (C and D) TGA and DTG plot for nanocomposite i.e. GO@*T.absoluta* (C) AGO@*T.absoluta* (D) respectively measured in the temperature range up to 800 ˚C.

Following the hydrodynamic size and charge dynamics study with the loading, the binding assisted change in the bond structure has been studied with FTIR (Fig 4.3B). The peak at 1038 cm^{-1}, 1200 cm^{-1}, 1404 cm^{-1} and 1720 cm^{-1} in GO corresponds to C=O, epoxy C-O-C stretch, C-OH stretch, and carboxy -COOH stretching vibrations respectively. In AGO a a broad depression peak appears at 1580 cm^{-1} which corresponds to N-H plane stretching vibrations.[264]After the pheromone loading both the GO@*T.absoluta* and AGO@*T.absoluta* platforms show the appearance of the peak at 960 $cm^{-1}$and 1365 cm^{-1}, which doesn't appear prominently before loading the pheromone in native GO and AGO. These two peaks correspond to alkene group i.e., C=C bending and C-H bending in the pheromone respectively. A strong peak that appears at 1030 and 1230 cm^{-1} corresponds to ester C-O stretching, which

also confirms the pheromone loading. TGA has been carried out for the pheromone loaded composite to evaluate the binding efficiency of the pheromone on GO and AGO. In GO@*T.absoluta* and AGO@*T.absoluta* (Fig 4.3C and Fig 4.3D), the pheromone peak identified at 225 ˚C is missing, as it shifts to merge with the weight loss peak above 250 ˚C followed by another peak at 430 ˚C. This concludes that the thermal stability is improved in the prepared nanocomposite i.e., GO@*T.absoluta and* AGO@*T.absoluta.*

The pheromone *T.absoluta* shows a single sharp peak at 225 ˚C corresponding to the removal of organic compounds that constitute the pheromone (Fig 4.4).

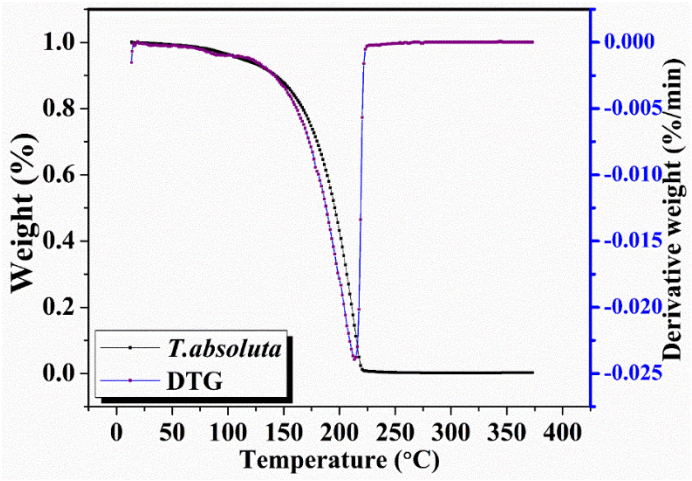

Fig 4.4 The comparison of the TGA and DTG plot recorded for the pheromone of *T.absoluta* against the variation of temperature ranged from 0-400 °C.

Following this the blank AGO and GO shows a typical DTG sharp peak at ~50 ˚C and ~170 ˚C, corresponding to the water and oxygen functionalities respectively as shown in Fig 4.5.[265] Then a minor peak is observed at 300 ˚C and then the next gradient above 500 ˚C which corresponds to the high-affinity functionalities and carbon/amine-carbon elimination respectively.[266]

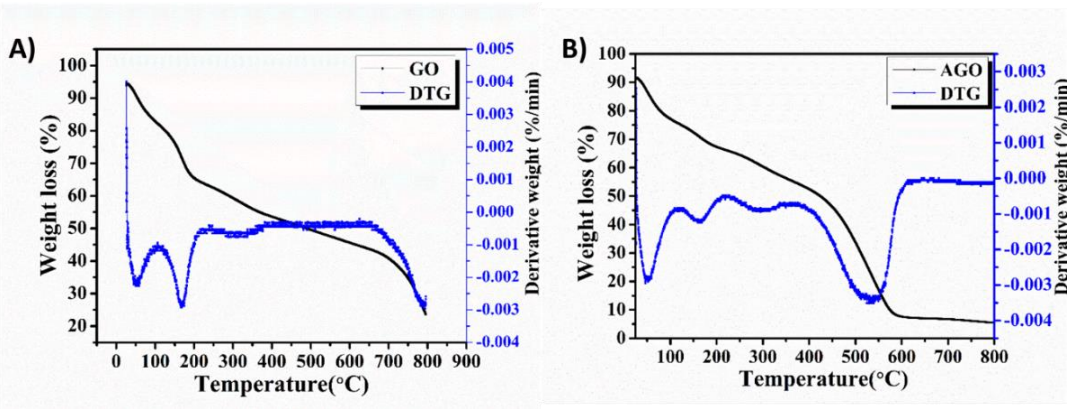

Fig 4.5 The comparison of TGA and DTG plot for A) GO B) AGO measured in the temperature range up to 800˚C.

Further the TGA of GO composite with individual pheromone component i.e., (E, Z)-3,8, Tetradecadienyl acetate and (E,Z,Z)-3,8,11 Tetradecatrienyl acetate (Fig 4.6) also showed the weight loss extending from 250 ˚C to 450 ˚C . This clearly demonstrates that the pheromone elimination temperature has been shifted to a higher temperature, which may cause expected controlled release.

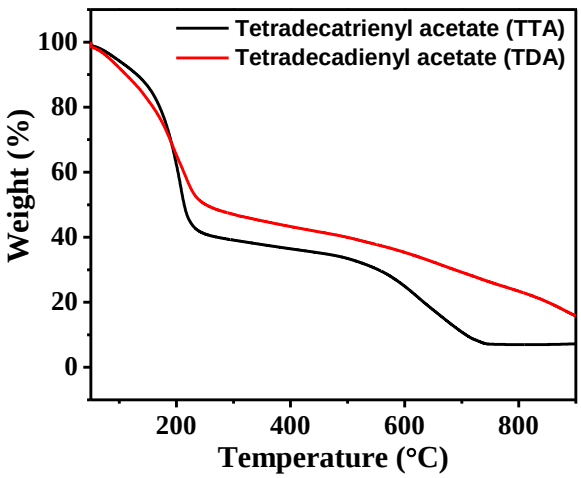

Fig 4.6 TGA plot for nanocomposite with individual components of *T. absoluta i.e.,* GO@tetradecadienyl acetate (GO@TDA) and GO@tetradecatrinyl acetate (GO@TTA).

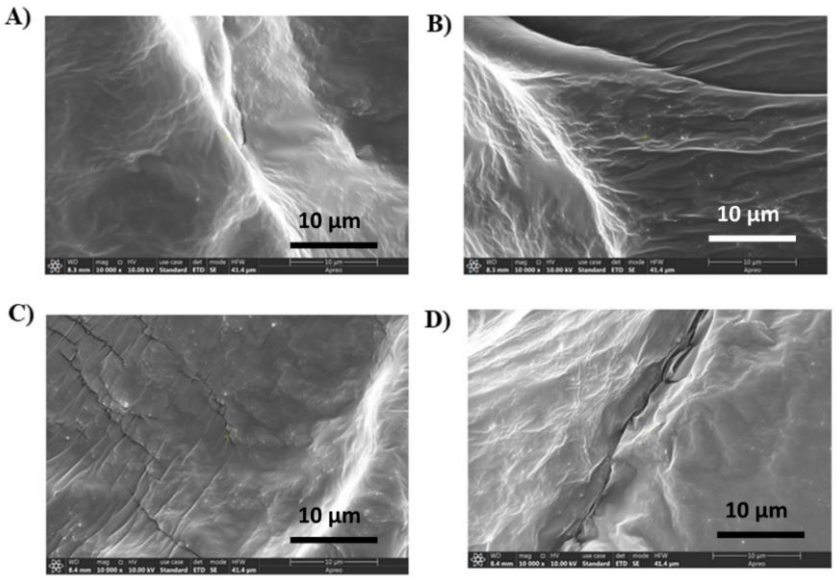

Fig 4.7 FE-SEM image of GO and AGO (A and B) FE-SEM images of GO sheets and AGO respectively, (C and D) FESEM images of the GO@T.absoluta and AGO@T.absoluta respectively.

The morphology of the samples was studied under SEM (Fig 4.7), to know the three-dimensional arrangement of the matrix that controlled the diffusion of the *T.absoluta* pheromone, which is an important property for sustained release. SEM images of GO and AGO is given in Fig 4.7A and Fig 4.7B. Interestingly GO@*T.absoluta* composite shows the layered arrangement of the matrix into a maze-like scaffold, which didn't appear in AGO@*T.absoluta* composite (Fig 4.7C and Fig 4.7D). To understand the effect of the presence and absence of the layered arrangement in GO@*T.absoluta* and AGO@*T.absoluta*, respectively on the thickness, the composite was analyzed under the AFM. As the diffusion is inversely proportional to the path length, which is further proportional to the thickness.[267]

The initial AFM study of the matrix before loading *T.absoluta* pheromone the GO and AGO shows ~5 nm and ~4 nm thickness, respectively (Fig 4.8A and Fig 4.8B). The thickness in GO and AGO corresponds to ~10-12 sheets and ~5-6 sheets respectively.[268] This corroborates with the Raman spectra, where the reduction in the number of sheets resulted in the appearance of

the 2D peak in AGO (Fig 4.9) however the peak is so broad whose peak maxima is not clear to find the shift towards larger wavenumber.[259]

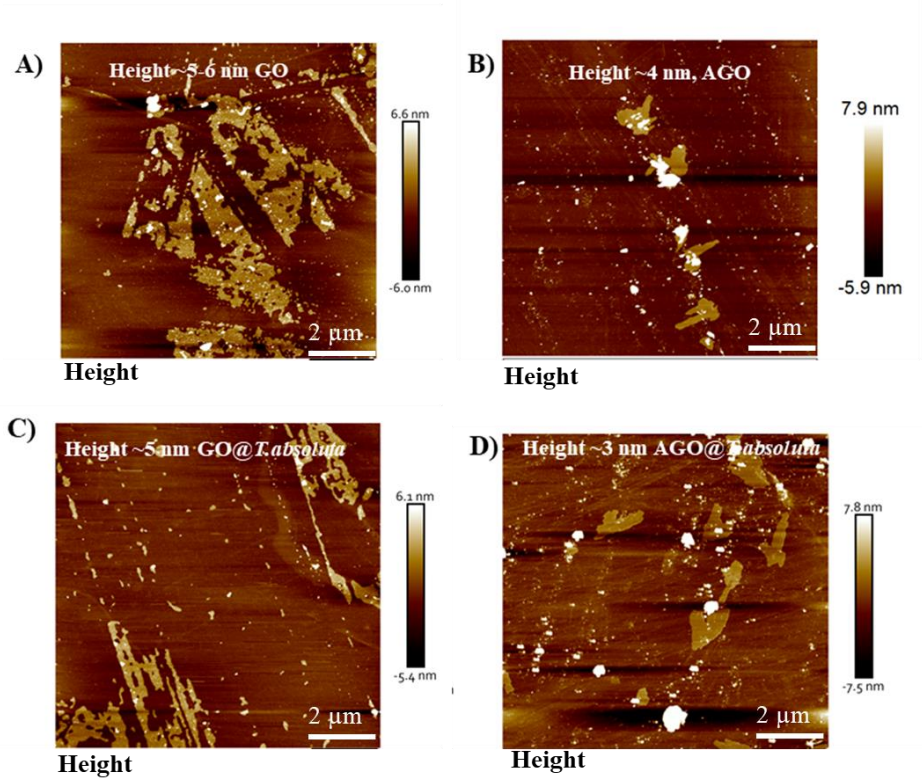

Fig 4.8 AFM height profile of GO, AGO and nanocomposite (A and B) AFM height profile of GO and AGO sheets respectively. (C and D) shows the height profile of GO@*T.absoluta* and AGO@*T.absoluta* nanocomposite respectively

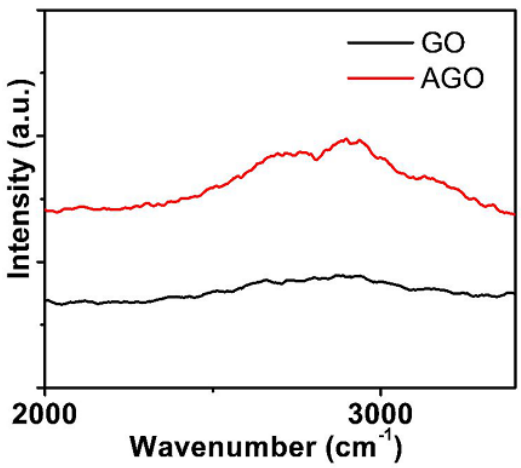

Fig 4.9 Raman spectra recorded for graphene oxide (GO) and amine modified graphene oxide (AGO) resulting in the appearance of 2D peaks in AGO.

After pheromone loading GO@*T. absoluta* composite shows the average thickness to be ~5 nm, whereas AGO@*T.absoluta* composite shows the average thickness to be ~3 nm (Fig 4.8C and Fig 4.8D). Thus in GO@*T.absoluta* composite there is almost no change in the thickness compared to the as-prepared GO. Whereas in the case of AGO@*T.absoluta* composite the thickness is reduced to half the dimension compared to the initial AGO thickness. It elucidates that the interaction of the AGO with the *T.absoluta* pheromone may have established steric hindrance to the layers of the sheets thus limiting the reaggregation. Whereas in the GO it may have led to supramolecular binding assisted self-assembly.

4.3.3 Electrophysiological response of pheromone

The electrophysiological response of the olfactory receptor neurons of adult males of *T. absoluta* has been studied to check if the pheromone *T.absoluta* loaded into the GO and AGO were faithfully released (in an appropriate ratio) to cause a neuronal response. For this, the antennae of the adult *T.absoluta* males were exposed to the headspace of the nano-matrix loaded with pheromone. To compare the efficiency, the commercial pheromone release matrix *viz.*, silicone rubber septa have been used. The volatile headspace of pheromone over the nano-matrix (GO and AGO) and silicone rubber septa caused ~1.2 mV electrophysiological response as shown in Fig 4.10A. The antennal response to pheromone stimulus from the silicone septa and the nano-matrix GO@*T.absoluta* /AGO@*T.absoluta* were at par. This indicates that the pheromone blend loaded into the nano-matrix has been able to release the appropriate ratio to cause the neuronal response. Whereas the antennae were exposed to air as control and the GO/AGO blank caused < 0.2 mV response.

4.3.4 Assessing the field efficacy of pheromone loaded in nano-matrix

The field trial laid to assess the efficacy of the pheromone loaded in nano-matrix revealed that pheromone *T.absoluta* (1 mg) loaded in GO had a numerically higher number of pests per trap (1015) as compared to the pheromone loaded in AGO (781) as shown in Fig 4.10B. This difference may be attributed to the material property to form stacked layers by the GO, which may aid in the sustainable release that led to more traps than the AGO. Surface functionalization assisted control in the pesticide release in liquid medium with/without stimuli contributing to different pattern of diffusion has been shown to have significant improvement in the crop protection.[269–271] In the gas mobility the porous surface of the carbon material and its interaction has been known to control the diffusion.[272] Interestingly, both the matrices GO@*T.absoluta* and AGO@*T.absoluta* trapped a higher number of the pest as compared to the pheromone loaded in commercial silicone septa that had 3 mg pheromone. The GO@*T. absoluta* and AGO@*T.absoluta* -based matrix with a lower load of pheromone (1mg) had a higher catch as compared to commercial lure having 3 mg. This suggests the nano-maze-like layered assembly to cause better trapping of insects in spatio-temporal scale as the control, GO and AGO blank trapped less than 10 pests per trap. The view of the experimental field and *T.absoluta* attracted to pheromone loaded GO trap is shown in Fig 4.10C and Fig 4.10D

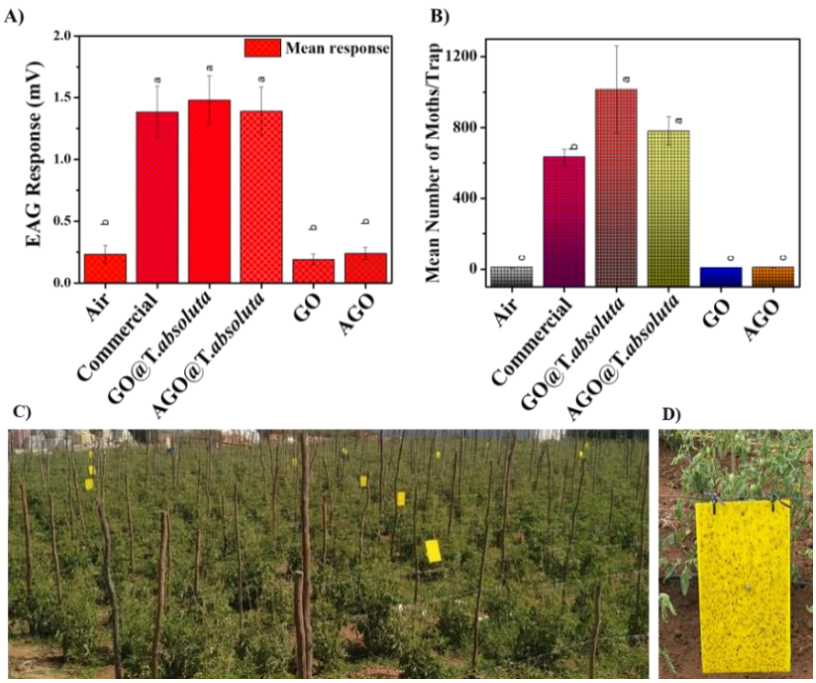

Fig 4.10 Field study of nanocomposite with EAG response **(**A) EAG measurement in response to Air, commercial septa, GO@*T.absoluta*, AGO@*T.absoluta* , GO and AGO. Statistical significance between Air-GO, Air-AGO and Air-commercial has p value <0.001 (***) whereas the statistical value between commercial-GO and commercial-AGO is non-significant. (B) Mean number of pest entrapped/trap in different treatments. (p> 0.05),Statistical-significance between Control- GO@*T.absoluta* and Control- AGO@*T.absoluta* has p value <0.001 (****)*.* Results are represented as Mean ±S.E. (C) View of the experimental field to assess the efficacy of *T.absoluta* pheromone. (D) *T.absoluta* moths attracted to pheromone loaded GO composite trap.

4.4 Conclusion

Exploiting the pheromones-pest interaction, for tapping the insect promises sustainable agriculture by substituting the pesticide assisted crop protection that causes irreparable environmental damage. Commercial lures (rubber/silicone) used to deliver *T. absoluta* pheromone have a short field life due to the quick release of pheromone from the matrix. To address this limitation, two GO scaffolds were prepared to hold the pheromone. In this the pristine GO scaffolds having maze-like staking caused the controlled release of pheromone by the diffusion path extension. This in turn enhanced the field efficacy of the GO lure loaded

with *T. absoluta* pheromone by extended pest control. From this study the controlled release nano formulation for the biological application being limited to drug delivery in liquid medium until now,[42] will get new perspective to extend as solid-state assemblies for controlled pheromone release and pest control. To give future scope to this study the photothermal stimuli-controlled pheromone release from the composite has been assessed (Fig 4.11 and Fig 4.12).

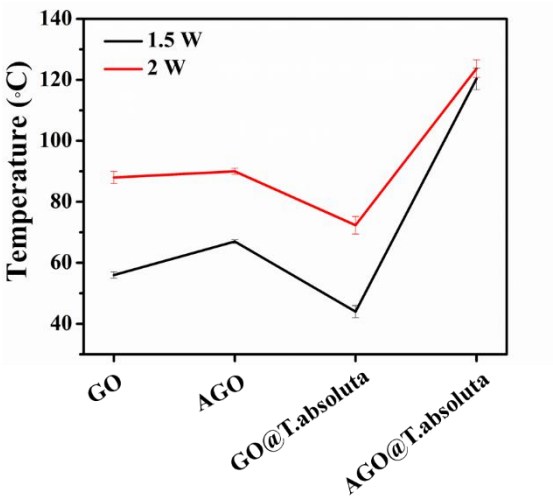

Fig 4.11 Solid state photothermal activity of GO, AGO, GO@*T.absoluta*, and AGO@*T.absoluta*) measured by irradiating at a wavelength of 808 nm for 10 min at 1.5 and 2 Watt Power.

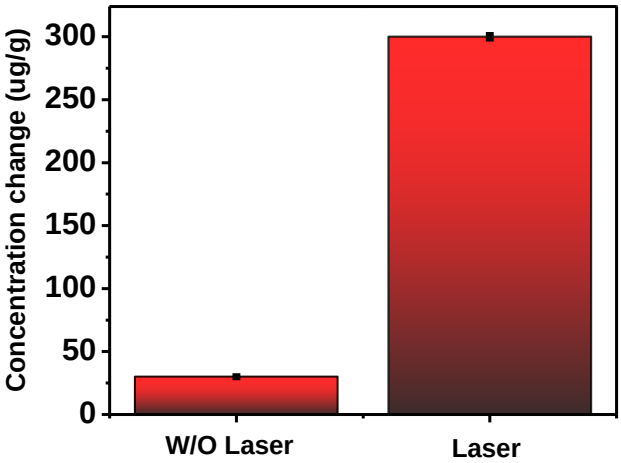

Fig 4.12 Comparison of the concentration increase of *T.absoluta* pheromone with and without laser irradiation. The *T.absoluta* pheromone on irradiation with 1.5 W laser (808 nm) showed ~10 times higher concentration change to that of non-irradiated sample.

In this process the solid state material under the 808 nm laser illumination started to give fumes, hence the release was quantified in the solvent, which showed good stimuli triggered release as in cancer drugs;[273,274] but needs fine tuning to adopt for this application. Further there is a tremendous scope for this work to extent for other pheromone ratio, multi pest pheromone ratio, as well as to check the potential of the matrix to reuse etc.

Chapter 5

Summary and conclusions

Conclusions

Chapter 1

The first part of introduction discusses about Vitamin D and its associated health benefits. Just after COVID-19, there has been an increased awareness among the rising health benefits of this vitamin. Vitamin D sources include fish, meat, chicken and vegetarian sources includes mushrooms and milk. However, the only vegetarian source is the mushroom. So, food fortification is important to meet daily nutritional requirement and needs of the living beings. The mushrooms constitute of sterols, in which 90 % is ergosterol, which can be converted to vitamin D_2 using UV light. The practice is already in commercial use in US but limitation is poor penetration depth of UV light. Therefore, this chapter summarises different techniques employed in the mushrooms *i.e.*, varying mushroom varieties, thickness of the mushroom tissue, time duration of UV treatment and its gap. To fulfil this gap the upconversion nanoparticles that can source UV light using NIR light excitation that can penetrate deep inside the mushrooms is envisaged for efficient ergosterol conversion to vitamin D_2.

Hence, the second part of introduction is comprised of basic literature survey describing upconversion nanoparticles. These are composed of an inorganic host lattice with lanthanide ions as dopants and tuneable emission in the visible and NIR region. There are various mechanisms associated with energy transfer in the upconversion nanoparticles. Energy transfer upconversion is one of the most efficient energy transfer mechanisms. Mostly used sensitizers in upconversion nanoparticles are ytterbium due to broad absorption in NIR region and activators are thulium and erbium due to their ladder like energy levels. Biomolecules and inorganic ions sensing is accomplished using different sensing mechanisms like inner filter effects, photo induced electron transfer, FRET etc. The basic criterion for sensing can be accomplished following an overlap in the absorbance spectrum of the analyte with the upconversion nanoparticles emission spectrum.

In the optically important nanomaterials, next to fluorescent material the photothermal materials get maximum attention. The third part of introduction deals with photothermal associated release of target moiety from the nanocomposite. Photothermal therapy cause heating of the local environment around the cells for effective destruction of cancer and malignant cells. The rise in temperature is the main cause for cell destruction as it destroys lipids, membranes and proteins. Various types of nanomaterials are considered photothermal responsive, in which gold nanoparticles are considered as standard for their effective targeted based cancer killing by having longitudinal plasmonic band in the NIR region. Also, various carbon-based materials are used due to its basal planar structure, high surface area and optoelectronic properties. This intrigues our interest to explore pheromone integrated graphene oxide for photothermal triggered pheromone release and pest control.

Chapter 2

Vitamin D, also known as the "sunshine vitamin" plays a vital role in calcium homeostasis, fighting cancer, heart diseases, multiple sclerosis etc., by maintaining healthy immune system. Vitamin D_3 is synthesized in the body by the exposure of sunlight, which cause the conversion of 7- dehydrocholestrol in skin to pre-vitamin D_3 that finally isomerises to vitamin D_3. However, due to sedentary indoor lifestyle the exposure to sunlight is minimum now a days, which cause vitamin D deficiency worldwide. Vitamin D deficiency is measured in the body using 25-hydroxy vitamin D in blood serum. A serum concentration of less than 20 ng mL^{-1} is identified as vitamin D_2 deficient patients.

Vitamin D_2 is an isoform, as beneficial as vitamin D_3 to maintain serum vitamin D levels. The sources of vitamin D_2 include fish, meat, egg, red meat (non-veg sources) and mushroom (only vegetarian source).

However, the Vitamin D_2 in mushrooms is not readily available, but present in the form of ergosterol, a provitamin D_2, which converts into vitamin D_2 only in the presence of UV radiation, by the cleavage of B ring in the structure. This conversion is found useful for many different types of mushrooms like button, oyster, shiitake etc. The UV light assisted conversion in mushrooms is already in commercial practice in US, but the limitation of this method is the poor penetration depth of UV light. Therefore, optical nanomaterials such as upconversion nanoparticles i.e., $NaYF_4$, Yb^{3+}, Tm^{3+} are of significant importance as it converts deep penetrating NIR wavelength (980 nm) to UV light using an anti-stokes process. Therefore, we synthesized $NaYF_4$, Yb^{3+}, Tm^{3+} nanoparticles, and spin coated it on quartz cover slips for the insertion into the interlamellar space in mushrooms (*A.bisporus*) to enable ergosterol conversion. The concentration of nanoparticles to be spin coated was optimised as 400 ppb with respect to yttrium concentration (measured using ICP-MS).

Thus prepared three quartz disks were placed at an equal interlamellar distance and exposed to different radiations viz. 980 nm laser, sunlight and solar simulator (only NIR light). Also, three different controls were maintained *i.e.*, control mushroom without any irradiation, mushroom exposed to UV light (2 hours) and mushroom exposed to sunlight (2 hours).

After the exposure of mushrooms, the samples were subsequently lyophilized and vitamin D_2 has been extracted *via.*, saponification for quantification by HPLC in methanol/acetonitrile gradient flow using PDA detector (wavelength 265 nm). Control mushroom without any irradiation show ~5 µg vitamin D_2 g^{-1} dry weight. In case of mushrooms exposed to UV light, vitamin D_2 content increased to ~ 32 µg g^{-1} dry weight and in case of 980 nm laser exposure (1 hour) in mushrooms using UCNPs coated disks, the conversion increased to ~ 57 µg g^{-1} dry weight of mushroom. This is the highest conversion in *A. bisporus* till date. Also, in case of UCNPs coated disks in sunlight, the conversion was ~ 23 µg/g which was 2.5 times enhancement as compared to control.

Chapter 3

Lycopene is an important carotenoid with the highest antioxidant potential and an indicator of crop quality; hence its quantification is gaining more importance in the food and agriculture industry. Lycopene is abundant in tomato and other few crops and is extracted using expensive methods. The health benefits of lycopene include better cardiac health, reduces risk of cancer, organ disorder and improves fertility.

Lycopene is acyclic with 5, 9, 13, and 15 position isomers having 3 absorbance maxima between 400 to 510 nm, which draws special attention for having the highest reactive oxygen removal rate among all carotenoids (Kq : 31 x 10^9 M^{-1} S^{-1}).[212,213]

To sense this by fluorescence technique, the use of upconversion nanoparticles that have NIR excitation has been envisaged, due to its inherent property of less background interference. Upconversion nanoparticles $NaYF_4$, Yb^{3+}, Tm^{3+} were prepared having a maximum emission at 475 nm. The emission overlapped with lycopene absorbance and it was found to quench the upconversion fluorescence with increasing lycopene concentrations. The sensitive fluorescence-based sensing technique has been developed to measure the concentration down to 80 pM from 120 nM with just 0.5 mg mL^{-1} of upconversion nanoparticles. Recently, many smartphone-based sensors have been developed for the detection of sugars, nucleic acids, metals, covid virus etc. using fluorescent nanoparticles embedded in a substrate like cellulose. Hence, a portable smartphone camera readable cost effective UCNPs sensor strips were prepared from cellulose nanocrystals and poly vinyl alcohol with detection limit to 10 nM. This resolution has been achieved without the use of metal quenchers. Due to the use of a smartphone and nano paper-based sensor, the method can be used with little to no skill. The sensitivity of UCNPs embedded in nanocellulose is significantly higher than a regular cellulose paper, probably due to the minimum scattering in the paper. The strip also shows ~100 % luminescence recovery with simple washing, allowing for reusability; that gives the strips

convenience for internet of things assisted data pooling from different locations, which is emphasised for future agriculture.[51]

Chapter 4

Tomato pinworm (*Tuta absoluta*) is a major threat to tomato cultivation. In the absence of good pheromone release technology, managing this pest using pesticide will face different problems. Generally, the pesticide drift, volatilisation and leaching cause less efficiency; and specifically, the pest mines inside the leaf hence they stay protected in spite of the presence of pesticide on the leaf.

Eco-friendly pest management strategies motivate the search for pheromone assisted pest control strategy. The widespread adoption of this technology demands for the platform having the ability to deliver pheromone in a controlled manner. Present pheromone technology employs use of dispensers and rubber septa. The pheromone employed in these dispensers quickly volatilizes and needs a quick refill. Ideally, the layered materials like the graphene oxide could sandwich the pheromone in the interlayer gap and harness the pheromone release. Two types of 2D layers *i.e.*, graphene oxide (GO) and amine-modified graphene oxide (AGO) that can extend the diffusion path has been developed. The composite was tested for electrophysiological response before taking to field levels. The nanocomposite stimulated similar response in comparison to the commercial formulation, which qualifies the nanocomposite for the field study.

The field study of this nanocomposite with 1 mg of the pheromone load has been able to capture a greater number of insects in comparison to 3 mg of pheromone in the commercial formulation. Compared to AGO, the GO composite with the pheromone assembled into multilayer increased the pheromone diffusion path, that proportionally increased the pest trapped. This technique will provide benefit to the farmers as they have longer field efficacy to

keep the pest damage at low in an environment friendly manner. Further at the end, the composite has also demonstrated the ability to deliver the pheromone in a controlled fashion, by photothermal effect using light as stimuli.

Future Work:

Previous chapters clearly demonstrate the use of optically active nanomaterials *i.e.,* upconversion nanoparticles for food processing, food sensing and graphene oxide for plant protection. Upconversion nanoparticles assisted ergosterol conversion using sunlight in mushrooms is enough for daily intake nutritional requirement. Therefore, this can overcome vitamin D deficiency in the population. However, the UV emission intensity needs to be further enhanced to improve the conversion efficiency. Moreover, the study can be extended in different mushroom varieties to verify its efficiency.

Further upconversion nanoparticles were explored for lycopene sensing in Chapter 3 using a transparent strip having minimal scattering. The fabricated paper has a huge potential for on demand real time sensor-based systems, thereby surpassing the expensive extraction-based techniques. The sensor demands expensive lasers for its usage, therefore more efficient UCNPs can get excited using NIR emission from the sunlight, which can reduce the overall cost. Hence, in this scope the work can be extended further.

Pheromones have been explored as a green management strategy in Chapter 4. This technique is the most eco-friendly way of monitoring the pest populations as these composites are not applied directly in the plant or soil, thereby inhibiting the disturbance of the soil microbe interactions. However, the applied nanocomposite has been explored for just one pest species but in a field so many pests cause the crop damage and yield loss. Therefore, there is a huge scope to extend this work to control multilevel pest population in field applications. Also, the matrix reuse can be a potential platform, thereby improving the overall cost.

Final Remarks:

The upconversion nanoparticles can ensure the energy free light assisted processing. Upconversion nanoparticles also has a huge potential for detection of various biomolecules and important nutrient ions. This will ensure the early detection of the pest/diseases, deficiency and crop quality that will enable early correction. Nanotechnology has huge potential to revolutionize the agriculture sector by developing nano formulations with functional nanoparticles like light responsive materials. Thus, a light controlled delivery of the active ingredient will ensure the judicious and targeted application of the chemicals.

References

1. Shafiee-Jood, M. & Cai, X. Reducing Food Loss and Waste to Enhance Food Security and Environmental Sustainability. *Environmental Science and Technology* **50**, 8432–8443 (2016).

2. Ford, J. A. *et al.* Cardiovascular disease and vitamin D supplementation: Trial analysis, systematic review, and meta-analysis. *American Journal of Clinical Nutrition* **100**, 746–755 (2014).

3. Cantorna, M. T. Vitamin D and autoimmunity: is vitamin D status an environmental factor affecting autoimmune disease prevalence? *Proceedings of the Society for Experimental Biology and Medicine. Society for Experimental Biology and Medicine (New York, N.Y.)* **223**, 230–233 (2000).

4. Speer, G. *et al.* Vitamin D and estrogen receptor gene polymorphisms in type 2 diabetes mellitus and in android type obesity. *European journal of endocrinology* **144**, 385–389 (2001).

5. Hossein-Nezhad, A. & Holick, M. F. Vitamin D for health: A global perspective. *Mayo Clinic Proceedings* **88**, 720–755 (2013).

6. Holick, M. F. Sunlight and vitamin D for bone health and prevention of autoimmune diseases, cancers, and cardiovascular disease. *The American journal of clinical nutrition* vol. 80 at https://doi.org/10.1093/ajcn/80.6.1678s (2004).

7. E, G. *et al.* Intake of carotenoids and retinol in relation to risk of prostate cancer. *Journal of the National Cancer Institute* **87**, 1767–1776 (1995).

8. Majewski, S., Kutner, A. & Jablonska, S. Vitamin D Analogs in Cutaneous Malignancies. *Current Pharmaceutical Design* **6**, 829–838 (2007).

9. Norman, P., Moss, I., Sian, M., Gosling, M. & Powell, J. Maternal and postnatal vitamin D ingestion influences rat aortic structure, function and elastin content. *Cardiovascular Research* **55**, 369–374 (2002).

10. Holick, M. F. Medical progress: Vitamin D deficiency. *New England Journal of Medicine* vol. 357 266–281 at https://doi.org/10.1056/NEJMra070553 (2007).

11. Ginde, A. A., Liu, M. C. & Camargo, C. A. Demographic differences and trends of

vitamin D insufficiency in the US population, 1988-2004. *Archives of internal medicine* **169**, 626–632 (2009).

12. Tangpricha, V., Pearce, E. N., Chen, T. C. & Holick, M. F. Vitamin D insufficiency among free-living healthy young adults. *The American journal of medicine* **112**, 659–662 (2002).

13. Schwartz, G. G. & Hanchette, C. L. UV, latitude, and spatial trends in prostate cancer mortality: all sunlight is not the same (United States). *Cancer causes & control : CCC* **17**, 1091–1101 (2006).

14. Jakobsen, J. Bioavailability and bioactivity of vitamin D3 active compounds – Which potency should be used for 25-hydroxyvitamin D3? *International Congress Series* **1297**, 133–142 (2007).

15. Roberts, J. S., Teichert, A. & McHugh, T. H. Vitamin D2 formation from post-harvest UV-B treatment of mushrooms (Agaricus bisporus) and retention during storage. *Journal of agricultural and food chemistry* **56**, 4541–4544 (2008).

16. Jasinghe, V. J., Perera, C. O. & Sablani, S. S. Kinetics of the conversion of ergosterol in edible mushrooms. *Journal of Food Engineering* **79**, 864–869 (2007).

17. Aparna, P., Muthathal, S., Nongkynrih, B. & Gupta, S. K. Vitamin D deficiency in India. *Journal of Family Medicine and Primary Care* **7**, 324 (2018).

18. Bikle, D. D. Vitamin D metabolism, mechanism of action, and clinical applications. *Chemistry & biology* **21**, 319–329 (2014).

19. Holick, M. F. Cancer, sunlight and vitamin D. *Journal of Clinical & Translational Endocrinology* **1**, 179 (2014).

20. Qin, X. F., Zhao, L. S., Chen, W. R., Yin, D. W. & Wang, H. Effects of vitamin D on plasma lipid profiles in statin-treated patients with hypercholesterolemia: A randomized placebo-controlled trial. *Clinical nutrition (Edinburgh, Scotland)* **34**, 201–206 (2015).

21. Papandreou, D. & Hamid, Z. T. N. The Role of Vitamin D in Diabetes and Cardiovascular Disease: An Updated Review of the Literature. *Disease markers* **2015**, (2015).

22. Mattila, P., Lampi, A. M., Ronkainen, R., Toivo, J. & Piironen, V. Sterol and vitamin D2 contents in some wild and cultivated mushrooms. *Food Chemistry* **3**, 293–298 (2002).

23. Fernandes, Â., Antonio, A. L., Oliveira, M. B. P. P., Martins, A. & Ferreira, I. C. F. R. Effect of gamma and electron beam irradiation on the physico-chemical and nutritional properties of mushrooms: A review. *Food Chemistry* **135**, 641–650 (2012).

24. Koorapati, A., Foley, D., Pilling, R. & Prakash, A. Electron-beam Irradiation Preserves the Quality of White Button Mushroom (Agaricus bisporus) Slices. *Journal of Food Science* **69**, (2004).

25. Wittig, M., Krings, U. & Berger, R. G. Single-run analysis of vitamin D photoproducts in oyster mushroom (Pleurotus ostreatus) after UV-B treatment. *Journal of Food Composition and Analysis* **31**, 266–274 (2013).

26. Cardwell, G., Bornman, J. F., James, A. P. & Black, L. J. A Review of Mushrooms as a Potential Source of Dietary Vitamin D. *Nutrients* **10**, (2018).

27. Roberts, J. S., Teichert, A. & McHugh, T. H. Vitamin D $_2$ Formation from Post-Harvest UV-B Treatment of Mushrooms (*Agaricus bisporus*) and Retention During Storage. *Journal of Agricultural and Food Chemistry* **56**, 4541–4544 (2008).

28. Teichmann, A., Dutta, P. C., Staffas, A. & Jägerstad, M. Sterol and vitamin D2 concentrations in cultivated and wild grown mushrooms: Effects of UV irradiation. *LWT - Food Science and Technology* **40**, 815–822 (2007).

29. Barnkob, L. L., Argyraki, A., Petersen, P. M. & Jakobsen, J. Investigation of the effect of UV-LED exposure conditions on the production of vitamin D in pig skin. *Food chemistry* **212**, 386–391 (2016).

30. Huang, B.-H., Yung, K.-H. & Chang, S.-T. The Sterol Composition of Volvariella Volvacea and other Edible Mushrooms . *Mycologia* **77**, 959–963 (1985).

31. Mattila, P. *et al.* Contents of vitamins, mineral elements, and some phenolic compounds in cultivated mushrooms. *Journal of Agricultural and Food Chemistry* **49**, 2343–2348 (2001).

32. Holick, M. F. *et al.* Vitamin D2 is as effective as vitamin D3 in maintaining circulating concentrations of 25-hydroxyvitamin D. *Journal of Clinical Endocrinology and*

Metabolism **93**, 677–681 (2008).

33. Alves, M. *et al.* A review on antimicrobial activity of mushroom (Basidiomycetes) extracts and isolated compounds. *Planta medica* **78**, 1707–1718 (2012).

34. Carocho, M. & Ferreira, I. The Role of Phenolic Compounds in the Fight against Cancer – A Review. *Anti-Cancer Agents in Medicinal Chemistry* **13**, 1236–1258 (2013).

35. Taofiq, O., González-Paramás, A. M., Martins, A., Barreiro, M. F. & Ferreira, I. C. F. R. Mushrooms extracts and compounds in cosmetics, cosmeceuticals and nutricosmetics-A review.

36. Bischoff-Ferrari, H. A., Giovannucci, E., Willett, W. C., Dietrich, T. & Dawson-Hughes, B. Estimation of optimal serum concentrations of 25-hydroxyvitamin D for multiple health outcomes. *The American journal of clinical nutrition* **84**, 18–28 (2006).

37. Pludowski, P. *et al.* Vitamin D supplementation guidelines. *The Journal of steroid biochemistry and molecular biology* **175**, 125–135 (2018).

38. Ross, A. C., Taylor, C. L., Yaktine, A. L. & Del Valle, H. B. Dietary reference intakes for calcium and vitamin D. (2011).

39. Dietary Reference Intakes - Canada.ca.

40. Phillips, K. M. *et al.* Vitamin D and Sterol Composition of 10 Types of Mushrooms from Retail Suppliers in the United States. *Journal of Agricultural and Food Chemistry* **59**, 7841–7853 (2011).

41. O'Mahony, L., Stepien, M., Gibney, M. J., Nugent, A. P. & Brennan, L. The potential role of vitamin D enhanced foods in improving vitamin D status. *Nutrients* **3**, 1023–1041 (2011).

42. Jasinghe, V. J. & Perera, C. O. Ultraviolet irradiation: The generator of Vitamin D2 in edible mushrooms. *Food Chemistry* **95**, 638–643 (2006).

43. Jasinghe, V. J. & Perera, C. O. Distribution of ergosterol in different tissues of mushrooms and its effect on the conversion of ergosterol to vitamin D2 by UV irradiation. *Food Chemistry* **92**, 541–546 (2005).

44. Urbain, P. & Jakobsen, J. Dose-Response Effect of Sunlight on Vitamin D2 Production

in Agaricus bisporus Mushrooms. *Journal of agricultural and food chemistry* **63**, 8156–8161 (2015).

45. Wu, W. J. & Ahn, B. Y. Statistical optimization of ultraviolet irradiate conditions for Vitamin D2 synthesis in oyster mushrooms (Pleurotus ostreatus) using response surface methodology. *PLoS ONE* **9**, (2014).

46. Rzymski, P. *et al.* Multielemental analysis of fruit bodies of three cultivated commercial Agaricus species. *Journal of Food Composition and Analysis* **59**, 170–178 (2017).

47. Simon, R. R., Phillips, K. M., Horst, R. L. & Munro, I. C. Vitamin D Mushrooms: Comparison of the Composition of Button Mushrooms (Agaricus bisporus) Treated Postharvest with UVB Light or Sunlight. *Journal of Agricultural and Food Chemistry* **59**, 8724–8732 (2011).

48. Mattila, P. *et al.* Contents of vitamins, mineral elements, and some phenolic compounds in cultivated mushrooms. *Journal of agricultural and food chemistry* **49**, 2343–2348 (2001).

49. Banlangsawan, N. & Sanoamuang, N. Effect of UV-B Irradiation on Contents of Ergosterol, Vitamin D 2 , Vitamin B 1 and Vitamin B 2 in Thai Edible Mushrooms. *Chiang Mai J. Sci* **43**, 45–53 (2016).

50. Kristensen, H. L., Rosenqvist, E. & Jakobsen, J. Increase of vitamin D(2) by UV-B exposure during the growth phase of white button mushroom (Agaricus bisporus). *Food & nutrition research* **56**, (2012).

51. Koyyalamudi, S. R., Jeong, S. C., Song, C. H., Cho, K. Y. & Pang, G. Vitamin D2 formation and bioavailability from Agaricus bisporus button mushrooms treated with ultraviolet irradiation. *Journal of agricultural and food chemistry* **57**, 3351–3355 (2009).

52. Kalaras, M. D., Beelman, R. B. & Elias, R. J. Effects of postharvest pulsed uv light treatment of white button mushrooms (Agaricus bisporus) on vitamin D2 content and quality attributes. *Journal of Agricultural and Food Chemistry* **60**, 220–225 (2012).

53. Edward, T. L. *et al.* Change in Concentration of Vitamin D 2 in Oyster Mushrooms Exposed to 254nm and 365nm UV-light During Growth. *International Journal of*

Biochemistry and Biophysics **3**, 1–5 (2015).

54. Sławińska, A. *et al.* Study on Vitamin D2 stability in dried mushrooms during drying and storage. *Food Chemistry* **199**, 203–209 (2016).

55. Bennett, L. *et al.* Vitamin D2-enriched button mushroom (Agaricus bisporus) improves memory in both wild type and APPswe/PS1dE9 transgenic mice. *PloS one* **8**, (2013).

56. Chen, G., Qiu, H., Prasad, P. N. & Chen, X. Upconversion nanoparticles: Design, nanochemistry, and applications in Theranostics. *Chemical Reviews* **114**, 5161–5214 (2014).

57. Dong, H., Sun, L., Nanoscale, C. Y.- & 2013, undefined. Basic understanding of the lanthanide related upconversion emissions. *pubs.rsc.org* doi:10.1039/c3nr34069d.

58. Shen, J., Sun, L. D. & Yan, C. H. Luminescent rare earth nanomaterials for bioprobe applications. *Dalton Transactions* 5687–5697 (2008) doi:10.1039/B805306E.

59. Auzel, F. Upconversion and Anti-Stokes Processes with f and d Ions in Solids. *Chemical Reviews* **104**, 139–173 (2004).

60. Patra, A., Friend, C. S., Kapoor, R. & Prasad, P. N. Upconversion in Er3+:ZrO2 nanocrystals. *Journal of Physical Chemistry B* **106**, 1909–1912 (2002).

61. Dong, H., Sun, L. D. & Yan, C. H. Energy transfer in lanthanide upconversion studies for extended optical applications. *Chemical Society Reviews* **44**, 1608–1634 (2015).

62. Chen, G., Yang, C. & Prasad, P. N. Nanophotonics and nanochemistry: controlling the excitation dynamics for frequency up- and down-conversion in lanthanide-doped nanoparticles. *Accounts of chemical research* **46**, 1474–1486 (2013).

63. Wang, F., Banerjee, D., Liu, Y., Chen, X. & Liu, X. Upconversion nanoparticles in biological labeling, imaging, and therapy. *Analyst* **135**, 1839–1854 (2010).

64. Zhou, J., Liu, Z. & Li, F. Upconversion nanophosphors for small-animal imaging. *Chemical Society Reviews* **41**, 1323–1349 (2012).

65. Sun, L. D., Wang, Y. F. & Yan, C. H. Paradigms and challenges for bioapplication of rare earth upconversion luminescent nanoparticles: Small size and tunable emission/excitation spectra. *Accounts of Chemical Research* **47**, 1001–1009 (2014).

66. Nyk, M., Kumar, R., Ohulchanskyy, T. Y., Bergey, E. J. & Prasad, P. N. High contrast in vitro and in vivo photoluminescence bioimaging using near infrared to near infrared up-conversion in Tm 3+ and Yb 3+ doped fluoride nanophosphors. *Nano Letters* **8**, 3834–3838 (2008).

67. Chen, G. *et al.* (α-NaYbF 4:Tm 3+)/CaF 2 core/shell nanoparticles with efficient near-infrared to near-infrared upconversion for high-contrast deep tissue bioimaging. *ACS Nano* **6**, 8280–8287 (2012).

68. Liu, F., Ma, E., Chen, D., Yu, Y. & Wang, Y. Tunable red-green upconversion luminescence in novel transparent glass ceramics containing Er: NaYF4 nanocrystals. *Journal of Physical Chemistry B* **110**, 20843–20846 (2006).

69. Sivakumar, S., Van Veggel, F. C. J. M. & Raudsepp, M. Bright white light through up-conversion of a single NIR source from sol-gel-derived thin film made with Ln3+-doped LaF3 nanoparticles. *Journal of the American Chemical Society* **127**, 12464–12465 (2005).

70. Dong, B. *et al.* Optical thermometry through infrared excited green upconversion emissions in Er3+–Yb3+ codoped Al2O3. *Applied Physics Letters* **90**, 181117 (2007).

71. Kar, A. & Patra, A. Impacts of core–shell structures on properties of lanthanide-based nanocrystals: crystal phase, lattice strain, downconversion, upconversion and energy transfer. *Nanoscale* **4**, 3608–3619 (2012).

72. Chen, G. Y. *et al.* Enhancement of the upconversion radiation in Y2O3:Er3+ nanocrystals by codoping with Li+ ions. *Applied Physics Letters* **92**, 113114 (2008).

73. Chen, G. Y., Liang, H. J., Liu, H. C., Somesfalean, G. & Zhang, Z. G. Anomalous power dependence of upconversion emissions in Gd2O3:Er3+ nanocrystals under diode laser excitation of 970 nm. *Journal of Applied Physics* **105**, 114315 (2009).

74. Ivaturi, A. *et al.* Optimizing infrared to near infrared upconversion quantum yield of β-NaYF4:Er3+ in fluoropolymer matrix for photovoltaic devices. *Journal of Applied Physics* **114**, (2013).

75. Patra, A., Friend, C. S., Kapoor, R. & Prasad, P. N. Effect of crystal nature on upconversion luminescence in Er3+:ZrO2 nanocrystals. *Applied Physics Letters* **83**, 284–286 (2003).

76. Li, Y., Wei, X., compounds, M. Y.-J. of alloys and & 2011, undefined. Synthesis and upconversion luminescent properties of Er3+ doped and Er3+–Yb3+ codoped GdOCl powders. *Elsevier*.

77. Patra, A. *et al.* Sonochemical preparation and characterization of Eu2O3 and Tb2O3 doped in and coated on silica and alumina nanoparticles. *Journal of Physical Chemistry B* **103**, 3361–3365 (1999).

78. Suyver, J., Grimm, J., Krämer, K., luminescence, H. G.-J. of & 2005, undefined. Highly efficient near-infrared to visible up-conversion process in NaYF4: Er3+, Yb3+. *Elsevier*.

79. Yang, T. *et al.* Cubic sub-20 nm NaLuF4-based upconversion nanophosphors for high-contrast bioimaging in different animal species. *Elsevier*.

80. Sudheendra, L., Ortalan, V., Dey, S., Browning, N. D. & Kennedy, I. M. Plasmonic enhanced emissions from cubic NaYF4:Yb:Er/Tm nanophosphors. *Chemistry of Materials* **23**, 2987–2993 (2011).

81. Zhang, H. *et al.* Plasmonic Modulation of the Upconversion Fluorescence in NaYF4:Yb/Tm Hexaplate Nanocrystals Using Gold Nanoparticles or Nanoshells. *Wiley Online Library* **49**, 2865–2868 (2010).

82. Kumar Rai, V. *et al.* Surface-plasmon-enhanced frequency upconversion in doped tellurium-oxide glasses containing silver nanoparticles. *aip.scitation.org* **103**, 93526 (2008).

83. Kokuoz, B., DiMaio, J. R., Kucera, C. J., Evanoff, D. D. & Ballato, J. Color kinetic nanoparticles. *Journal of the American Chemical Society* **130**, 12222–12223 (2008).

84. Barnes, W. L., Dereux, A. & Ebbesen, T. W. Surface plasmon subwavelength optics. *Nature* **424**, 824–830 (2003).

85. Liu, T. M., Conde, J., Lipiński, T., Bednarkiewicz, A. & Huang, C. C. Smart NIR linear and nonlinear optical nanomaterials for cancer theranostics: Prospects in photomedicine. *Progress in Materials Science* vol. 88 89–135 at https://doi.org/10.1016/j.pmatsci.2017.03.004 (2017).

86. Lim, S. F. *et al.* In vivo and scanning electron microscopy imaging of upconverting nanophosphors in Caenorhabditis elegans. *Nano Letters* **6**, 169–174 (2006).

87. Qin, X. *et al.* Surface Plasmon-Photon Coupling in Lanthanide-Doped Nanoparticles. *Journal of Physical Chemistry Letters* **12**, 1520–1541 (2021).

88. Wang, L. *et al.* Fluorescence resonant energy transfer biosensor based on upconversion-luminescent nanoparticles. *Angewandte Chemie - International Edition* **44**, 6054–6057 (2005).

89. Tao, A., Sinsermsuksakul, P. & Yang, P. Tunable plasmonic lattices of silver nanocrystals. *Nature Nanotechnology* **2**, 435–440 (2007).

90. Saboktakin, M. *et al.* Metal-enhanced upconversion luminescence tunable through metal nanoparticle-nanophosphor separation. *ACS Nano* **6**, 8758–8766 (2012).

91. Haase, M. & Schäfer, H. Upconverting nanoparticles. *Angewandte Chemie - International Edition* **50**, 5808–5829 (2011).

92. Dwivedi, Y., Thakur, S. N. & Rai, S. B. Study of frequency upconversion in Yb3+/Eu3+ by cooperative energy transfer in oxyfluoroborate glass matrix. *Applied Physics B 2007 89:1* **89**, 45–51 (2007).

93. Wang, F. & Liu, X. Upconversion multicolor fine-tuning: Visible to near-infrared emission from lanthanide-doped NaYF4 nanoparticles. *Journal of the American Chemical Society* **130**, 5642–5643 (2008).

94. Chen, G., Ohulchanskyy, T. Y., Kumar, R., Ågren, H. & Prasad, P. N. Ultrasmall monodisperse NaYF4:Yb3+/Tm3+ nanocrystals with enhanced near-infrared to near-infrared upconversion photoluminescence. *ACS nano* **4**, 3163 (2010).

95. Yin, A., Zhang, Y., Sun, L. & Yan, C. Colloidal synthesis and blue based multicolor upconversion emissions of size and composition controlled monodisperse hexagonal NaYF4 : Yb,Tm nanocrystals. *Nanoscale* **2**, 953–959 (2010).

96. Liu, Y., Ouyang, Q., Li, H., Zhang, Z. & Chen, Q. Development of an Inner Filter Effects-Based Upconversion Nanoparticles-Curcumin Nanosystem for the Sensitive Sensing of Fluoride Ion. *ACS Applied Materials and Interfaces* **9**, 18314–18321 (2017).

97. Deng, R., Xie, X., Vendrell, M., Chang, Y. T. & Liu, X. Intracellular glutathione detection using MnO 2-nanosheet- modified upconversion nanoparticles. *Journal of the American Chemical Society* **133**, 20168–20171 (2011).

98. Wang, X. *et al.* High-Sensitivity Sensing of Divalent Copper Ions at the Single Upconversion Nanoparticle Level. *Analytical Chemistry* **93**, 11686–11691 (2021).

99. Alonso-Cristobal, P. *et al.* Highly Sensitive DNA Sensor Based on Upconversion Nanoparticles and Graphene Oxide. *ACS Applied Materials and Interfaces* **7**, 12422–12429 (2015).

100. Zhang, K., Zhu, G., Wei, Y., Zhang, L. & Shen, Y. Engineering of an Upconversion Luminescence Sensing Platform Based on the Competition Effect for Mercury-Ion Monitoring in Green Tea. *Journal of Agricultural and Food Chemistry* **69**, 8565–8570 (2021).

101. Pan, W., Zhao, J. & Chen, Q. Fabricating Upconversion Fluorescent Probes for Rapidly Sensing Foodborne Pathogens. *Journal of Agricultural and Food Chemistry* **63**, 8068–8074 (2015).

102. Liu, Q., Peng, J., Sun, L. & Li, F. High-efficiency upconversion luminescent sensing and bioimaging of Hg(II) by chromophoric ruthenium complex-assembled nanophosphors. *ACS Nano* **5**, 8040–8048 (2011).

103. Wang, N., Yu, X., Zhang, K., Mirkin, C. A. & Li, J. Upconversion Nanoprobes for the Ratiometric Luminescent Sensing of Nitric Oxide. *Journal of the American Chemical Society* **139**, 12354–12357 (2017).

104. Zhao, L. *et al.* Yolk-shell upconversion nanocomposites for LRET sensing of cysteine/homocysteine. *ACS Applied Materials and Interfaces* **6**, 11190–11197 (2014).

105. Ma, Y., Huang, S., Deng, M. & Wang, L. White upconversion luminescence nanocrystals for the simultaneous and selective detection of 2,4,6-trinitrotoluene and 2,4,6-trinitrophenol. *ACS Applied Materials and Interfaces* **6**, 7790–7796 (2014).

106. Naghdi, T. *et al.* Chitin Nanofiber Paper toward Optical (Bio)sensing Applications. *ACS Applied Materials and Interfaces* **12**, 15538–15552 (2020).

107. Breasted, J. H. & University of Chicago. Oriental Institute. The Edwin Smith surgical papyrus, published in facsimile and hieroglyphic transliteration with translation and commentary in two volumes. (1930).

108. Huang, X., Jain, P. K., El-Sayed, I. H. & El-Sayed, M. A. Plasmonic photothermal therapy (PPTT) using gold nanoparticles. *Lasers in Medical Science* **23**, 217–228

(2008).

109. Melamed, J., Edelstein, R., nano, E. D.-A. & 2015, undefined. Elucidating the fundamental mechanisms of cell death triggered by photothermal therapy. *ACS Publications* **9**, 6–11 (2012).

110. Dolmans, D. E. J. G. J., Fukumura, D. & Jain, R. K. Photodynamic therapy for cancer. *Nature Reviews Cancer 2003 3:5* **3**, 380–387 (2003).

111. Tee, S., Win, K., Goh, S., Teng, C. & Tang, K. Introduction to Photothermal Nanomaterials. (2022).

112. Zhu, L., Gao, M., Peh, C., Energy, G. H.-N. & 2019, undefined. Recent progress in solar-driven interfacial water evaporation: advanced designs and applications. *Elsevier* **57**, 507–518 (2019).

113. Menger, R. F., Funk, E., Henry, C. S. & Borch, T. Sensors for detecting per- and polyfluoroalkyl substances (PFAS): A critical review of development challenges, current sensors, and commercialization obstacles. *Chemical Engineering Journal* **417**, 129133 (2021).

114. Hu, M. *et al.* Gold nanostructures: engineering their plasmonic properties for biomedical applications. *pubs.rsc.org*.

115. Gärtner, W. W. Photothermal effect in semiconductors. *Physical Review* **122**, 419–424 (1961).

116. Chen, H. *et al.* Understanding the photothermal conversion efficiency of gold nanocrystals. *Small (Weinheim an der Bergstrasse, Germany)* **6**, 2272–2280 (2010).

117. Maysinger, D. Nanoparticles and cells: Good companions and doomed partnerships. *Organic and Biomolecular Chemistry* **5**, 2335–2342 (2007).

118. Benedek, T. G. The history of gold therapy for tuberculosis. *Journal of the history of medicine and allied sciences* **59**, 50–89 (2004).

119. Demann, E. T. K., Stein, P. S. & Haubenreich, J. E. Gold as an implant in medicine and dentistry. *Journal of long-term effects of medical implants* **15**, 687–698 (2005).

120. Liu, X. *et al.* A one-step homogeneous immunoassay for cancer biomarker detection using gold nanoparticle probes coupled with dynamic light scattering. *Journal of the*

American Chemical Society **130**, 2780–2782 (2008).

121. Abadeer, N. S. & Murphy, C. J. Recent Progress in Cancer Thermal Therapy Using Gold Nanoparticles. *Journal of Physical Chemistry C* **120**, 4691–4716 (2016).

122. Hirsch, L. R. *et al.* Nanoshell-mediated near-infrared thermal therapy of tumors under magnetic resonance guidance. *Proceedings of the National Academy of Sciences of the United States of America* **100**, 13549–13554 (2003).

123. Pissuwan, D., Valenzuela, S. M. & Cortie, M. B. Therapeutic possibilities of plasmonically heated gold nanoparticles. *Trends in biotechnology* **24**, 62–67 (2006).

124. Abdoon, A. S. *et al.* Efficacy and toxicity of plasmonic photothermal therapy (PPTT) using gold nanorods (GNRs) against mammary tumors in dogs and cats. *Nanomedicine : nanotechnology, biology, and medicine* **12**, 2291–2297 (2016).

125. Hillyer, J. F. & Albrecht, R. M. Gastrointestinal persorption and tissue distribution of differently sized colloidal gold nanoparticles. *Journal of pharmaceutical sciences* **90**, 1927–1936 (2001).

126. Kelly, K., Coronado, E., … L. Z.-T. J. of P. & 2003, undefined. The optical properties of metal nanoparticles: the influence of size, shape, and dielectric environment. *ACS Publications* **107**, 668–677 (2003).

127. Jain, P. K., Lee, K. S., El-Sayed, I. H. & El-Sayed, M. A. Calculated absorption and scattering properties of gold nanoparticles of different size, shape, and composition: Applications in biological imaging and biomedicine. *Journal of Physical Chemistry B* **110**, 7238–7248 (2006).

128. Murphy, C. J. *et al.* Anisotropic metal nanoparticles: Synthesis, assembly, and optical applications. *Journal of Physical Chemistry B* **109**, 13857–13870 (2005).

129. Link, S. & El-Sayed, M. A. Erratum: Simulation of the optical absorption spectra of gold nanorods as a function of their aspect ratio and the effect of the medium dielectric constant (Journal of Physical Chemistry B (1999) 103B). *Journal of Physical Chemistry B* **109**, 10531–10532 (2005).

130. Huang, X., El-Sayed, I. H., Qian, W. & El-Sayed, M. A. Cancer cell imaging and photothermal therapy in the near-infrared region by using gold nanorods. *Journal of the American Chemical Society* **128**, 2115–2120 (2006).

131. Yin, S. *et al.* Photothermal ablation cancer therapy using homogeneous Cs x WO 3 nanorods with broad near-infra-red absorption. *pubs.rsc.org* (2013) doi:10.1039/c3nr01025b.

132. Shibu, E. S., Hamada, M., Murase, N. & Biju, V. Nanomaterials formulations for photothermal and photodynamic therapy of cancer. *Journal of Photochemistry and Photobiology C: Photochemistry Reviews* **15**, 53–72 (2013).

133. Variation in age at death of dogs of different sexes and breeds - PubMed.

134. MacEwen, E. G. Spontaneous tumors in dogs and cats: models for the study of cancer biology and treatment. *Cancer metastasis reviews* **9**, 125–136 (1990).

135. Ali, M. R. K., Ibrahim, I. M., Ali, H. R., Selim, S. A. & El-Sayed, M. A. Treatment of natural mammary gland tumors in canines and felines using gold nanorods-assisted plasmonic photothermal therapy to induce tumor apoptosis. *International journal of nanomedicine* **11**, 4849–4863 (2016).

136. Safety and efficacy of targeted hyperthermia treatment utilizing gold nanorod therapy in spontaneous canine neoplasia | BMC Veterinary Research | Full Text.

137. Ali, M. R. K., Wu, Y. & El-Sayed, M. A. Gold-Nanoparticle-Assisted Plasmonic Photothermal Therapy Advances Toward Clinical Application. *Journal of Physical Chemistry C* **123**, 15375–15393 (2019).

138. Skrabalak, S. E., Au, L., Li, X. & Xia, Y. Facile synthesis of Ag nanocubes and Au nanocages. *Nature Protocols* **2**, 2182–2190 (2007).

139. Ye, E. *et al.* Plasmonic gold nanocrosses with multidirectional excitation and strong photothermal effect. *Journal of the American Chemical Society* **133**, 8506–8509 (2011).

140. Ali, M. R. K. *et al.* Efficacy, long-term toxicity, and mechanistic studies of gold nanorods photothermal therapy of cancer in xenograft mice. *Proceedings of the National Academy of Sciences of the United States of America* **114**, E3110–E3118 (2017).

141. Alkilany, A. M. & Murphy, C. J. Toxicity and cellular uptake of gold nanoparticles: What we have learned so far? *Journal of Nanoparticle Research* **12**, 2313–2333 (2010).

142. Huang, X., Tang, S., Yang, J., Tan, Y. & Zheng, N. Etching growth under surface confinement: An effective strategy to prepare mesocrystalline Pd nanocorolla. *Journal of the American Chemical Society* **133**, 15946–15949 (2011).

143. Dao, V.-D. *et al.* Carbon-based sunlight absorbers in solar-driven steam generation devices. *Wiley Online Library* **2**, 1700094 (2018).

144. Ni, G. *et al.* Volumetric solar heating of nanofluids for direct vapor generation. *Elsevier*.

145. Lou, J. *et al.* Bioinspired Multifunctional Paper-Based rGO Composites for Solar-Driven Clean Water Generation. *ACS Applied Materials and Interfaces* **8**, 14628–14636 (2016).

146. Hu, X. *et al.* Tailoring graphene oxide-based aerogels for efficient solar steam generation under one sun. *Wiley Online Library* **29**, 1604031 (2017).

147. Wang, L. *et al.* Photodynamic effect of functionalized single-walled carbon nanotubes: a potential sensitizer for photodynamic therapy. *Nanoscale* **6**, 4642–4651 (2014).

148. Wang, C. *et al.* Immunological responses triggered by photothermal therapy with carbon nanotubes in combination with anti-CTLA-4 therapy to inhibit cancer metastasis. *Advanced materials (Deerfield Beach, Fla.)* **26**, 8154–8162 (2014).

149. Wang, H. *et al.* Mn3O4-graphene hybrid as a high-capacity anode material for lithium ion batteries. *Journal of the American Chemical Society* **132**, 13978–13980 (2010).

150. Wang, H., Wang, X., Li, X. & Dai, H. Chemical self-assembly of graphene sheets. *Nano Research* **2**, 336–342 (2009).

151. Robinson, J. T., Perkins, F. K., Snow, E. S., Wei, Z. & Sheehan, P. E. Reduced graphene oxide molecular sensors. *Nano Letters* **8**, 3137–3140 (2008).

152. Liang, Y., Wang, H., Casalongue, H. S., Chen, Z. & Dai, H. TiO2 Nanocrystals grown on graphene as advanced photocatalytic hybrid materials. *Nano Research* **3**, 701–705 (2010).

153. Ito, Y. *et al.* Multifunctional Porous Graphene for High-Efficiency Steam Generation by Heat Localization. *Advanced materials (Deerfield Beach, Fla.)* **27**, 4302–4307 (2015).

154. Yang, J. *et al.* Functionalized Graphene Enables Highly Efficient Solar Thermal Steam Generation. *ACS Nano* **11**, 5510–5518 (2017).

155. Kim, H. D. *et al.* Enhanced Osteogenic Commitment of Human Mesenchymal Stem Cells on Polyethylene Glycol-Based Cryogel with Graphene Oxide Substrate. *ACS Biomaterials Science and Engineering* **3**, 2470–2479 (2017).

156. Rezaei, A., Aligholi, H., Zeraatpisheh, Z., Gholami, A. & Mirzaei, E. Collagen/chitosan-functionalized graphene oxide hydrogel provide a 3D matrix for neural stem/precursor cells survival, adhesion, infiltration and migration. *Journal of Bioactive and Compatible Polymers* **36**, 296–313 (2021).

157. Zhou, F. *et al.* Cancer photothermal therapy in the near-infrared region by using single-walled carbon nanotubes. *Journal of Biomedical Optics* **14**, 021009 (2009).

158. Robinson, J. T. *et al.* Ultrasmall reduced graphene oxide with high near-infrared absorbance for photothermal therapy. *Journal of the American Chemical Society* **133**, 6825–6831 (2011).

159. Sattary, M., Rafienia, M., Kazemi, M., Salehi, H. & Mahmoudzadeh, M. Promoting effect of nano hydroxyapatite and vitamin D3 on the osteogenic differentiation of human adipose-derived stem cells in polycaprolactone/gelatin scaffold for bone tissue engineering. *Materials Science and Engineering C* **97**, 141–155 (2019).

160. Wacker, M. & Holick, M. F. Sunlight and Vitamin D: A global perspective for health. *Dermato-Endocrinology* vol. 5 51–108 at https://doi.org/10.4161/derm.24494 (2013).

161. Webb, A. R. Who, what, where and when-influences on cutaneous vitamin D synthesis. *Progress in Biophysics and Molecular Biology* vol. 92 17–25 at https://doi.org/10.1016/j.pbiomolbio.2006.02.004 (2006).

162. WEBB, A. R., KLINE, L. & HOLICK, M. F. Influence of Season and Latitude on the Cutaneous Synthesis of Vitamin D 3 : Exposure to Winter Sunlight in Boston and Edmonton Will Not Promote Vitamin D 3 Synthesis in Human Skin. *The Journal of Clinical Endocrinology & Metabolism* **67**, 373–378 (1988).

163. Roth, D. E. *et al.* Global prevalence and disease burden of vitamin D deficiency: a roadmap for action in low- and middle-income countries. *Annals of the New York Academy of Sciences* **1430**, 44–79 (2018).

164. Keegan, R. J. H., Lu, Z., Bogusz, J. M., Williams, J. E. & Holick, M. F. Photobiology of vitamin D in mushrooms and its bioavailability in humans. *Dermato-Endocrinology* **5**, 165–176 (2013).

165. Krings, U. & Berger, R. G. Dynamics of sterols and fatty acids during UV-B treatment of oyster mushroom. *Food Chemistry* **149**, 10–14 (2014).

166. Guan, W. *et al.* Effects of UV-C treatment and cold storage on ergosterol and vitamin D2 contents in different parts of white and brown mushroom (Agaricus bisporus). *Food chemistry* **210**, 129–34 (2016).

167. Phillips, K. M., Horst, R. L., Koszewski, N. J. & Simon, R. R. Vitamin D4 in Mushrooms. *PLoS ONE* **7**, e40702 (2012).

168. Nagaraj, S., Easwaramoorthi, S., Rao, J. R. & Thanikaivelan, P. Probing visible light induced photochemical stabilization of collagen in green solvent medium. *International Journal of Biological Macromolecules* **131**, 779–786 (2019).

169. Zhao, S. *et al.* Multiplexed Readout of Enzymatic Reactions by Means of Laterally Resolved Illumination of Quantum Dot Electrodes. *ACS Applied Materials & Interfaces* **11**, 21830–21839 (2019).

170. Nandwana, V. *et al.* Engineering the Nanoscale Morphology of a Quantum Dot–Fullerene Assembly via Complementary Hydrogen Bonding Interactions. *Langmuir* **29**, 7534–7537 (2013).

171. Rao, C. N. R. & Dey, S. Solar thermochemical splitting of water to generate hydrogen. *Proceedings of the National Academy of Sciences of the United States of America* vol. 114 13385–13393 at https://doi.org/10.1073/pnas.1700104114 (2017).

172. Krishna, K. S., Sandeep, C. S. S., Philip, R. & Eswaramoorthy, M. Mixing does the magic: A rapid synthesis of high surface area noble metal nanosponges showing broadband nonlinear optical response. *ACS Nano* **4**, 2681–2688 (2010).

173. Han, R. L., Shi, J. H., Liu, Z. J., Hou, Y. F. & Wang, Y. Near-Infrared Light-Triggered Hydrophobic-to-Hydrophilic Switch Nanovalve for On-Demand Cancer Therapy. *ACS Biomaterials Science and Engineering* **4**, 3478–3486 (2018).

174. Liao, M. Y. *et al.* Surface state mediated NIR two-photon fluorescence of iron oxides for nonlinear optical microscopy. *Advanced Functional Materials* **23**, 2044–2051

(2013).

175. Lv, R. *et al.* When a Semiconductor Utilized as an NIR Laser-Responsive Photodynamic/Photothermal Theranostic Agent Integrates with Upconversion Nanoparticles. *ACS Biomaterials Science & Engineering* **5**, 3100–3110 (2019).

176. Kar, A., Kundu, S. & Patra, A. Lanthanide-Doped Nanocrystals: Strategies for Improving the Efficiency of Upconversion Emission and Their Physical Understanding. *ChemPhysChem* **16**, 505–521 (2015).

177. Yan, B., Boyer, J.-C., Habault, D., Branda, N. R. & Zhao, Y. Near Infrared Light Triggered Release of Biomacromolecules from Hydrogels Loaded with Upconversion Nanoparticles. *Journal of the American Chemical Society* **134**, 16558–16561 (2012).

178. Chien, Y.-H. *et al.* Near-Infrared Light Photocontrolled Targeting, Bioimaging, and Chemotherapy with Caged Upconversion Nanoparticles *in Vitro* and *in Vivo*. *ACS Nano* **7**, 8516–8528 (2013).

179. Meng, Z., Zhang, L., He, Z. & Lian, H. Mucosal Penetrating Bioconjugate Coated Upconverting Nanoparticles That Integrate Biological Tracking and Photodynamic Therapy for Gastrointestinal Cancer Treatment. *ACS Biomaterials Science & Engineering* **4**, 2203–2212 (2018).

180. Chen, D. *et al.* Multimodal Nanoprobe Based on Upconversion Nanoparticles for Monitoring Implanted Stem Cells in Bone Defect of Big Animal. *ACS Biomaterials Science & Engineering* **4**, 626–634 (2018).

181. Nagai, A. *et al.* Tumor Imaging Based on Photon Upconversion of Pt(II) Porphyrin Rhodamine Co-modified NIR Excitable Cellulose Enhanced by Aggregation. *ACS Biomaterials Science & Engineering* **1**, 1206–1210 (2015).

182. D'Souza, A. A., Kumari, D. & Banerjee, R. Nanocomposite biosensors for point-of-care—evaluation of food quality and safety. in *Nanobiosensors* 629–676 (Elsevier, 2017). doi:10.1016/b978-0-12-804301-1.00015-1.

183. Giust, D. *et al.* Graphene Oxide–Upconversion Nanoparticle Based Portable Sensors for Assessing Nutritional Deficiencies in Crops. *ACS Nano* **12**, 6273–6279 (2018).

184. Zhang, J. *et al.* Ultrasensitive and reusable upconversion-luminescence nanofibrous indicator paper for in-situ dual detection of single droplet. *Chemical Engineering*

Journal **382**, 122779 (2020).

185. Shan, J. *et al.* Biofunctionalization, cytotoxicity, and cell uptake of lanthanide doped hydrophobically ligated NaYF4 upconversion nanophosphors. *Journal of Applied Physics* **104**, 094308 (2008).

186. Yan, B., Boyer, J.-C., Branda, N. R. & Zhao, Y. Near-Infrared Light-Triggered Dissociation of Block Copolymer Micelles Using Upconverting Nanoparticles. *Journal of the American Chemical Society* **133**, 19714–19717 (2011).

187. Jayakumar, M. K. G., Idris, N. M. & Zhang, Y. Remote activation of biomolecules in deep tissues using near-infrared-to-UV upconversion nanotransducers. *Proceedings of the National Academy of Sciences of the United States of America* **109**, 8483–8488 (2012).

188. Wang, F. & Liu, X. Recent advances in the chemistry of lanthanide-doped upconversion nanocrystals. *Chemical Society Reviews* **38**, 976–989 (2009).

189. Pokhrel, M., Valdes, C. & Mao, Y. Ultraviolet upconversion enhancement in triply doped NaYF4:Tm3+, Yb3+ particles: The role of Nd3+ or Gd3+ Co-doping. *Optical Materials* **58**, 67–75 (2016).

190. Wilhelm, S. Perspectives for Upconverting Nanoparticles. *ACS Nano* vol. 11 10644–10653 at https://doi.org/10.1021/acsnano.7b07120 (2017).

191. Wang, F. & Liu, X. Multicolor tuning of lanthanide-doped nanoparticles by single wavelength excitation. *Accounts of Chemical Research* **47**, 1378–1385 (2014).

192. Kraft, M., Würth, C., Palo, E., Soukka, T. & Resch-Genger, U. Colour-optimized quantum yields of Yb, Tm Co-doped upconversion nanocrystals. *Methods and Applications in Fluorescence* **7**, (2019).

193. Liu, N., Qin, W., Qin, G., Jiang, T. & Zhao, D. Highly plasmon-enhanced upconversion emissions from Au@β-NaYF 4:Yb,Tm hybrid nanostructures. *Chemical Communications* **47**, 7671–7673 (2011).

194. Jin, L. M., Chen, X., Siu, C. K., Wang, F. & Yu, S. F. Enhancing Multiphoton Upconversion from $NaYF_4$:Yb/Tm@$NaYF_4$ Core–Shell Nanoparticles *via* the Use of Laser Cavity. *ACS Nano* **11**, 843–849 (2017).

195. Zhang, Y. Y., Yang, L. W., Xu, C. F., Zhong, J. X. & Sun, C. Q. Sensitized deep-ultraviolet up-conversion emissions of Gd3+ via Tm3+ and Yb3+ in hexagonal NaYF4 nanorods. *Applied Physics B: Lasers and Optics* **98**, 243–247 (2010).

196. Sharma, S., Singh, S., Ganguli, A. K. & Shanmugam, V. Anti-drift nano-stickers made of graphene oxide for targeted pesticide delivery and crop pest control. *Carbon* **115**, 781–790 (2017).

197. Guller, A. E. *et al.* Rational Surface Design of Upconversion Nanoparticles with Polyethylenimine Coating for Biomedical Applications: Better Safe than Brighter? *ACS Biomaterials Science and Engineering* **4**, 3143–3153 (2018).

198. Wilhelm, S. *et al.* Water dispersible upconverting nanoparticles: Effects of surface modification on their luminescence and colloidal stability. *Nanoscale* **7**, 1403–1410 (2015).

199. Mau, J.-L., Chen, P.-R. & Yang, J.-H. Ultraviolet Irradiation Increased Vitamin D_2 Content in Edible Mushrooms. *Journal of Agricultural and Food Chemistry* **46**, 5269–5272 (1998).

200. Holick, M. F. Vitamin D: a D-Lightful health perspective. *Nutrition Reviews* **66**, S182–S194 (2008).

201. Ciriminna, R., Fidalgo, A., Meneguzzo, F., Ilharco, L. M. & Pagliaro, M. Lycopene: Emerging Production Methods and Applications of a Valued Carotenoid. *ACS Sustainable Chemistry and Engineering* **4**, 643–650 (2016).

202. Lycopene Market by Form, Nature, and Application: Global Opportunity Analysis and Industry Forecast, 2021-2030.

203. Pereira Soares, N. da C. *et al.* Lycopene induce apoptosis in human prostate cells and alters the expression of Bax and Bcl-2 genes. *LWT - Food Science and Technology* **59**, 1290–1297 (2014).

204. E, F.-G. Skin protection against UV light by dietary antioxidants. *Food & function* **5**, 1994–2003 (2014).

205. E, G., EB, R., Y, L., MJ, S. & WC, W. A prospective study of tomato products, lycopene, and prostate cancer risk. *Journal of the National Cancer Institute* **94**, 391–398 (2002).

206. Wu, H. *et al.* Efficient production of lycopene from CO2 via microbial electrosynthesis. *Chemical Engineering Journal* **430**, 132943 (2022).

207. P, D. M., S, K. & H, S. Lycopene as the most efficient biological carotenoid singlet oxygen quencher. *Archives of biochemistry and biophysics* **274**, 532–538 (1989).

208. M, J. *et al.* Variations in lycopene blood levels and tomato consumption across European countries based on the European Prospective Investigation into Cancer and Nutrition (EPIC) study. *The Journal of nutrition* **135**, (2005).

209. EM, G. *et al.* A comparison of plasma and prostate lycopene in response to typical servings of tomato soup, sauce or juice in men before prostatectomy. *The British journal of nutrition* **114**, 596–607 (2015).

210. REGULATION (EC) No 1333/2008 OF THE EUROPEAN PARLIAMENT AND OF THE COUNCIL of 16 December 2008 on food additives (Text with EEA relevance).

211. Berna, A. Z., Lammertryn, J., Saevels, S., Di Natale, C. & Nicolaï, B. M. Electronic nose systems to study shelf life and cultivar effect on tomato aroma profile. *Sensors and Actuators B: Chemical* **97**, 324–333 (2004).

212. ES, M., G, M. & FP, Z. ABSORPTION SPECTRA OF ALPHA AND BETA CAROTENES AND LYCOPENE. *Plant physiology* **10**, 375–381 (1935).

213. Grabowska, M. *et al.* Let food be your medicine: nutraceutical properties of lycopene. *Food & Function* **10**, 3090–3102 (2019).

214. Balbinot, S., Srivastav, A. M., Vidic, J., Abdulhalim, I. & Manzano, M. Plasmonic biosensors for food control. *Trends in Food Science & Technology* **111**, 128–140 (2021).

215. Swarnkar, A., Shanker, G. S. & Nag, A. Organic-free colloidal semiconductor nanocrystals as luminescent sensors for metal ions and nitroaromatic explosives. *Chemical Communications* **50**, 4743–4746 (2014).

216. Zare, H., Ghalkhani, M., Akhavan, O., Taghavinia, N. & Marandi, M. Highly sensitive selective sensing of nickel ions using repeatable fluorescence quenching-emerging of the CdTe quantum dots. *Materials Research Bulletin* **95**, 532–538 (2017).

217. Ghosh, H. N., Pal, H., Palit, D. K., Mukherjee, T. & Mittal, J. P. Interaction of the

excited singlet state of disubstituted anthraquinones with aliphatic and aromatic amines: a fluorescence quenching study. *Journal of Photochemistry and Photobiology, A: Chemistry* **73**, 17–22 (1993).

218. Nuruddin, M. *et al.* Structure−Property Relationship of Cellulose Nanocrystal−Polyvinyl Alcohol Thin Films for High Barrier Coating Applications. *ACS Appl. Mater. Interfaces* **13**, 18 (2021).

219. Rachel Carson, Silent Spring.

220. Sharma, S. *et al.* Triple-smart eco-friendly chili anthracnose control agro-nanocarrier. *ACS Applied Materials and Interfaces* **13**, 9143–9155 (2021).

221. Gao, Y. *et al.* Fabrication of a hollow mesoporous silica hybrid to improve the targeting of a pesticide. *Chemical Engineering Journal* **364**, 361–369 (2019).

222. Gao, Y. *et al.* Metal-organic framework nanohybrid carrier for precise pesticide delivery and pest management. *Chemical Engineering Journal* 130143 (2021) doi:10.1016/j.cej.2021.130143.

223. Sharma, S. *et al.* Porous nanomaterials: Main vein of agricultural nanotechnology. *Progress in Materials Science* 100812 (2021) doi:10.1016/J.PMATSCI.2021.100812.

224. Bhattacharyya, A., Bhaumik, A., Rani, P. U., Mandal, S. & Epidi, T. T. Nano-particles-A recent approach to insect pest control. *African Journal of Biotechnology* **9**, 3489–3493 (2010).

225. Gopal, M., Kumar, R., Goswami, A. & others. Nano-pesticides-a recent approach for pest control. *The Journal of Plant Protection Sciences* **4**, 1–7 (2012).

226. Venugopal, V. & Subaharan, K. Olfactory response of red palm weevil, rhynchophorous ferrugineus (Olivier) (Coleoptera: Dryophthoridae), to host / food volatiles. *Journal of Plantation Crops* **47**, 41–47 (2019).

227. Stetter, J. & Lieb, F. Innovation in crop protection: Trends in research. *Angewandte Chemie - International Edition* vol. 39 1724–1744 at https://doi.org/10.1002/(sici)1521-3773(20000515)39:10<1724::aid-anie1724>3.0.co;2-5 (2000).

228. Hjeresen, D. L. & Gonzales, R. Peer Reviewed: Can Green Chemisty Promote

Sustainable Agriculture? *Environmental Science & Technology* **36**, 102A-107A (2002).

229. Dicke, M., Van Loon, J. J. A. & Soler, R. Chemical complexity of volatiles from plants induced by multiple attack. *Nature Chemical Biology* vol. 5 317–324 at https://doi.org/10.1038/nchembio.169 (2009).

230. Hara, N. *et al.* Diffusive separation of propylene/propane with ZIF-8 membranes. *Journal of Membrane Science* **450**, 215–223 (2014).

231. Burmann, P., Zornoza, B., Téllez, C. & Coronas, J. Mixed matrix membranes comprising MOFs and porous silicate fillers prepared via spin coating for gas separation. *Chemical Engineering Science* **107**, 66–75 (2014).

232. Bhagat, D., Samanta, S. K. & Bhattacharya, S. Efficient management of fruit pests by pheromone nanogels. *Scientific Reports* **3**, 1–8 (2013).

233. Silvestre-Albero, A. *et al.* High saturation capacity of activated carbons prepared from mesophase pitch in the removal of volatile organic compounds. *Carbon* **48**, 548–556 (2010).

234. Di Gregorio, F., Parrillo, F., Salzano, E., Cammarota, F. & Arena, U. Removal of naphthalene by activated carbons from hot gas. *Chemical Engineering Journal* **291**, 244–253 (2016).

235. Srinivas, G., Burress, J. & Yildirim, T. Graphene oxide derived carbons (GODCs): Synthesis and gas adsorption properties. *Energy and Environmental Science* **5**, 6453–6459 (2012).

236. Clark, N. *et al.* Temperature Programmed Desorption Study of Graphene Oxide. *APS* C1.175 (2009).

237. Wang, C., Yang, S., Ma, Q., Jia, X. & Ma, P. C. Preparation of carbon nanotubes/graphene hybrid aerogel and its application for the adsorption of organic compounds. *Carbon* **118**, 765–771 (2017).

238. Akhavan, O., Ghaderi, E. & Esfandiar, A. Wrapping bacteria by graphene nanosheets for isolation from environment, reactivation by sonication, and inactivation by near-infrared irradiation. *Journal of Physical Chemistry B* **115**, 6279–6288 (2011).

239. Hashemi, E. *et al.* Cyto and genotoxicities of graphene oxide and reduced graphene oxide sheets on spermatozoa. *RSC Advances* **4**, 27213–27223 (2014).

240. Kim, H. W. *et al.* Selective gas transport through few-layered graphene and graphene oxide membranes. *Science* **342**, 91–95 (2013).

241. Cui, Y., Kundalwal, S. I. & Kumar, S. Gas barrier performance of graphene/polymer nanocomposites. *Carbon* vol. 98 313–333 at https://doi.org/10.1016/j.carbon.2015.11.018 (2016).

242. Krungleviciute, V. *et al.* Probing the structure of carbon nanohorn aggregates by adsorbing gases of different sizes. *Journal of Physical Chemistry C* **112**, 5742–5746 (2008).

243. Ma, S. *et al.* Surfactant-modified graphene oxide membranes with tunable structure for gas separation. *Carbon* **152**, 144–150 (2019).

244. Wong, K. C., Goh, P. S., Taniguchi, T., Ismail, A. F. & Zahri, K. The role of geometrically different carbon-based fillers on the formation and gas separation performance of nanocomposite membrane. *Carbon* **149**, 33–44 (2019).

245. Fisher, E. R. Challenges in the characterization of plasma-processed three-dimensional polymeric scaffolds for biomedical applications. *ACS Applied Materials and Interfaces* **5**, 9312–9321 (2013).

246. Mwaura, J. K. *et al.* Photovoltaic cells based on sequentially adsorbed multilayers of conjugated poly(p-phenylene ethynylene)s and a water-soluble fullerene derivative. *Langmuir* **21**, 10119–10126 (2005).

247. Desneux, N. *et al.* Biological invasion of European tomato crops by Tuta absoluta: Ecology, geographic expansion and prospects for biological control. *Journal of Pest Science* **83**, 197–215 (2010).

248. Ballal, C. R., Gupta, A., Mohan, M., Lalitha, Y. & Verghese, A. The new invasive pest Tuta absoluta (Meyrick) (Lepidoptera: Gelechiidae) in India and its natural enemies along with evaluation of trichogrammatids for its biological control. *Current Science* **110**, 2155–2159 (2016).

249. Akhavan, O., Ghaderi, E., Shirazian, S. A. & Rahighi, R. Rolled graphene oxide foams as three-dimensional scaffolds for growth of neural fibers using electrical stimulation

of stem cells. *Carbon* **97**, 71–77 (2016).

250. Shanmugam, V., Selvakumar, S. & Yeh, C. S. Near-infrared light-responsive nanomaterials in cancer therapeutics. *Chemical Society Reviews* vol. 43 6254–6287 at https://doi.org/10.1039/c4cs00011k (2014).

251. Jannesari, M., Akhavan, O., Madaah Hosseini, H. R. & Bakhshi, B. Graphene/CuO2Nanoshuttles with Controllable Release of Oxygen Nanobubbles Promoting Interruption of Bacterial Respiration. *ACS Applied Materials and Interfaces* **12**, 35813–35825 (2020).

252. Agarwal, V. & Zetterlund, P. B. Strategies for reduction of graphene oxide – A comprehensive review. *Chemical Engineering Journal* vol. 405 127018 at https://doi.org/10.1016/j.cej.2020.127018 (2021).

253. Dickens, J. C. Olfaction in the boll weevil,Anthonomus grandis Boh. (Coleoptera: Curculionidae): Electroantennogram studies. *Journal of chemical ecology* **10**, 1759–85 (1984).

254. VISSER, J. H. ELECTROANTENNOGRAM RESPONSES OF THE COLORADO BEETLE, LEPTINOTARSA DECEMLINEATA, TO PLANT VOLATILES. *Entomologia Experimentalis et Applicata* **25**, 86–97 (1979).

255. Sharma, S. *et al.* Ecofriendly Fruit Switches: Graphene Oxide-Based Wrapper for Programmed Fruit Preservative Delivery to Extend Shelf Life. *ACS Applied Materials and Interfaces* **10**, 18478–18488 (2018).

256. Abdel-Karim, A. *et al.* High flux and fouling resistant flat sheet polyethersulfone membranes incorporated with graphene oxide for ultrafiltration applications. *Chemical Engineering Journal* **334**, 789–799 (2018).

257. Li, B. *et al.* Cross-plane conductance through a graphene/molecular monolayer/Au sandwich. *Nanoscale* **10**, 19791–19798 (2018).

258. Mohammadi, A. *et al.* Aqueous dispersion of polyurethane nanocomposites based on calix[4]arenes modified graphene oxide nanosheets: Preparation, characterization, and anti-corrosion properties. *Chemical Engineering Journal* **349**, 466–480 (2018).

259. Akhavan, O. Bacteriorhodopsin as a superior substitute for hydrazine in chemical reduction of single-layer graphene oxide sheets. *Carbon* **81**, 158–166 (2015).

260. Akhavan, O., Ghaderi, E., Abouei, E., Hatamie, S. & Ghasemi, E. Accelerated differentiation of neural stem cells into neurons on ginseng-reduced graphene oxide sheets. *Carbon* **66**, 395–406 (2014).

261. Szabó, T., Tombácz, E., Illés, E. & Dékány, I. Enhanced acidity and pH-dependent surface charge characterization of successively oxidized graphite oxides. *Carbon* **44**, 537–545 (2006).

262. Jannesari, M., Akhavan, O. & Madaah Hosseini, H. R. Graphene oxide in generation of nanobubbles using controllable microvortices of jet flows. *Carbon* **138**, 8–17 (2018).

263. Hatamie, S. *et al.* Curcumin-reduced graphene oxide sheets and their effects on human breast cancer cells. *Materials Science and Engineering C* **55**, 482–489 (2015).

264. Sharma, S. *et al.* Effect of galvanotaxic graphene oxide on chloroplast activity: Interaction quantified with Biolayer-Interferometry coupled confocal microscopy. *Carbon* **162**, 147–156 (2020).

265. McAllister, M. J. *et al.* Single sheet functionalized graphene by oxidation and thermal expansion of graphite. *Chemistry of Materials* **19**, 4396–4404 (2007).

266. Roy, S. *et al.* Enhanced molecular level dispersion and interface bonding at low loading of modified graphene oxide to fabricate super nylon 12 composites. *ACS Applied Materials and Interfaces* **7**, 3142–3151 (2015).

267. Celebi, K. *et al.* Ultimate permeation across atomically thin porous graphene. *Science* **344**, 289–292 (2014).

268. Mkhoyan, K. A. *et al.* Atomic and electronic structure of graphene-oxide. *Nano Letters* **9**, 1058–1063 (2009).

269. Zhang, W. *et al.* Preparation and characterization of novel functionalized prochloraz microcapsules using silica-alginate-elements as controlled release carrier materials. *ACS Applied Materials and Interfaces* **6**, 11783–11790 (2014).

270. Liang, Y. *et al.* Preparation of MSNs-Chitosan@Prochloraz Nanoparticles for Reducing Toxicity and Improving Release Properties of Prochloraz. *ACS Sustainable Chemistry and Engineering* **6**, 10211–10220 (2018).

271. Liang, Y. *et al.* Development of Novel Urease-Responsive Pendimethalin Microcapsules Using Silica-IPTS-PEI As Controlled Release Carrier Materials. *ACS Sustainable Chemistry and Engineering* **5**, 4802–4810 (2017).

272. Gadipelli, S., Lu, Y., Skipper, N. T., Yildirim, T. & Guo, Z. Design of hyperporous graphene networks and their application in solid-amine based carbon capture systems. *Journal of Materials Chemistry A* **5**, 17833–17840 (2017).

273. Hong, W. E. *et al.* Assembled growth of 3D Fe3O4@Au nanoparticles for efficient photothermal ablation and SERS detection of microorganisms. *Journal of Materials Chemistry B* **6**, 5689–5697 (2018).

274. Huang, C. C. & Liu, T. M. Controlled Au-Polymer Nanostructures for Multiphoton Imaging, Prodrug Delivery, and Chemo-Photothermal Therapy Platforms. *ACS Applied Materials and Interfaces* **7**, 25259–25269 (2015).

Appendix-Publications

Publications included in thesis

1. **Kaur, K**., Bindra, P., Mondal, S., Li, W.P., Sharma, S., Sahu, Bk., Shanmugam, V., Upconversion Nanodevice-Assisted Healthy Molecular Photocorrection, ACS Biomaterials Science & Engineering 2021, 7, 291-298. (IF=4.41)

2**. Kaur, K**., Sharma, S., Gupta, R., Shanmugam V. Nanomaze Lure: Pheromone Sandwich in Graphene Oxide Interlayers for Sustainable Targeted Pest Control ACS Appl. Mater. Interfaces 2021, 13, 48349−48357. (IF=9.22)

3. **Kaur, K**., Shanmugam V. Phone camera nano-biosensor using mighty sensitive reusable upconversion paper, ACS Applied Materials, and Interfaces. (IF=9.22)

Other Publications

4. Bindra, P., **Kaur, K**., Rawat, A., Sarkar, A. De, Singh, M., Shanmugam, V., Nano-hives for plant stimuli controlled targeted iron fertilizer application, Chemical Engineering Journal 2019, 375, 121995. (IF=13.27)

5. Chandel, M., **Kaur, K**., Sahu, BK., Sharma, S., Shanmugam, V., Promise of nano-carbon to the next generation sustainable agriculture Carbon 2022, 188, 461-481. (IF=9.59)

6. Sharma, S., Kumari, BK., Cao L, Bindra, P., **Kaur, K**, Shanmugam, V.., Porous nanomaterials: Main vein of agricultural nanotechnology...Progress in Materials Science, 2021, 100812. (IF=39.58)

7. Bindra, P., Nagargade, M., Sahu, BK., Shukla, SK., **Kaur, K**., ...Shanmugam, V., Porous Silica Biofiber: A Reusable, Sustainable Fertilizer Reservoir. ACS Omega 2022,7,6,4832-4839. (IF=3.512)

8. Sahu, B. K., Sharma, S., **Kaur, K**., Chandel, M., Sood, P., Singh, M., & Shanmugham, V. (2022). Farm waste-eggshell nanoparticles constitute gel for safe navigation of probiotic across the stomach. *Materials Today Communications*, 104876.

9. Palanisami, M., **Kaur, K**., Sahu, B. K., Kataria, S., Chandel, M., Sharma, A., ... & Shanmugam, V. (2022). Excellent enzymeless anti-oxidant sensor for fruit juice and wine using nano gold/metal selenide urchins decorated 2D-composite. *Microchemical Journal*, *183*, 108078.

10. Chandel, M., Kumar, P., Arora, A., Kataria, S., Dubey, S. C., **Kaur, K**., ... & Shanmugam, V. (2022). Nanocatalytic Interface to Decode the Phytovolatile Language for Latent Crop Diagnosis in Future Farms. *Analytical Chemistry*, *94*(31), 11081-11088.

11. Sahu, B. K., Nagargade, M., Chandel, M., **Kaur, K**., Swami, K., Kumar, P., ... & Shanmugam, V. (2022). Eco-Friendly Urea Nanosack: Jute Grafted Silica Nanoring Woven Fertilizer to Control Urea Release and Enhance Crop Productivity. *ACS Sustainable Chemistry & Engineering*, *10*(40), 13357-13366.